Spatio-temporal spectra and spectral transfers in fluid dynamics

by

Andrew J. Morten

A dissertation submitted in partial fulfillment
of the requirements for the degree of
Doctor of Philosophy
(Physics)
in The University of Michigan
2015

Doctoral Committee:

Associate Professor Brian K. Arbic, Co-Chair
Professor Charles R. Doering, Co-Chair
Professor John P. Boyd
Associate Professor Robert D. Deegan
Professor Glenn R. Flierl, Massachusetts Institute of Technology

To Yuwei & Liam

ACKNOWLEDGEMENTS

This dissertation was made possible thanks primarily to the support of Prof. Brian Arbic. I have been more than fortunate to have him as my adviser these past five years. He not only put up with me, but paid me for his trouble, while doing everything within his power to ensure my academic growth and success. My writing, presenting, and time management skills have been greatly improved thanks to his incredibly patient support.

I also thank my co-adviser Prof. Charles Doering for years of support and for the work involved in staying abreast of my research progress. Discussions about research with him were always enlightening. Many meetings between Brian and myself began with Brian saying “I talked to Charlie, and...,” foreshadowing the transfer of vital knowledge or that an important decision had been reached.

I want to especially thank Prof. Glenn Flierl for many in-depth discussions about my research. Despite his busy schedule, he made time for lengthy Skype conversations and several days-long visits to MIT. His scientific comments on my first paper were invaluable, and his interest in my work was a great encouragement to me. I am grateful that he provided the original numerical code for my simulations. I can now claim semi-expertise in using the oldest and latest versions of Fortran, an “experience” I would have otherwise missed out on.

On several occasions Prof. Robert Deegan asked probing questions that helped me better motivate my research in my writing. Prof. John Boyd was a pleasure to work with, and I am grateful for his advice during the initial phase of my thesis writing. I

thank all of my committee members for their comments on my dissertation and the discussion following my defense.

I am indebted to Prof. Divakar Viswanath for useful conversations about code optimization early on in my research. I appreciate all of the work done by Mike Messina, who supported our group's computational needs, including my use of the high-performance computer cluster provided by the University of Michigan Office of Research Cyberinfrastructure. I also thank Brock Palen for answering questions about cluster usage and apologize for my occasional extreme use of scratch space.

I am particularly indebted to the staff in the Physics department without whom I could not have completed my degree. Christina Zigulis and Chris Bolang were ever encouraging and helped me navigate any and all problems during my years at Michigan. I cannot overstate my gratitude for all of their help. The same is true for Prof. Cagliyan Kurdak, who provided much needed encouragement and advice in his role as graduate chair, later to be followed by Prof. Finn Larsen.

I thank my primary sources of funding support over the years. During my early years I was primarily supported by the U-M physics department through a combination of fellowships and graduate student instructorships. During my years in my adviser's lab I was primarily supported by National Science Foundation grants OCE-0960820 and OCE-1351837 and by my adviser's startup funds from the University of Michigan.

I am grateful for the camaraderie and support provided by past and present members of Prof. Arbic's research group, including Patrick Timko, David Trossman, Joseph Ansong, Alfedo Wetzel, Anna Savage, Conrad Luecke, Paige Martin, Steve Bassette, Amanda O'Rourke, and Houraa Daher. Life with you in the "lab" has been fruitful and most entertaining.

I appreciate the support during the past few years from my family. My father Ken and siblings Matt and Jenny were there for me when needed. My brother Matt deserves special thanks for visiting and watching over my infant son during the final stretch of my dissertation writing. My son Liam, even before he was born, provided me that extra motivation I needed to hurry up and finish and move on with my life. Thanks, buggy!

Finally, I have insufficient words to describe my gratitude for my wife Yuwei. Her support and encouragement have helped me get through the most difficult times in school and life. I will look back at my years in grad school as when we first met and forged a life together, during which time I apparently also conducted some research and wrote a thesis.

TABLE OF CONTENTS

CHAPTER

LIST OF FIGURES

<u>**Figure**</u>

LIST OF TABLES

Table

ABSTRACT

Spatio-temporal spectra and spectral transfers in fluid dynamics

by

Andrew J. Morten

Co-Chairs: Brian K. Arbic & Charles R. Doering

Motivated in part by interest in low-frequency variability in complicated flows such as the ocean or atmosphere but also by a general interest in the spatio-temporal structure of turbulent flows, we investigate two-dimensional and quasi-two-dimensional turbulence in the wavenumber-frequency domain.

First, given a general equation of motion we derive spatio-temporal spectral transfers and corresponding fluxes in terms of a general bilinear time-frequency representation. Such transfers generalize the spatial spectral transfers used in the well-known theories for the cascade of energy or enstrophy in two- and three-dimensional turbulence. Specifically for transfers based on the short-time Fourier transform, we also develop a theoretical model that quantifies the effects of either a mean flow or isotropic sweeping on the spatio-temporal spectral transfers.

Second, we use spatio-temporal spectral transfers as a diagnostic in simulations of forced-dissipated two-dimensional homogeneous isotropic turbulence, where the forcing is narrowband in both wavenumber *and frequency.* We use the simulations both to illustrate the physical meaning of the spectral transfers and to investigate the robustness of the diagnostic when applied to imperfect data. We find that temporal spectral fluxes remain quantitatively reliable for a range of dataset limitations, such as low temporal resolution, limited record duration, and the presence of a trend. The theory and numerical investigations outlined above provide a foundation for the interpretation of spatio-temporal transfers in more complex systems.

Third, we conduct a wavenumber-frequency analysis of a quasi-two-dimensional system: the single-layer shallow-water quasi-geostrophic equation on the beta plane, one of the simplest models for large scale oceanic and atmospheric dynamics. We report that the "nondispersive line" that sometimes appears in zonal wavenumber-frequency spectra is not just a signature of westward propagating vortices. The nondispersive line can also be a signature of westward propagating meandering jets, although the propagation speed of jets is slightly slower than that of westward propagating vortices. We also report the discovery of new spectral features, such as a "nonlinear dispersive curve" that also appears in simulations with meandering jets, and quasi-sinusoidal dispersive curves that appear in simulations with nearly zonal jets.

CHAPTER I

Introduction

1.1 General Introduction and Layout of Thesis

One typically begins a dissertation with some very broad statement about the importance of the field in which the research is situated. What is that field in this case? Because of the wide applicability of the technique presented in Chapter II, the broadest field of research to which at least part of this thesis applies would be "systems that change in time." A majority of scientists agree: this is a topic worth investigating (e.g. *Newton*, 1687).

However, most of this dissertation falls within the less general realm of fluid dynamics, with a considerable focus on fluid turbulence. Fluid dynamics itself encompasses a mind-boggling variety of systems: from the very large (galactic) to the very small (quantum hydrodynamics), with many examples in between, including geophysical flows (atmospheres, oceans), hydrology (rivers), geodynamical flows (mantle), magnetohydrodynamics (plasmas), aerodynamics, industrial applications (mixing), and hemodynamics (blood flow). The diagnostic developed and examined in this dissertation could in principle be applied to systems within any of these subdisciplines.

Situated within the field of fluid dynamics is the theory of turbulence. Although the diagnostic derived in this thesis may be applied to any flow, turbulence is such a ubiquitous and interesting phenomenon that it warrants particular attention. For example, both three-dimensional and two-dimensional turbulence are thought to play important roles in transfers of energy between scales in the ocean. Quantifying energy transfers in the ocean is important if we want to understand how the ocean affects Earth's climate.

The theory of turbulence has proved to be a difficult problem, allowing for few exact theoretical results. It has turned out that the most successful theoretical predictions have involved only purely spatial quantities. For example, there is Kolmogorov's four-fifths law (*Kolmogorov*, 1941b), an exact relation for the average of the cube of longitudinal velocity increments (which are by definition spatially separated). A related result is Kolmogorov's prediction of the form of the wavenumber spectrum of kinetic energy $\mathcal{E}(k) \sim \epsilon^{2/3} k^{-5/3}$ in the inertial range, where k is isotropic wavenumber and ϵ is the power put into the turbulent flow.

There has been less theoretical progress involving temporal quantities and spatio-temporal quantities in the theory of turbulence. For example, there are no exact results predicting two-time correlations or the form of energy spectra in frequency space or wavenumber-frequency space. Theoretical progress is made only by resorting to modeling approximations that apply in certain limits, such as within the dissipation range or when the small scale turbulence is "frozen in" a la Taylor's hypothesis (*Taylor*, 1938). Perhaps related to this lack of theory, until recently there have been relatively few studies of turbulence in wavenumber-frequency space. The main contribution of this dissertation is to look at a variety of flows in the wavenumber-frequency domain.

Why should we care about analyses in the wavenumber-frequency domain? One answer is that many flows have natural frequencies. For example, many geophysical systems experience periodic external forces, such as seasonal or diurnal cycles. In industrial applications such as mixing there are frequencies associated with the stirring, and in hemodynamics the heart pumps at regular intervals. Also, a wide variety of fluids are sufficiently complicated to allow one or more type of wave motion, with dispersion relations that can be straightforwardly diagnosed in wavenumber-frequency space. In addition to these linear effects, non-linear effects play a role as well. Consider that the non-linear advection term common to all fluids involves not just wavenumber triad interactions but frequency triad interactions as well. One major contribution of this dissertation is to provide an improved interpretation of nonlinear wavenumber-frequency triad interactions. We will show that nonlinearities can transfer substantial amounts of energy to high and low frequencies, alongside the well-known transfers to high and low wavenumbers. This nonlinear transfer in the frequency domain has been shown to be important in, for instance, ocean models of both low-frequency geostrophic flows and high-frequency internal gravity waves.

Each of the following three thesis chapters contributes to the study of fluid dynamics in *spatio-temporal* spectral space (e.g. in the frequency-wavenumber domain). A (perhaps too much) simplified outline of this thesis could be the following: Chapter II, “spatio-temporal spectral transfers generally;” Chapter III, “spatio-temporal spectral transfers in two-dimensional (2D) turbulence;” Chapter IV, “spatio-temporal spectra (mostly) and spectral transfers in quasi-2D turbulence;” and Chapter V, “future directions.” The next few paragraphs provide a summary of each chapter, and then the rest of this Introduction gives a more detailed background and motivation for each chapter in turn.

Chapter II formulates spatio-temporal spectral transfers in a way that is very general and can be applied to many different systems (not just fluid dynamics). After presenting the general formulation we narrow the focus to the advection term of pure two- or three-dimensional turbulence (i.e. Navier-Stokes flow). We conduct a theoretical investigation of the effects of two widely used modeling assumptions – Taylor’s 1938 hypothesis and the sweeping hypothesis (*Tennekes*, 1975)– on the form of the spatio-temporal spectral transfers.

Chapter III presents a numerical investigation of forced-dissipated two-dimensional turbulence, utilizing the theory and testing the predictions laid out in Chapter II. The motivation for these numerical investigations is to provide a foundation for the interpretation of spatio-temporal spectral transfers in more complicated systems. In other words, two-dimensional turbulence provides a simple "base case" for more geophysically interesting systems. We focus not only on the two-dimensional system but on the robustness of the diagnostic itself. While the theory in Chapter II assumes perfectly resolved continuous data, in Chapter III we study the effects of realistic dataset limitations (e.g., limited record duration and finite sampling intervals) that are important in practice.

Chapter IV focuses on the spatio-temporal spectra (with some discussion of transfers) in a more geophysically interesting system: the single-layer shallow water quasi-geostrophic equation on the planetary beta-plane (sometimes referred to as a 1 1/2 layer, or reduced gravity, or equivalent barotropic model). Chapter IV is motivated in part by the question of how nonlinearities can cause deviations from linear dispersion relations in wavenumber-frequency spectra, and in part by the ubiquity of westward propagating features, identified through their signatures in wavenumber-frequency spectra, in beta-plane systems such as Earth's ocean. We conduct a comprehensive wavenumber-frequency analysis of this system for a wide range of parameters, and we discover several previously unreported phenomena.

Another way to summarize this thesis is by the equation of motion studied in each chapter. Full descriptions of the equations below, including definitions of symbols, can be found in their respective chapters. In Chapter II we consider a very general equation of motion:

$$\frac{\partial}{\partial t} G(\boldsymbol{\chi}, t) = \sum_{n} A_n(\boldsymbol{\chi}, t), \tag{1.1}$$

and use as an example the forced-dissipated two-dimensional Navier-Stokes equations, shown here as the vorticity equation in spectral space:

$$\frac{\partial}{\partial t}|\boldsymbol{k}|^2\widetilde{\psi}(\boldsymbol{k},t) = \widetilde{J(\psi, \nabla^2\psi)}(\boldsymbol{k},t) - \widetilde{D}(\boldsymbol{k},t) - \widetilde{F}(\boldsymbol{k},t). \tag{1.2}$$

. In Chapter III we numerically investigate equation 1.2. In Chapter IV we add a deformation radius $L_d \equiv 1/k_d$ and a "beta term:"

$$\frac{\partial}{\partial t}(|\boldsymbol{k}|^2 + k_d^2)\widetilde{\psi}(\boldsymbol{k},t) = J(\widetilde{\psi, \nabla^2\psi + \beta y})(\boldsymbol{k},t) - \widetilde{D}(\boldsymbol{k},t) - \widetilde{F}(\boldsymbol{k},t), \tag{1.3}$$

and we conduct an extensive parameter sweep of that system.

1.2 Background for Chapter II

A fundamental insight central to the theory of turbulence is the *cascade* picture, in which energy (or, more generally, some other conserved quantity) is transferred locally between nearby spatial scales starting from some initial spatial scale and ending at some some faraway dissipation scale. Much of the utility of the cascade framework lies in the prediction of the form of the wavenumber spectrum $\mathcal{E}(k)$ of energy in the inertial range. Wavenumber spectra predictions were derived by *Kolmogorov* (1941b,a); *Obukhov* (1941a,b); *Onsager* (1945) for three-dimensional turbulence and by *Kraichnan* (1967); *Kraichnan* (1971); *Leith* (1968); *Batchelor* (1969) for two-dimensional turbulence, and verified experimentally (less so for the two-dimensional case) and numerically many times over.

An important component of this cascade picture is the spectral transfer, which we refer to as the *spatial* spectral transfer in order to avoid ambiguity later. The spatial spectral transfer quantifies the time rate of change of some spatial spectral quantity, typically wavenumber spectra of kinetic energy $\mathcal{E}(k)$ or enstrophy $\mathcal{Z}(k)$, due to various terms in the equation of motion. In the cascade picture it is the spatial spectral transfer due to the nonlinear advection term in the Navier–Stokes equations that plays an important role in our understanding of turbulence today.

While the spatial spectral transfer has been a fruitful tool in the study of turbulence – used in the derivation of some of the celebrated few exact theoretical results – we wonder if this usefulness as a *prognostic* has kept a more general spatio-temporal spectral transfer from being widely utilized as a *diagnostic*. In other words, while spatio-temporal transfers are less useful than spatial transfers in deriving exact theoretical results, they provide a useful measure of the spatio-temporal structure of a given flow, particularly if the flow is sufficiently complex to allow for transfers among and between different wavenumber-frequency modes of the system.

A few recent studies have calculated temporal and spatio-temporal spectral transfers and fluxes for a variety of systems. *Arbic et al.* (2012) diagnosed temporal spectral transfers using three data sets: output from several regions of a realistic general ocean circulation model, altimetric measurements of sea surface height in the same regions, and the output of a simple two-layer quasi-geostrophic model. A follow-up study (*Arbic et al.*, 2014) diagnosed spatio-temporal transfers using roughly the same three data sets. *Arbic et al.* (2012, 2014) were motivated by the possibility of linking the well-known nonlinear inverse cascade of energy towards larger spatial scales with low-frequency variability in the ocean. They found that in most of the examined regions nonlinear advection transferred energy to longer time scales, but in some regions energy was transferred to shorter time scales.

Concurrent and planned future research by our collaborators will apply the diagnostic to a variety of more complicated systems. Motivated by the ubiquitous westward propagation seen in the oceanic mesoscale eddy field, an additional study currently in preparation will focus on directional wavenumbers k and l in a two-layer geostrophic model with $\beta \neq 0$. A related study in preparation will look at simulation output from NEMO (Nucleus for European Modelling of the Ocean) (*Mandec*, 2008), and will utilize much longer time-series then those used in *Arbic et al.* (2012, 2014).

The diagnostic has also already been used as part of an investigation of internal gravity waves in the ocean (*Müller et al.*, 2015). That study looked at how well internal gravity waves are resolved in realistic global ocean models, run at two different horizontal resolutions (1/12° and 1/25°) and forced by atmospheric fields as well as tides. The higher resolution simulation includes additional wavenumber-frequency triad interactions not seen in the lower resolution simulation. Ongoing work will compute internal gravity wave spatio-temporal spectral transfers in global models run at even higher horizontal resolution (1/48°).

Several other ongoing studies will use spatio-temporal spectral transfers to investigate the interaction between the ocean and atmosphere. Motivated by the desire to quantitatively separate forced and intrinsic low-frequency variability, one study will diagnose contributions to temporal sea surface height variability separately made by nonlinear advection versus wind stress forcing. That research will be based on output from a state-of-the-art high resolution coupled climate model (*Donner et al.*, 2011). A companion paper using the same dataset will examine low-frequency contributions to sea surface temperature variability made separately by nonlinear advection and ocean-atmosphere heat exchange. Related studies will conduct similar investigations using an idealized quasi-geostrophic model of the coupled ocean-atmosphere system (Q-GCM; *Hogg et al.* (2003)).

There is a clear desire to use spatio-temporal and temporal spectral transfers to study a wide variety of systems, as outlined above. This thesis provides a rigorous foundation for the application of spatio-temporal spectral transfers in those and future investigations.

There are a small number of other studies of temporal spectral transfers in the literature. Four decades ago *Chiu* (1970) derived kinetic energy spectral equations in the frequency domain for large-scale atmospheric motions. *Sheng and Hayashi* (1990a,b) independently derived similar equations and applied them to global atmospheric simulations. *Elipot and Gille* (2009) derived similar spectral equations in order to study which frequency components dominate the wind energy input into the Ekman layer in the Southern Ocean.

The difference between the spectral transfers of earlier studies and those of Chapter II is that the earlier studies derive a spectral "balance" of energy in the frequency- or wavenumber-frequency domain, whereas here we obtain what can truly be described as spectral "transfers" of energy in the frequency or wavenumber-frequency domain. To directly quote *Chiu* (1970):

> "At this point, we note that when the spectrum in the wave number domain is interested, [...] the real part of the complex spectral equation (or the co-spectral equation) deals with the time rate of change of spectrum. On the other hand, when the spectrum in the frequency domain is interested, [...] the co-spectral equation does not deal with the time rate of change of spectrum, but with the balance among various co-spectra."

The mathematical framework presented in this dissertation describes how to incorporate the "time rate of change" that was absent in earlier derivations.

In the first half of Chapter II, we derive spatio-temporal spectral transfers and fluxes for a very general equation of motion. Although our main motivation is the study of fluid dynamics, the theory works for any equation of the form

$$\frac{\partial}{\partial t}G(\boldsymbol{\chi},t)=\sum_{n}A_n(\boldsymbol{\chi},t), \tag{1.4}$$

where the only requirements are the differentiability of $G(\boldsymbol{\chi},\cdot)$ and easily satisfied (weak) integrability requirements involving the functions $A_n(\boldsymbol{\chi},\cdot)$. The variable $\boldsymbol{\chi}$ represents all independent variables besides time t. In fluid dynamics applications,

$\boldsymbol{\chi}$ could be a spatial variable such as position $\boldsymbol{x}$ or wavevector $\boldsymbol{k}$, and $G(\boldsymbol{\chi}, t)$ could be the velocity, the vorticity, or a spatial Fourier or wavelet transform of the stream function (for example).

With 1.4 as the starting point, we derive general spatio-temporal transfers. The derivation must differ fundamentally from that of the more commonly used *spatial* spectral transfers because of the presence of the time-derivative in equation 1.4. Instead of a purely spectral (i.e. frequency) analysis, one needs to use a more general time-frequency analysis, such as the short time Fourier transform, a temporal wavelet transform, or some other bilinear time-frequency representation (*Cohen*, 1995). The derivations are shown for the general case of a bilinear time-frequency representation, which is a mathematically convenient way to simultaneously handle both Fourier transforms and wavelet transforms (and their generalizations). The use of a general bilinear representation also makes it clear that the many details of Fourier or wavelet analysis are not important to the derivation.

However, even the most general case of a bilinear time-frequency representation is not quite sufficient for our needs. In practical applications we may want to perform a detrending operation. The inclusion of a detrending operation may seem trivial, but is in fact subtle. Interestingly, if a detrending operation is incorporated into the mathematical framework in a particular way, then an exact spectral energy budget can still be derived.

After the general derivation of spatio-temporal spectral transfers, the remainder of Chapter II investigates the effect of a mean flow and isotropic sweeping on the spectral transfers and triad interactions, specifically in 2D and 3D turbulence. We also give an interpretation of the transfers in Chapter II. The remainder of this section provides the necessary background for these topics.

Taylor's hypothesis (*Taylor*, 1938) is often invoked in experimental investigations of turbulence in order to reconstruct spatial information from time-resolving measurements at a single point in space. Taylor's hypothesis states that the small-scale turbulent flow is advected without significant distortion by the large-scale mean flow. Another way to describe Taylor's hypothesis is that at sufficiently small scales the turbulence appears to be spatially "frozen" and simply translates uniformly at the mean velocity $\boldsymbol{U}$. Under this assumption, there is a mapping between spatial and temporal Fourier modes given by $\omega = \boldsymbol{k} \cdot \boldsymbol{U}$. It would require hundreds of pages *just to cite* every paper that invokes Taylor's hypothesis. The accuracy of Taylor's hypothesis has been investigated both theoretically (*Lumley*, 1965; *Wyngaard and Clifford*, 1977; *Hill*, 1996) and computationally (*Dosio et al.*, 2005; *Bahraminasab et al.*, 2008; *Del Alamo and Jimenez*, 2009; *Moin*, 2009, for some recent examples). It is natural to wonder what effect the assumption of Taylor's hypothesis has on spatio-temporal spectral transfers, a topic that to our knowledge has seen little investigation.

In the absence of a mean flow Taylor's hypothesis does not apply, but we may still try to find a relationship between the spatial and temporal properties of the spectral transfers by invoking a "sweeping hypothesis." According to the sweeping hypothesis (*Heisenberg*, 1948; *Tennekes*, 1975; *Chen and Kraichnan*, 1989; *Nelkin and Tabor*, 1990), the small-scale turbulent structures are still advected by larger-scale structures as is the case for Taylor's hypothesis, but the large-scale structures may have different (spatially locally averaged) mean velocities at different locations and times. According to very simple models of sweeping, the resulting relations between spatial statistics and temporal statistics are based on an averaging over the many different mean velocities. This dissertation presents a model of sweeping that adds some small improvements to the earlier models. The improvements make it possible to predict the effects of isotropic sweeping on spatio-temporal spectral transfers and triad interactions.

1.3 Background for Chapter III

To illustrate the use of spatio-temporal spectral transfers, we apply them to a simple fluid system: a modified version of the incompressible two-dimensional Navier–Stokes equation (for reviews of two-dimensional turbulence see *Boffetta and Ecke*, 2012; *Tabeling*, 2002; *Kellay and Goldburg*, 2002; *Kraichnan and Montgomery*, 1980). Motivated by the utility of diagnosing *spatial* spectral transfers in systems where energy and enstrophy are injected within a narrow range of wavenumber (recent examples include *Danilov and Gurarie*, 2001; *Chen et al.*, 2003; *Babiano and Dubos*, 2005; *Chen et al.*, 2006; *Boffetta*, 2007; *Xiao et al.*, 2009; *Dritschel et al.*, 2009; *Boffetta and Musacchio*, 2010), we choose to study the *spatio-temporal* spectral transfers in a system where energy and enstrophy are injected within a narrow range of wavenumber *and frequency*. To our knowledge, ours in the first study to use such a "modulated forcing" in simulations of pure two-dimensional turbulence.

Of note, forced-dissipated turbulence with a "modulated forcing" has been previously studied in three dimensions (*Lohse*, 2000; *Hooghoudt et al.*, 2001; *von der Heydt et al.*, 2003; *Cadot et al.*, 2003; *Kuczaj et al.*, 2006, 2008). In the three-dimensional case theoretical predictions were made based on the static structure functions of *Effinger and Grossmann* (1987). In three-dimensional modulated turbulence studies the focus has been on the prediction and existence of a resonant frequency. To our knowledge there have been no similar studies done for two-dimensional turbulence, which may be more complicated due to the dual cascade of energy and enstrophy.

The first purpose of Chapter III is to explain the physical meaning of spatio-temporal and temporal spectral transfers in these two-dimensional turbulence simulations. The motivation for studying this system is to connect our results with prior studies of spatio-temporal spectral transfers calculated using oceanic data and output of realistic ocean models (*Arbic et al.*, 2012, 2014). In those studies, for example, one region showed energy being transferred to smaller time scales, an unexpected result which may be partly explained by our results in Chapter III.

The second purpose of Chapter III is to use the output of our numerical simulations to test the robustness of temporal spectral transfers as a diagnostic. The satellite altimeter measurements of sea surface height used in calculating spectral transfers in *Arbic et al.* (2012, 2014) had both limited temporal resolution and duration, such that some relevant dynamical time scales were not resolved by the data. This is a problem typical of large scale oceanic datasets. Because our numerical simulations produce data that resolve all dynamical time scales, we are able to comprehensively study the effects of limited record duration, limited temporal resolution, and temporal detrending in a way not possible with realistic data. Our investigation in Chapter III shows that temporal spectral transfers are typically accurate over a range of frequencies even when the data set is severely limited. This robustness of the diagnostic is an important result, given our intent to apply spatio-temporal spectral transfers to realistic datasets in future work.

1.4 Background for Chapter IV

Satellite altimetric measurements of sea surface height, with relatively high resolution in both space and time, have made it possible to conduct systematic studies of the ocean in the wavenumber-frequency domain. In addition to calculations of sea surface height variance, we can also calculate kinetic energy spectra from sea surface heights when assuming geostrophic balance (*Vallis*, 2006). A recent study (*Wunsch*, 2009) calculated wavenumber-frequency spectra for several regions in the ocean and found that the spectra follows a “nondispersive line (NDL)” instead of any of the proposed linear dispersion relations. Follow-up studies have created empirical models for the spectra (*Wunsch*, 2010; *Wortham*, 2013; *Wortham and Wunsch*, 2014) which fit the data nicely, but do not provide a physical mechanism which explains the observations.

Early et al. (2011) investigated the NDL in simulations of the single-layer shallow-water quasi-geostrophic equation, seeded with Gaussian-profile vortices similar to eddies observed in the ocean. They found that if they removed the non-linear advection term then the spectra followed the linear dispersion relation. However, if they included non-linear advection then the spectra followed a NDL. In the nonlinear case the vortices maintained coherence much longer as they propagated westward. Studies of wavenumber-frequency spectra in simulations of a two-layer model also found there is a NDL in simulations that have high amplitude westward propagating vortices (*Berloff and Kamenkovich*, 2013a,b). While these studies show that the NDL may correspond to westward propagating coherent vortices in simple models, in theory the NDL could correspond to any (somewhat) coherent westward propagating structure.

These studies lead us to ask how common the NDL is in simulations of the single-layer shallow-water quasi-geostrophic equation. Rather than seeding the fluid with vortices as in *Early et al.* (2011), we study the case where coherent structures naturally emerge in forced-dissipated statistical equilibrium. We ask whether there are any flow regimes that produce a NDL besides westward propagating coherent vortices (the answer is yes). We also investigate wavenumber-frequency spectra for flow regimes that do not produce a NDL. As will be seen, a comprehensive investigation of wavenumber-frequency spectra for a wide variety of flow regimes results in some interesting observations, in particular a “nonlinear dispersive curve” (NDC) that appears to correspond to meandering jets. In addition to spectra we also calculate nonlinear spectral transfers, which provide a direct measurement of the involvement of nonlinearity in the formation of the NDL and NDC.

Thus, in Chapter IV we simulate the single-layer shallow-water quasi-geostrophic equation 1.3. The three key parameters are the deformation radius L_d (or equivalently, deformation wavenumber $k_d := 1/L_d$), the meridional gradient β of the Coriolis parameter, and the forcing wavenumber k_F. There have been relatively few studies of the general case ($k_d \neq 0$, $\beta \neq 0$), which is the subject of our investigation. There have been quite a few investigations of this equation with either $k_d = 0$ or $\beta = 0$. Much of the literature review that follows is about these two cases. The phenomenology of both of those cases are important for an understanding of the more general system.

Perhaps the most studied case is $k_d = 0$ (infinite deformation radius) and $\beta \neq 0$. The seminal paper by Rhines (*Rhines*, 1975) predicted that the inverse cascade of energy is nearly arrested at the Rhines wavenumber, the wavenumber at which the beta term reaches the same magnitude as the nonlinear advection term. In its simplest manifestation, the Rhines wavenumber is given by $k_{Rh} := \sqrt{\beta/2U_{rms}}$, where U_{rms} is the root mean square velocity. *Vallis and Maltrud* (1993) studied the effects of rough topography and also defined a transition wavenumber, $k_\beta := (\beta^3/\epsilon)^{1/5}$, which is intended to serve the same purpose as the Rhines wavenumber, but depends on ϵ, the energy injection rate by the forcing. Other studies of two-dimensional turbulence on a beta plane have investigated diffusion (*Smith et al.*, 2002) and the structural form of jets (*Danilov and Gurarie*, 2004; *Danilov and Gryanik*, 2004). A more recent study (*Sukoriansky et al.*, 2007) clarifies the interpretation of the Rhines wavenumber. *Sukoriansky et al.* (2007) argue that Rhines scale is not associated with the arrest of the inverse cascade, because the cascade continues (albeit anisotropically) to large scales until friction is reached. They also show that the Rhines scale should not be viewed as a crossover between turbulence and Rossby wave ranges, because Rossby waves and turbulence co-exist at smaller scales. The beta-plane simulations with $k_d = 0$ have been supplemented by simulations on a sphere (*Sukoriansky et al.*, 2007, 2008; *Galperin et al.*, 2010), demonstrating the existence of a new class of nonlinear waves called "zonons."

Another well-studied case is $\beta = 0$ and $k_d \neq 0$ (finite deformation radius). In this case the equation of motion is equivalent to the Charney-Hasegawa-Mima equation, which models drift-wave turbulence in magnetically confined plasmas (e.g. tokamaks). *Larichev and McWilliams* (1991) conducted simulations for a wide range of k_d and found coherent potential vorticity monopoles. *Kukharkin et al.* (1995) also studied coherent structures in this system, and *Iwayama et al.* (2002) studied the equation in the limit $k_d \to \infty$. Additional studies (*Tran and Bowman*, 2003; *Arbic and Flierl*, 2003; *Tran and Dritschel*, 2006) have looked at energy cascades, finding that a finite k_d acts as a shield to the kinetic energy cascade, allowing only potential energy to cascade to larger scales. *Tran and Dritschel* (2006) found that this cascade of potential energy is incredibly slow. Recently, *Scott and Dritschel* (2013) made predictions for the partitioning of total energy into kinetic and potential energy at equilibrium, assuming the large scale dissipation is by thermal damping, which is equivalent to our choice of damping.

Finally, there is the case $k_d \neq 0$ and $\beta \neq 0$, the focus of our study. This case has not been investigated by direct numerical simulation nearly as often as the $k_d = 0$ case or the $\beta = 0$ case. *Kukharkin and Orszag* (1996) found that jets formed when $k_d = 0$ are destabilized when k_d takes on a finite value. Instead, coherent vortices form with size somewhat larger than the deformation radius. *Okuno and Masuda* (2003) showed that a strong horizontal divergence (equivalently, large k_d) suppresses the Rhines effect (i.e. the anisotropization of the flow). The explanation for these observations is that for sufficiently large values of k_d the beta term cannot dominate the nonlinear term. *Smith* (2004) studied this system theoretical and numerically for a wide range of parameters. Their focus was on the parameter requirements for anisotropy and the production of jets, quite relevant to our study, although their form of large-scale dissipation is different from our own, and they did not study the system in the wavenumber frequency domain. A tangentially (pun intended) related study simulates the equation on a sphere (*Scott and Polvani*, 2007).

Our investigation is focused on wavenumber-frequency analyses of numerical simulations of equation 1.3 for a wide range of values of k_d and β. Two very recent studies have also looked at this system in wavenumber frequency space. *Zhang and Afanasyev* (2014) conducted an experimental study of barotropic and baroclinic turbulent flows generated in a rotating tank with a topographic beta effect. They observed the creation of jets and found evidence of linear Rossby waves in wavenumber-frequency spectra at low wavenumber. *Suhas and Sukhatme* (2015) conducted a numerical investigation similar to our own. Their main result is that Rossby waves account for most of the kinetic energy when there are jets. Our study considers a much broader parameter sweep and finds a greater variety of features in wavenumber-frequency spectra, and we investigate the role of nonlinear spectral transfers in the formation of the observed spectral features.

CHAPTER II

Spatio-temporal spectral transfers: theory

2.1 Overview of this Chapter

This chapter has a dual purpose: (1) to provide a derivation of general spatio-temporal spectral transfers, and (2) to derive the effects of a mean flow and isotropic sweeping on spectral transfers specifically when the transfers are based on the Fourier transform. In regard to layout of this dissertation, the present chapter is the theory for the results in Chapter III.

We begin (section 2.2) with the theory for spatio-temporal transfers and fluxes, allowing for a general equation of motion and a general spatial dependence. For example, one could apply a spatial filter or a spatial Fourier transform or wavelet analysis to the original equation of motion before proceeding to calculate the transfers. General spatio-temporal transfers are then defined in terms of temporal Fourier transforms, temporal wavelet analysis, and more general bilinear time-frequency distributions. Importantly, the effect of a temporal detrending operation is calculated and shown to be easily incorporated into the mathematical framework. While we provide general forms for the spatio-temporal transfers throughout, we simultaneously provide an illustrative example in the form of the spatially Fourier transformed two-dimensional vorticity equation.

We then proceed (section 2.3) to derive the effects of mean flows and isotropic sweeping on spatio-temporal and temporal spectral transfers in the case of the two-dimensional vorticity equation. These results rely specifically on the use of the spatial Fourier transform and the short-time Fourier transform, as opposed to the general spatial transform and general bilinear time-frequency representation considered in section 2.2. We show the effect of a Galilean transformation, which is roughly equivalent to the imposition of a mean flow, and we provide a model for the effect of isotropic sweeping on the spatio-temporal and temporal spectral transfers. We also show that spatio-temporal and temporal triad interactions are readily defined analogous to spatial triads (*Kraichnan*, 1967), that similar local conservation laws are satisfied, and that sweeping affects the locality of the generalized spatio-temporal triad interactions.

We also provide an interpretation of the spatio-temporal and temporal transfers following straightforwardly from the derivation. The issue of locality versus non-locality of the temporal triad interactions is quite important in the interpretation of spatio-temporal spectral transfers and fluxes. Temporal spectral fluxes typically should not be interpreted as arising from a spectrally local interaction, because of the effects of isotropic sweeping. It should be noted that spatial triad interactions are also not strictly spectrally local either. We review the main results of Chapter II in the Conclusion (section 2.4).

2.2 General theory for spatio-temporal spectral transfers

2.2.1 General and specific equations of motion

We derive spatio-temporal spectral transfers in a general way so they may be used in a wide variety of fluid dynamical applications. In order to be widely applicable, the equation of motion used as a starting point must be quite general. In order to motivate the general equation of motion, we begin this chapter with a few concrete examples.

We could start with the Navier–Stokes equations with generalized dissipation and forcing terms:

$$\partial_t \boldsymbol{u}(\boldsymbol{x},t) = -(\boldsymbol{u}\cdot\boldsymbol{\nabla})\boldsymbol{u} - \boldsymbol{\nabla}p + \boldsymbol{d}[\boldsymbol{u}] + \boldsymbol{f}(\boldsymbol{x},t), \qquad \boldsymbol{\nabla}\cdot\boldsymbol{u} = 0, \tag{2.1}$$

where $\boldsymbol{u}(\boldsymbol{x},t)$ is the Eulerian velocity field, p is pressure, $\boldsymbol{d}[\cdot]$ is a linear dissipation operator, and $\boldsymbol{f}(\boldsymbol{x},t)$ is an external force. We could start with the spatial Fourier transform of equation 2.1:

$$\partial_t \widetilde{\boldsymbol{u}}(\boldsymbol{k},t) = -\widetilde{(\boldsymbol{u}\cdot\boldsymbol{\nabla})\boldsymbol{u}} - \widetilde{\boldsymbol{\nabla}p} + \widetilde{\boldsymbol{d}[\boldsymbol{u}]} + \widetilde{\boldsymbol{f}}(\boldsymbol{k},t), \qquad \boldsymbol{k}\cdot\widetilde{\boldsymbol{u}} = 0, \tag{2.2}$$

where the operator "tilde" performs the two-dimensional spatial Fourier transform defined by $\widetilde{A}(\boldsymbol{k}) := \int\int d^2x\; e^{i\boldsymbol{k}\cdot\boldsymbol{x}}A(\boldsymbol{x})/L^2$, where L is the width of the square, periodic domain. If we were interested in looking at individual terms in the multi-scale gradient expansion of (*Eyink*, 2006a,b), we could begin with a low-pass filtered equation

$$\partial_t \overline{\boldsymbol{u}}(\boldsymbol{x},t,\ell) = -(\overline{\boldsymbol{u}}\cdot\boldsymbol{\nabla})\overline{\boldsymbol{u}} - \boldsymbol{\nabla}\cdot\boldsymbol{\tau} + \boldsymbol{d}[\overline{\boldsymbol{u}}] + \overline{\boldsymbol{f}}(\boldsymbol{x},t,\ell), \tag{2.3}$$

where

$$\overline{A}(\boldsymbol{x},t,\ell) := \int d^n\boldsymbol{r}\, G_\ell(\boldsymbol{r})A(\boldsymbol{x}+\boldsymbol{r}) \tag{2.4}$$

and $\boldsymbol{\tau} := \overline{\boldsymbol{u}\boldsymbol{u}} - \overline{\boldsymbol{u}}\,\overline{\boldsymbol{u}}$, following the notation of *Eyink* (2006a,b). Lastly, we could start with a spatial wavelet transform of 2.1 or some other primitive fluid equation.

All of the above equations can be written in the form

$$\partial_t G[\boldsymbol{u}](\boldsymbol{\chi},t,\{\alpha_i\}) = \sum_n A_n[\boldsymbol{u}](\boldsymbol{\chi},t,\{\alpha_i\}), \tag{2.5}$$

where $G[\cdot]$ and $A_n[\cdot]$ are (typically but not necessarily linear) functionals acting on the velocity $\boldsymbol{u}$; $\boldsymbol{\chi}$ is the new spatial coordinate, which for example could be the original coordinate $\boldsymbol{x}$ or a spectral coordinate $\boldsymbol{k}$; and $\{\alpha_i\}$ is some collection of additional coordinates, such as a length scale in a wavelet analysis.

The dependence of G and A_n on $\boldsymbol{u}$ will be used in section 2.3 when we determine the effects of mean flows and isotropic sweeping. However, in the current section the velocity $\boldsymbol{u}$ is irrelevant, and we can simply start with

$$\partial_t G(\boldsymbol{\chi}, t) = \sum_n A_n(\boldsymbol{\chi}, t), \tag{2.6}$$

where G and A_n are arbitrary functions (subject to suitable differentiability and integrability requirements).

Since we are primarily motivated by fluid dynamical applications, we show how to derive spectral transfers specifically for the two-dimensional vorticity equation in addition to the more general case of equation 2.6. The two-dimensional vorticity equation (with generalized forcing and dissipation) is

$$\frac{\partial}{\partial t}\nabla^2\psi(\boldsymbol{x}, t) + J(\psi, \nabla^2\psi) = D[\psi] + F, \tag{2.7}$$

which is obtained by taking the z-component of the curl of equation 2.1 (and assuming translation invariance in the z-direction). In equation 2.7, $\psi(\boldsymbol{x}, t) = \psi(x\widehat{\boldsymbol{x}} + y\widehat{\boldsymbol{y}}, t)$ is the stream function, which by definition is chosen so that $\partial_x\psi = \widehat{\boldsymbol{y}}\cdot\boldsymbol{u}$ and $\partial_y\psi = -\widehat{\boldsymbol{x}}\cdot\boldsymbol{u}$, implying that the scalar vorticity is $\nabla^2\psi = \widehat{\boldsymbol{z}}\cdot(\boldsymbol{\nabla}\times\boldsymbol{u})$; the Jacobian $J(\cdot,\cdot)$ is defined by $J(A, B) := \partial_x A\partial_y B - \partial_y A\partial_x B$; the dissipation term is $D[\psi] := \widehat{\boldsymbol{z}}\cdot(\boldsymbol{\nabla}\times\boldsymbol{d}[\boldsymbol{u}])$; and $F := \widehat{\boldsymbol{z}}\cdot(\boldsymbol{\nabla}\times\boldsymbol{f})$. Here, $\widehat{\boldsymbol{x}}$, $\widehat{\boldsymbol{y}}$, and $\widehat{\boldsymbol{z}}$ are the standard Cartesian coordinate unit vectors in the three-dimensional system.

The spatial Fourier transform of equation 2.7 is

$$\frac{\partial}{\partial t}k^2\widetilde{\psi}(\boldsymbol{k}, t) = \widetilde{J(\psi, \nabla^2\psi)}(\boldsymbol{k}, t) - \widetilde{D}(\boldsymbol{k}, t) - \widetilde{F}(\boldsymbol{k}, t), \tag{2.8}$$

where we have assumed periodic boundary conditions. In the rest of this section we derive spatio-temporal spectral transfers not only for the general equation of motion (equation 2.6) but also for equation 2.8.

2.2.2 Spectral transfers in $\boldsymbol{k}$-space

It is standard practice in turbulence theory to calculate spectral transfers or fluxes in the spatial domain, allowing one to diagnose the direction and magnitude of the transfer of energy (or enstrophy) between different spatial scales. Thus, it will be instructive to show first the derivation of spectral transfers in the spatial domain (briefly; for details see e.g. *Frisch*, 1995). While not strictly necessary, for simplicity we assume spatially periodic boundary conditions.

Multiplying equation 2.8 by $\widetilde{\psi}^*(\boldsymbol{k},t)$, where $*$ denotes complex conjugate, and taking the real part (Re[$\cdot$]) gives the equation for the *energy budget*:

$$\frac{\partial}{\partial t}E_{(1)}(\boldsymbol{k},t) := \frac{\partial}{\partial t}\tfrac{1}{2}k^2|\widetilde{\psi}|^2 = \mathrm{Re}[\widetilde{\psi}^*\widetilde{J(\psi,\nabla^2\psi)}] - \mathrm{Re}[\widetilde{\psi}^*\widetilde{D}] - \mathrm{Re}[\widetilde{\psi}^*\widetilde{F}], \tag{2.9}$$

where $E_{(1)}(\boldsymbol{k},t)$ is thought of as the energy *spectral density* in wave-vector mode $\boldsymbol{k}$ at time t. An additional multiplicative factor of k^2 in equation 2.9 results in the *enstrophy budget*:

$$\frac{\partial}{\partial t}Z_{(1)}(\boldsymbol{k},t) := k^2\frac{\partial}{\partial t}E_{(1)}(\boldsymbol{k},t) = k^2(\text{r.h.s of equation 2.9}), \tag{2.10}$$

where $Z_{(1)}(\boldsymbol{k},t)$ is thought of as the enstrophy spectral density in wave-vector mode $\boldsymbol{k}$ at time t. A subscript (1) on the energy and enstrophy is used to indicate that this is the first definition we give for the spatial spectral densities. We will provide a second definition later in section 2.2.5 that uses the spatio-temporal spectral densities defined in section 2.2.4.

For each wavevector $\boldsymbol{k}$ we refer to each term on the right-hand-side of the spectral budgets, (2.9) or (2.10), as the energy (or enstrophy) *spectral transfer* into wavevector mode $\boldsymbol{k}$ due to that term. In general, for any term $A_n(\boldsymbol{\chi}, t)$ in the general equation of motion (2.6) we denote the corresponding spatial spectral transfer by $\mathcal{A}_n(\boldsymbol{\chi}, t)$ or simply $\mathcal{A}(\boldsymbol{\chi}, t)$. As is standard for homogeneous isotropic turbulence, when $\boldsymbol{\chi} \equiv \boldsymbol{k}$, one typically integrates over all spectral angles to obtain energy (or enstrophy) spectral transfers dependent only on the isotropic wavenumber k. We refer to the corresponding reduced spectral densities as $E_{(1)}(k,t)$ and $Z_{(1)}(k,t)$, and we refer to their temporal averages as $\mathcal{E}_{(1)}(k)$ and $\mathcal{Z}_{(1)}(k)$.

One may proceed to calculate *spectral fluxes* defined as integrals of the spectral transfers:

$$\Pi^{>}_{\mathcal{A}}(k,t) := \int_{k}^{\infty} dk'\ \mathcal{A}(k',t), \quad \text{and} \quad \Pi^{>}_{\mathcal{A}}(k) := \int_{k}^{\infty} dk'\ \mathcal{A}(k') \tag{2.11}$$

where $\mathcal{A}(k,t)$ is a spatial spectral transfer and $\mathcal{A}(k)$ is its time-average. Note that we allow $\mathcal{A}$ to be any spatial spectral transfer term, not just the nonlinear advection term. Because the linear terms act locally in k-space, the standard notion of a "flux through k" makes little sense for the linear terms. However, a "transfer at k" does make sense for the linear terms, and the corresponding flux $\Pi^{>}_{\mathcal{A}}(k,t)$ is simply an integral of the transfer.

2.2.3 A note on notation

Throughout this chapter we employ a useful convention: a single function name may be used more than once to refer to several different functions, but each function is uniquely defined by the number and dimensions of the inputs. For example, $E(\boldsymbol{k},t)$, $E(k,t)$, $E(\boldsymbol{k},\omega,\tau)$, and $E(k,\omega,\tau)$ refer to four different functions (the last two are defined later). Also, the spatial spectral transfer $\mathcal{A}(k,t)$ and the temporal spectral transfer $\mathcal{A}(\omega,t)$ (defined later) are distinguished by the use of different input variables, k versus ω; the same is true for the spatial spectral flux $\Pi^{>}_{\mathcal{A}}(k,t)$ and the temporal spectral flux $\Pi^{>}_{\mathcal{A}}(\omega,t)$ (also defined later). Sometimes, additional parameters will be included after a semicolon without changing the meaning of a function. For example $E(\boldsymbol{k}, \omega, \tau; T)$ is the same function as $E(\boldsymbol{k}, \omega, \tau)$, but with the dependence on the parameter T simply made explicit. These conventions greatly reduce the number of symbols that the reader would otherwise need to remember.

2.2.4 Spectral transfers in $(\boldsymbol{k}, \omega)$-space

One might expect to be able to derive temporal and spatio-temporal spectral transfers analogous to the derivation of spatial spectral transfers derived in section 2.2.2. However, temporal spectral transfers are fundamentally different because of the temporal derivative in equation 2.6. While the temporal derivative commutes with spatial detrending and spatial Fourier transforms (or any other spatial operator), the temporal derivative does not commute with temporal detrending and temporal Fourier transforms.

A naive application of a temporal Fourier transform to equation 2.8 in an attempt to derive temporal spectral transfers results in the replacement of the time-derivative by $-i\omega$, which then drops out of the equation upon taking the real part. The absence of a temporal derivative in the result prohibits the interpretation of the remaining terms as rates of change (i.e. transfers) of energy in spectral space. Instead, one simply obtains a balance of terms. Less naive methods (*Chiu*, 1970; *Sheng and Hayashi*, 1990a,b; *Elipot and Gille*, 2009), which employ autocorrelation functions, also result in a balance among terms in wavenumber-frequency space rather than provide an interpretation of each term as a spectral transfer. In order to truly derive temporal spectral transfers, we need both a time derivative and a frequency variable in the final spectral budget. Thus, we turn to time-frequency representations.

In this section we define general spatio-temporal spectral transfers in terms of general bilinear time-frequency analysis methods. The time-frequency methods take as an input a signal $f(t)$ and output a time-frequency representation, $\mathrm{TFR}_f(\omega, \tau)$, that is quadratic in f. The representation $\mathrm{TFR}_f(\omega,\tau)$ depends on two variables: a frequency ω, which is typically related to the time-scale of the spectral content; and a "central time" τ, which is typically the center of some temporal window inside which the spectral content is calculated. See (see, e.g. *Hlawatsch and Auger*, 2008) for a review of time-frequency analysis methods.

The two most commonly used bilinear time-frequency representations are the spectrogram and the scalogram, which are the modulus squared of the short time Fourier transform (STFT) and the wavelet transform (WT) respectively. Given a function $f(t)$ we define the short time Fourier transform:

$$\mathrm{STFT}_f(\omega,\tau;T) := \int\limits_{\tau-T/2}^{\tau+T/2} \sigma_T(t-\tau) f(t) e^{-i\omega(t-\tau)} dt, \tag{2.12}$$

where $\sigma_T(s)$ is a window function of width T centered at $s=0$. For later convenience we have inserted a multiplicative factor of $e^{i\omega\tau}$ into the usual definition of the STFT. We also define the wavelet transform:

$$\mathrm{WT}_f(\omega,\tau) := \int\limits_{-\infty}^{\infty} f(t)|\omega|^{1/2} W((t-\tau)\omega) dt, \tag{2.13}$$

where $W(\cdot)$ is the "mother wavelet," which can be chosen according to desired properties.

Equations 2.12 and 2.13 are special cases of more general time-frequency representations: Cohen's class (*Cohen*, 1995) of time-frequency representations (which includes the STFT) and the affine class of time-frequency representations (which includes the WT). Sometimes it is possible to use these more general forms to obtain better temporal localization in the time-frequency representation (while also attempting to minimize cross-terms). In general, one defines

$$C_f(\omega,\tau) := \int\limits_{-\infty}^{\infty}\int\limits_{-\infty}^{\infty} d\tau' dt\ \phi_{\text{t-d}}(\tau-\tau',t)e^{-i\omega t} f\left(\tau'+\frac{t}{2}\right) f^*\left(\tau'-\frac{t}{2}\right) \tag{2.14}$$

for Cohen's class, and

$$\Omega_f(\omega,\tau) := \frac{\omega}{\omega_0}\int\limits_{-\infty}^{\infty}\int\limits_{-\infty}^{\infty} d\tau' dt\ \phi_{\text{t-d}}\left(\frac{\omega}{\omega_0}(\tau'-\tau),\frac{\omega}{\omega_0}t\right) f\left(\tau'+\frac{t}{2}\right) f^*\left(\tau'-\frac{t}{2}\right) \tag{2.15}$$

for the affine class, where ω_0 is some reference frequency. Both of these time-frequency representations have the form

$$\text{TFR}_f(\omega,\tau) := \int\limits_{-\infty}^{\infty}\int\limits_{-\infty}^{\infty} d\tau' dt\ K(\tau'-\tau,t,\omega) f\left(\tau'+\frac{t}{2}\right) f^*\left(\tau'-\frac{t}{2}\right), \tag{2.16}$$

where the kernel K is an arbitrary function. One reason we use equation 2.16 is that it handles both the short-time Fourier transform and continuous wavelet transform without reference to the specific details of each transform. The specific choice of K, and hence whether one is using a STFT or a WT or some other transform, is unimportant in the derivation of spatio-temporal spectral transfers.

In the above formulation of general bilinear time-frequency representations, the function $\phi_{\text{t-d}}(\cdot,\cdot)$ is the *time-delay* kernel (see, e.g. *Hlawatsch and Auger*, 2008), which can be chosen according to desired properties. For the STFT, $\phi_{\text{t-d}}(s,t) := \sigma^*(-s+t/2)\sigma(-s-t/2)$, where $\sigma(\cdot)$ is the window function, and the resulting spectral density $C_f(\omega,\tau)$ is the spectrogram $|STFT_f(\omega,\tau)|^2$. For the WT, $\phi_{\text{t-d}}(s,t)$ is given by the Fourier transform (in the second argument) of the Wigner-Ville distribution $W_\psi(s,\omega)$ for the mother wavelet $\psi(t)$, and the resulting spectral density $\Omega_f(\omega,\tau)$ is the scalogram $|WT_f(\omega,\tau)|^2$. There are several other equivalent formulations of the spectral densities $C_f(\omega,\tau)$ and $\Omega_f(\omega,\tau)$ which are obtained by convolving the Fourier transform of the kernel with the Fourier transform of the rest of the integrand. We choose to present the time-delay formulation because in that case the temporal spectral transfers take the simplest form and the effect of a detrending operation is most easily derived.

It is common practice in time-series analysis to first apply a detrending operation to the raw data prior to any other data manipulation. However, if not done correctly, detrending might substantially affect all frequencies in the analysis, because any nonlinear term (such as the advection term) may produce nonlinear interactions between frequency modes, warranting caution. Therefore, for our method to be useful in practice, we should carefully incorporate the effects of detrending.

In order to incorporate a detrending operation into the standard time-frequency analysis methods, one must first recognize that a detrended function depends not only on time t but also on the central time τ and duration T of the window over which the trend is calculated. That is, given some function $f(t)$ the result of a detrending operation is

$$f_{detrend}(t,\tau;T) := f(t) - f_{trend}(t,\tau;T), \tag{2.17}$$

where $f_{trend}(t,\tau;T)$ is the trend (such as a best fit line) calculated based on data within the range $[\tau - T/2, \tau + T/2]$. Moreover, it is typically natural to equate τ in equation 2.17 with τ in equations 2.14 and 2.15. Thus, we may extend the definition of a time-frequency transform to take as input a function of the form $f(t,\tau;T)$ rather than just $f(t)$, and we do so by simply replacing all evaluations of the function $f(\cdot)$ in equations 2.12, 2.13, 2.14 and 2.15 by evaluations of the more general function $f(\cdot,\tau;T)$. For example, the generalized STFT is

$$\mathrm{STFT}_{f_{detrend}}(\omega,\tau;T) := \int\limits_{\tau-T/2}^{\tau+T/2} \sigma_T(t-\tau) f_{detrend}(t,\tau;T) e^{-i\omega(t-\tau)} dt. \tag{2.18}$$

For the WT, which does not use a window of width T, the scale $(2\pi/\omega)$ of the wavelet is most naturally taken to correspond to the width of the detrending window. In that case, one must allow $T = T(\omega)$ to be a function of ω. For general time-frequency representations, the width T of the detrending window could depend on both τ and ω, but we must require $\partial_\tau T(\tau, \omega) = 0$ for the following derivations.

Any detrending operation that satisfies certain linearity and commutation-like requirements is allowed. Specifically, we require linearity:

$$(\alpha f + \beta g)_{detrend}(t, \tau; T) = \alpha f_{detrend}(t, \tau; T) + \beta g_{detrend}(t, \tau; T), \tag{2.19}$$

for any two constants α and β and input functions f and g. We also require the following commutation rule between time derivatives and the detrending operation:

$$\left(\frac{\partial}{\partial t} f(t)\right)_{detrend}(t, \tau; T) = \frac{\partial}{\partial t} f_{detrend}(t, \tau; T) + \frac{\partial}{\partial \tau} f_{detrend}(t, \tau; T). \tag{2.20}$$

We have verified that any linear least squares fit (and some generalizations thereof) satisfies these requirements. Here linear means "linear in the fit parameters," so that the trend would take the form $f_{trend}(t, \tau; T) := \sum a_m(\tau; T)\phi_m(t - \tau; T)$, where $a_m(\tau; T)$ are the fit parameters and $\{\phi_m(t - \tau; T)\}$ is the collection of fit functions. It is necessary that the fit functions ϕ_m depend on t and τ through the combination $t - \tau$, implying that the fit functions maintain their form relative to the center of the moving window. In addition to linear least squares, any linear filter acting upon windowed data would work as well. That is, f_{trend} could take the form of a convolution of the windowed signal with an impulse response function. Mathematically, this would be expressed as $f_{trend}(t, \tau; T) := h(t) *_t (\sigma_T(t - \tau) f(t))$, where $*_t$ indicates convolution over the variable t, and $h(t)$ is the impulse response function (i.e. inverse Laplace transform of the transfer function).

Proceeding with our derivation of the spatio-temporal transfers, for simplicity we first consider the two linear time-frequency transforms. Let the "hat" operator correspond to either the generalized STFT or the WT. That is,

$$\widehat{f_{detrend}}(\omega,\tau) \quad := \quad \mathrm{STFT}_{f_{detrend}}(\omega,\tau;T) \quad \text{or} \quad \mathrm{WT}_{f_{detrend}}(\omega,\tau). \tag{2.21}$$

Then, assuming that the constraints on the detrending operation given in equations 2.19 and 2.20 are satisfied, one can (nontrivially) show the effect on a time-derivative, $(\partial_t f)$, of a detrending operation followed by a linear time-frequency transform:

$$\widehat{(\partial_t f)_{detrend}}(\omega,\tau) = \partial_\tau \widehat{f_{detrend}}(\omega,\tau) + i g(\omega) \widehat{f_{detrend}}(\omega,\tau), \tag{2.22}$$

where $g(\omega)$ is a real-valued function ($g(\omega) \equiv 0$ for wavelets and our version of the STFT, but $g(\omega) \equiv \pm\omega$ for other reasonable STFT definitions). Upon multiplying equation 2.22 by $\widehat{f_{detrend}}^*(\omega,\tau)$ and taking the real part, the extra term drops out, yielding

$$\mathrm{Re}[\widehat{f_{detrend}}^* \widehat{(\partial_t f)_{detrend}}(\omega,\tau)] = \partial_\tau \tfrac{1}{2} |\widehat{f_{detrend}}(\omega,\tau)|^2. \tag{2.23}$$

If one substitutes $k\widetilde{\psi}(\boldsymbol{k},t)$ for $f(t)$ in equation 2.23 and applies the result to our example equation of motion 2.8, one obtains the spatio-temporal spectral energy budget:

$$\begin{aligned} \frac{\partial}{\partial\tau} E(\boldsymbol{k},\omega,\tau) := \frac{\partial}{\partial\tau} \tfrac{1}{2} k^2 \left| \widehat{\widetilde{\psi}_{detrend}} \right|^2 = \mathrm{Re} &\left[\left(\widehat{\widetilde{\psi}^*_{detrend}} \right) \left(\widehat{\widetilde{J(\psi, \nabla^2\psi)}_{detrend}} \right) \right] \\ - \mathrm{Re} &\left[\widehat{\widetilde{\psi}^*_{detrend}} \widehat{\widetilde{D}_{detrend}} \right] \\ - \mathrm{Re} &\left[\widehat{\widetilde{\psi}^*_{detrend}} \widehat{\widetilde{F}_{detrend}} \right], \end{aligned} \tag{2.24}$$

and an additional multiplicative factor of k^2 gives the enstrophy budget. Because the spatial Fourier transformation commutes with both the detrending operation and the time-frequency transform, in equation 2.24 the "tilde" operator can be applied before the detrend, after the detrend, or after the "hat" operator. However, the order of the detrend and the "hat" operator certainly does matter.

Note that the detrending operation in equation 2.24 acts on the nonlinear term J but *not* on the stream function itself. In general, because

$$\left(J(\widehat{\widetilde{\psi, \nabla^2\psi)}}_{detrend} \right) \neq \left(J(\psi_{detrend}, \widehat{\widetilde{\nabla^2\psi_{detrend}}}) \right), \tag{2.25}$$

it would be wrong to detrend the raw data (e.g. the stream function) before calculating the nonlinear term if one wants to rigorously interpret the result as a spatial-temporal transfer. Of course, approximate equality in equation 2.25 might hold for some datasets.

Finally, as our main result, we return to general bilinear time-frequency representations and the general formulation of the original equation of motion. Given the equation of motion 2.6, the constraints on the detrending operation (equations 2.19 and 2.20), and a bilinear time-frequency transformation TFR_f of the form 2.16, one obtains the following spatio-temporal spectral budget:

$$\frac{\partial}{\partial\tau}\mathrm{TFR}_{G_{detrend}}(\boldsymbol{\chi}, \tau, \omega) = \sum_n \mathcal{A}_n(\boldsymbol{\chi}, \tau, \omega), \tag{2.26}$$

where $\mathcal{A}_n(\boldsymbol{\chi}, \tau, \omega)$ is the *spatio-temporal spectral transfer* corresponding to A_n, defined by

$$\begin{aligned} \mathcal{A}_n(\boldsymbol{\chi}, \tau, \omega) := & \int_{-\infty}^{\infty}\int_{-\infty}^{\infty} d\tau' dt\, K(\tau - \tau', t, \omega) \\ & \times \left\{ A_{n,detrend}\left(\boldsymbol{\chi}, \tau' + \frac{t}{2}, \tau\right) G^*_{detrend}\left(\boldsymbol{\chi}, \tau' - \frac{t}{2}, \tau\right) \right. \\ & \left. + G_{detrend}\left(\boldsymbol{\chi}, \tau' + \frac{t}{2}, \tau\right) A^*_{n,detrend}\left(\boldsymbol{\chi}, \tau' - \frac{t}{2}, \tau\right) \right\}. \end{aligned} \tag{2.27}$$

2.2.5 Spectral transfers in ω-space and in other reduced spaces

Other spectral budgets can be derived by summing (or integrating) equation 2.24 or 2.27 over subsets of $(\boldsymbol{k}, \omega, \tau)$- or $(\boldsymbol{\chi}, \omega, \tau)$-space. In particular, the temporal spectral transfers, which we will diagnose in Chapter III, are obtained by summing the spatio-temporal energy budget 2.24 and the corresponding enstrophy budget over all wavevectors:

$$\frac{\partial}{\partial \tau} \mathcal{S}_E(\omega, \tau) := \sum_{\boldsymbol{k}} \frac{\partial}{\partial \tau} E(\boldsymbol{k}, \omega, \tau) \tag{2.28}$$

$$= \sum_{\boldsymbol{k}} \mathrm{Re}[\widehat{\widetilde{\psi}}^* [\widehat{\widetilde{J(\psi, \nabla^2 \psi)}}] - \sum_{\boldsymbol{k}} \mathrm{Re}[\widehat{\widetilde{\psi}}^* \widehat{\widetilde{D}}] - \sum_{\boldsymbol{k}} \mathrm{Re}[\widehat{\widetilde{\psi}}^* \widehat{\widetilde{F}}], \tag{2.29}$$

$$\frac{\partial}{\partial \tau} \mathcal{S}_Z(\omega, \tau) := \sum_{\boldsymbol{k}} \frac{\partial}{\partial \tau} Z(\boldsymbol{k}, \omega, \tau) = \sum_{\boldsymbol{k}} k^2 \frac{\partial}{\partial \tau} E(\boldsymbol{k}, \omega, \tau), \tag{2.30}$$

where $\mathcal{S}_E(\omega, \tau)$ and $\mathcal{S}_Z(\omega, \tau)$ are the temporal spectral densities (at central time τ) for energy and enstrophy, respectively, and each of the three terms on the right hand side of (2.29) is a *temporal spectral transfer*, which in general we write as $\mathcal{A}_n(\omega, \tau)$ or simply $\mathcal{A}(\omega, \tau)$. We define temporal spectral *fluxes* as integrals of the temporal spectral transfers:

$$\Pi^{>}_{\mathcal{A}}(\omega, \tau) := \int\limits_{|\omega'| > \omega} d\omega' \; \mathcal{A}(\omega', \tau), \quad \text{or} \quad \Pi^{>}_{\mathcal{A}}(\omega) := \int\limits_{|\omega'| > \omega} d\omega' \; \mathcal{A}(\omega'). \tag{2.31}$$

If instead one integrates equation 2.24 over all ω or all (ω, τ), one obtains a second form for the spectral densities in $\boldsymbol{k}$-space:

$$E_{(2)}(\boldsymbol{k}, \tau) := \int d\omega \; E(\boldsymbol{k}, \omega, \tau), \tag{2.32}$$

$$\mathcal{E}_{(2)}(\boldsymbol{k}) := \frac{1}{\tau_1 - \tau_0} \int\limits_{\tau_0}^{\tau_1} d\tau \; E_{(2)}(\boldsymbol{k}, \tau), \tag{2.33}$$

where the interval (τ_0, τ_1) spans the whole dataset. For a general time-frequency transform, this second form may or may not equal the commonly used spectral densities $E_{(1)}(\boldsymbol{k})$ and $Z_{(1)}(\boldsymbol{k})$ defined in section 2.2.2. However, if one uses the STFT, due to Parseval's theorem, the two forms will give nearly equal results if the effects of windowing and detrending are negligible.

2.3 Properties of Fourier transform-based spectral transfers for fluid flows

2.3.1 The effect of a Galilean transformation on spectral transfers

We now show how the spatio-temporal and temporal transfers change under a Galilean transformation, which is roughly equivalent to the imposition of a mean flow. Such a transformation is important because many flows of practical interest either exhibit a strong mean flow or are thought to exhibit sweeping, in which the smaller-scale structures are swept without distortion by larger-scale structures.

The effect of a Galilean transformation differs from the effect of a mean flow whenever there is a forcing term that sets a preferred frame of reference (as is typically the case). Therefore, it is not strictly correct to take the results of this section as an indication of the effect of a mean flow. However, so far as some spectral transfers, or at least certain regions in $(\boldsymbol{k}, \omega)$-space of some spectral transfers, are independent of the temporal properties of the forcing term (as will indeed be the case in our numerical simulations), the analysis below should hold reasonably well.

Suppose we have two frames of reference, in which the Eulerian velocity fields are $\boldsymbol{u}^{(1)}$ and $\boldsymbol{u}^{(2)}$, and that $\boldsymbol{V}$ is the (constant) velocity of the second frame with respect to the first, so that

$$\boldsymbol{u}^{(2)}(\boldsymbol{x}, t) = \boldsymbol{u}^{(1)}(\boldsymbol{x} + \boldsymbol{V}t, t) - \boldsymbol{V}, \tag{2.34}$$

$$\boldsymbol{f}^{(2)}(\boldsymbol{x}, t) = \boldsymbol{f}^{(1)}(\boldsymbol{x} + \boldsymbol{V}t, t). \tag{2.35}$$

Trivially, but as a means of setting notation, the energy budgets in frames (1) and (2) take the form

$$\frac{\partial}{\partial \tau} E^{(n)}(\boldsymbol{k}, \omega, \tau; T) = \mathcal{N}^{(n)}(\boldsymbol{k}, \omega, \tau; T) - \mathcal{D}^{(n)}(\boldsymbol{k}, \omega, \tau; T) - \mathcal{F}^{(n)}(\boldsymbol{k}, \omega, \tau; T), \tag{2.36}$$

where $\mathcal{N}$, $\mathcal{D}$, and $\mathcal{F}$ correspond to the nonlinear transfer, dissipation, and forcing terms respectively in the energy budget equation 2.24, and where $n = 1, 2$ labels the reference frame.

If the STFT is chosen, it can be shown that each term transforms according to

$$\mathcal{A}^{(2)}(\boldsymbol{k}, \omega, \tau; T) = \mathcal{A}^{(1)}(\boldsymbol{k}, \omega + \boldsymbol{V} \cdot \boldsymbol{k}, \tau; T), \tag{2.37}$$

where $\mathcal{A} = \mathcal{N}, \mathcal{D}, \mathcal{F}$, or $\partial_\tau E$. The transformation of each term is simply a $\boldsymbol{k}$-dependent shift in the frequency variable. The enstrophy transfer terms transform in the same way. Note that equation 2.37 is an exact equality regardless of the choice of temporal window or detrending operation.

After integrating over all spectral angles in $\boldsymbol{k}$-space in order to obtain $\mathcal{A}(k, \omega, \tau)$, or after summing over all $\boldsymbol{k}$ to obtain $\mathcal{A}(\omega, \tau)$, one finds the transformation rules

$$\mathcal{A}^{(2)}(k, \omega, \tau; T) := \int d\Omega_d \, k^{d-1} \mathcal{A}^{(2)}(\boldsymbol{k}, \omega, \tau; T) \tag{2.38}$$

$$= \int d\Omega_d \, k^{d-1} \mathcal{A}^{(1)}(\boldsymbol{k}, \omega + \boldsymbol{V} \cdot \boldsymbol{k}, \tau; T), \tag{2.39}$$

$$\mathcal{A}^{(2)}(\omega, \tau; T) := \sum_{\boldsymbol{k}} \mathcal{A}^{(2)}(\boldsymbol{k}, \omega, \tau; T) = \sum_{\boldsymbol{k}} \mathcal{A}^{(1)}(\boldsymbol{k}, \omega + \boldsymbol{V} \cdot \boldsymbol{k}, \tau; T) \tag{2.40}$$

where the integrals in (2.38) and (2.39) are over all angles in d-dimensional $\boldsymbol{k}$-space.

According to equations 2.39 and 2.40 the spectral content in mode ω in frame (2) corresponds to a sum of the spectral content over a range of wavevector-frequency modes in frame (1). Above some sufficiently high wavenumber (say, $k >_{max}$), the transfers $\mathcal{A}^{(1)}(\boldsymbol{k}, \omega', \tau; T)$ contribute negligibly to the sum 2.40, so the frequency modes ω' which contribute non-negligibly to the sum are restricted to the range $\omega - k_{max}V < \omega' < \omega + k_{max}V$, where one should note that k_{max} may depend on ω. Thus, the effect of a mean flow is to "smear" out each frequency mode into nearby frequency–wavenumber modes. This smearing of the temporal and spatio-temporal transfers can be avoided by choosing to work in a frame with zero mean velocity. However, even in a frame with zero mean velocity there will still be smearing effects evident in the transfers if "sweeping" plays an important role in the dynamics, as discussed in the next section.

2.3.2 The effect of sweeping on spectral transfers

As was alluded to at the end of the previous section, the effect of sweeping on the spectral transfers is expected to "smear" some hypothetical non-swept version of the spectral transfer into the spectral transfer that is ultimately observed. We attempt to provide a little more rigor to the statement above in this section. We provide a simple model for the effect of sweeping on the spectral transfers in the case of statistically stationary, homogeneous isotropic turbulence.

Suppose that there is some distribution of sweeping velocities $\boldsymbol{V}$ with probability density $p(\boldsymbol{V})$ and that at time t the whole fluid can be modeled as having a mean velocity $\boldsymbol{V}(t)$. Also assume that $\boldsymbol{V}(t)$ (as well as its higher order derivatives) changes "slowly" in time. A sufficient condition for the first derivative is that $(T/2)^2|\boldsymbol{k} \cdot \boldsymbol{V}'(\tau)| \ll 1$, which may be derived by Taylor expanding $\boldsymbol{V}(\tau + \Delta t)$ around τ with $\Delta t < T/2$. Then, according to equation 2.37, which assumes we are using the STFT,

$$\mathcal{A}^{(2)}(\boldsymbol{k}, \omega, \tau; T) \approx \mathcal{A}^{(1)}(\boldsymbol{k}, \omega + \boldsymbol{V}(\tau) \cdot \boldsymbol{k}, \tau; T), \tag{2.41}$$

where $\mathcal{A}^{(1)}$ is the spectral transfer in the reference frame in which the mean velocity is zero at time τ. We also assume that the sweeping is isotropic, i.e. $p(\boldsymbol{V}) = p(V)$, where $V = |\boldsymbol{V}|$.

Assuming that the fluid is in a statistically steady state, and taking this to imply that $\mathcal{A}^{(1)}(\boldsymbol{k}, \omega, \tau; T)$ is independent of τ, we may average equation 2.41 over a very wide range of τ to obtain

$$\begin{aligned}
\langle \mathcal{A}^{(2)}(\boldsymbol{k}, \omega, \tau; T)\rangle_\tau &:= \frac{1}{\tau_1 - \tau_0} \int_{\tau_0}^{\tau_1} d\tau \, \mathcal{A}^{(2)}(\boldsymbol{k}, \omega, \tau; T) && (2.42)\\
&\approx \frac{1}{\tau_1 - \tau_0} \int_{\tau_0}^{\tau_1} d\tau \, \mathcal{A}^{(1)}(\boldsymbol{k}, \omega + \boldsymbol{V}(\tau) \cdot \boldsymbol{k}, \tau_0; T) && (2.43)\\
&\approx \int d^dV \, p(\boldsymbol{V}) \mathcal{A}^{(1)}(\boldsymbol{k}, \omega + \boldsymbol{V} \cdot \boldsymbol{k}, \tau_0; T), && (2.44)
\end{aligned}$$

where the width of the integration domain, $\tau_1 - \tau_0 \gg T$, is assumed wide enough to allow the change of integration variable made in equation 2.44. The change of integration variables is allowed by assuming ergodicity.

Now assume that the fluid is statistically homogeneous and isotropic, which implies that that $\mathcal{A}^{(1)}(\boldsymbol{k}, \omega, \tau; T) = \mathcal{A}^{(1)}(k, \omega, \tau; T)/s_d(k)$, where $s_d(k) = 2\pi k$ in two dimensions and $s_d(k) = 4\pi k^2$ in three dimensions. Then equation 2.44 further reduces to

$$\begin{aligned}
\langle \mathcal{A}^{(2)}(k, \omega, \tau; T)\rangle_\tau &\approx \int d^dV \, p(\boldsymbol{V}) \, \mathcal{A}^{(1)}(k, \omega + \boldsymbol{V} \cdot \boldsymbol{k}, \tau_0; T) && (2.45)\\
&= \frac{1}{\pi} \int_0^\pi d\theta'_k \int d^dV \, p(\boldsymbol{V}) \mathcal{A}^{(1)}(k, \omega + Vk\cos\theta'_k, \tau_0; T) && (2.46)\\
&= \frac{1}{\pi} \int_{-1}^{1} \frac{d\epsilon'}{\sqrt{1 - \epsilon'^2}} \int d^dV \, p(\boldsymbol{V}) \mathcal{A}^{(1)}(k, \omega + Vk\epsilon' . \tau_0; T). && (2.47)
\end{aligned}$$

To get equation (2.46) we used the assumption that $p(\boldsymbol{V}) = p(V)$ is radially symmetric, so that the value of the integral does not change if we also average over all angles θ'_k, where $\boldsymbol{V} \cdot \boldsymbol{k} = Vk\cos\theta'_k$. In equation (2.47) the dummy variable $\epsilon' := \cos\theta'_k$ is not necessarily small.

If k is sufficiently large, then the integrands of equations 2.45 and 2.47 are non-negligible only when $\epsilon' \approx 0$, in which case

$$\langle \mathcal{A}^{(2)}(k,\omega,\tau;T)\rangle_\tau \approx \frac{1}{\pi}\int_{-\epsilon}^{\epsilon} d\epsilon' \int d^dV\; p(\boldsymbol{V})\mathcal{A}^{(1)}(k,\omega+Vk\epsilon',\tau_0;T) \tag{2.48}$$

$$= \frac{1}{\pi}\int d^dV\; p(\boldsymbol{V}) \int_{-Vk\epsilon}^{Vk\epsilon} d\omega' \frac{1}{Vk}\mathcal{A}^{(1)}(k,\omega+\omega',\tau_0;T) \tag{2.49}$$

$$\approx \frac{1}{\pi}\int d^dV\; p(\boldsymbol{V}) \int_{-\infty}^{\infty} d\omega' \frac{1}{Vk}\mathcal{A}^{(1)}(k,\omega+\omega',\tau_0;T) \tag{2.50}$$

$$= \frac{1}{\pi k}\mathcal{A}^{(1)}_{(2)}(k,\tau_0;T)\int d^dV\; \frac{p(\boldsymbol{V})}{V} \tag{2.51}$$

$$= \frac{1}{\pi k}\mathcal{A}^{(2)}_{(2)}(k,\tau_0;T)\int d^dV\; \frac{p(\boldsymbol{V})}{V} \tag{2.52}$$

where in the final result $\mathcal{A}^{(2)}_{(2)}(k,\tau_0;T)$ is simply the spatial spectral transfer corresponding to the spatial spectral densities $E_{(2)}(k,\tau)$ defined in equation 2.32. The last equality (equation 2.52) is due to the fact that the spatial spectral densities are the same in any frame.

Several assumptions were made to justify the approximations in the derivation of $\langle \mathcal{A}^{(2)}(k,\omega,\tau;T)\rangle_\tau$ at large k. The approximation in equation 2.48 holds whenever $Vk\epsilon > \omega_{max}(k)$ for some choice of $\epsilon \ll 1$ (in other words, $Vk \gg \omega_{max}$), where $\omega_{max}(k)$ is some possibly k-dependent cutoff frequency above which contributions to the total $\int d\omega\; \mathcal{A}^{(1)}(k,\omega,\tau_0;T)$ are negligible. The approximation in equation 2.50 holds whenever $|\omega| \pm Vk\epsilon > \omega_{max}$, so it suffices to require that $|\omega| < 2\omega_{max}$ in addition to the already mentioned requirements for equation 2.48. Since V is an integration variable, we note that in these inequalities V must be interpreted as some minimum velocity V_{min} below which the total probability $\int_{V<V_{min}} d^dV\; p(\boldsymbol{V})$ is sufficiently small.

Thus, we have shown that when $k \gg \omega_{max}(k)/V_{min}$ and $\omega < 2\omega_{max}$ the spectral transfers in (k,ω)-space become ω-independent and scale as $1/k$ times the spectral transfers in k-space. In that case the smearing of frequency modes of $\mathcal{A}^{(1)}(k,\omega,\tau_0;T)$

into frequency modes of $\mathcal{A}^{(2)}(k, \omega, \tau_0; T)$ covers such a wide range of frequencies that every frequency in $\mathcal{A}^{(1)}(k, \omega, \tau_0; T)$ contributes to each frequency in $\mathcal{A}^{(2)}(k, \omega, \tau_0; T)$ in a uniform way. For regions of (k, ω)-space that do not satisfy the given inequalities, the smearing of the frequency modes occurs across only nearby frequency modes in a non-uniform way quantified by equation 2.45.

Finally, we address two possible problems with our somewhat naive model of sweeping, and we suggest potential resolutions for these problems. The first problem is that we assumed that the whole fluid could be modeled with a single slowly changing, spatially independent mean velocity $\boldsymbol{V}(t)$. However, the idea behind sweeping is that the smaller scales (high wavenumbers) are swept not by the average velocity of the whole fluid, but by the average velocity over local regions of the fluid. The spatial spectral transfers calculated over the entire domain *do not* in general equal the sum of the spatial spectral transfers in the subdomains, that is, unless there is significant decoherence between the subdomains so that the cross-terms are negligible. When using the spatial Fourier transform, it would seem that we have no choice but to hope that is the case, and one can indeed argue that it should be. Perhaps a spatially localized transform (say, a spatial wavelet) may be better suited for any analysis of sweeping.

The second problem is that the window duration T was limited according to the rate of change of the sweeping velocity: $(T/2)^2 \max_\tau k|\partial_\tau V(\tau)| \ll 1$. One would also like to know the effects of sweeping on transfers calculated using windows with greater duration. Again, as with the problem in the spatial domain, the answer depends on the existence of a level of decoherence between appropriately narrow windows. On the one hand, it again seems that a wavelet analysis might be a more appropriate choice. On the other hand, there very well may be significant decoherence between time intervals, as could be checked by numerical experiment, in which case the Fourier transform may be perfectly acceptable or even preferable due to its widespread use and efficient numerical implementation. To put it in quantitative terms, we suspect and later numerically show that typically $\mathcal{A}^{(2)}(k, \omega, \tau_0; T_{large}) \approx \langle \mathcal{A}^{(2)}(k, \omega, \tau; T) \rangle_\tau$, where T_{large} is some window length significantly wider than the narrow window length T required in the above analysis.

2.3.3 Triad interactions, conservation laws, and non-locality

This section addresses the question of whether spatial triad interactions, understood in terms of spatial spectral transfers, can be suitably generalized to spatio-temporal triad interactions, understood in terms of spatio-temporal spectral transfers. Spatio-temporal triad interactions are already widely used in the literature, but in a subtly different way than is used here. The difference is that our spatio-temporal (and temporal) triad interactions can be interpreted as transferring energy between the various frequency modes as the central time changes, whereas spatio-temporal triads in the literature typically make no reference to a central time and therefore have a different interpretation. We also address the effects of mean flows and isotropic sweeping on spatio-temporal and temporal triad interactions in this section.

We define spatio-temporal and temporal triad interactions in terms of the STFT with no detrending operation. General time-frequency representations and detrending operations will not work, because the construction of triads explicitly makes use of a convolution theorem. One finds that detailed conservation still holds for the temporal and spatio-temporal triad interactions as it does for the spatial triad interactions. However, one cannot show that energy and enstrophy temporal fluxes must have opposite sign (i.e. the dual cascade) as was shown for spatial fluxes in *Kraichnan* (1967). Moreover, one can show that the presence of either a mean flow or isotropic sweeping turns local temporal transfers into non-local temporal transfers if high wavenumber modes are involved. For these reasons, the dual cascade picture might make less sense in frequency space than it does in wavenumber space. That said, the temporal and spatio-temporal triad interactions should not be simply discounted as being explained away by sweeping, because only triad interactions involving high wavenumbers are significantly affected by sweeping, and the low-wavenumber, low-frequency modes of the flow are also of dynamical interest.

We now make some of the above statements more precise. If one chooses to use the STFT with no detrending operation, the spatio-temporal spectral transfer due to the nonlinear advection term in equation 2.24 can be written (making the functional dependence of the STFT on the window σ explicit) as

$$\begin{aligned} N[\sigma](\boldsymbol{k},\omega,\tau;T) &:= \mathrm{Re}[\widehat{\widetilde{\psi}}^*[\widehat{\widetilde{J(\psi,\nabla^2\psi)}}[\sigma](\boldsymbol{k},\omega,\tau;T)] && (2.53) \\ &= \frac{1}{2}\sum_{\boldsymbol{p},\boldsymbol{q}}\int d\omega_{\boldsymbol{p}}\int d\omega_{\boldsymbol{q}}\, T[\sigma](\boldsymbol{k},\boldsymbol{p},\boldsymbol{q},\omega,\omega_{\boldsymbol{p}},\omega_{\boldsymbol{q}})\delta_{\boldsymbol{k}-\boldsymbol{p}-\boldsymbol{q},\boldsymbol{0}}\delta(\omega-\omega_{\boldsymbol{p}}-\omega_{\boldsymbol{q}}), && (2.54) \end{aligned}$$

where,

$$\begin{aligned} T[\sigma](\boldsymbol{k},\boldsymbol{p},\boldsymbol{q},&\omega,\omega_{\boldsymbol{p}},\omega_{\boldsymbol{q}}) := (\delta_{ij}k_m - k_ik_jk_m/k^2) && (2.55) \\ &\times \mathrm{Im}[\widehat{\widetilde{u}}_i^*[\sigma](\boldsymbol{k},\omega,\tau;T)\widehat{\widetilde{u}}_j[\sigma_1](\boldsymbol{p},\omega_{\boldsymbol{p}},\tau;T)\widehat{\widetilde{u}}_m[\sigma_2](\boldsymbol{q},\omega_{\boldsymbol{q}},\tau;T)], \end{aligned}$$

and σ_1 and σ_2 are window functions such that $\sigma_1\sigma_2 = \sigma$. Equations 2.53–2.62 follow the treatment of spatial triad interections by (*Kraichnan*, 1967). In that study and here, $T(\boldsymbol{k},\boldsymbol{p},\boldsymbol{q})$ is the rate of energy injection into wavevector mode $\boldsymbol{k}$ due to nonlinear interaction with modes $\boldsymbol{p}$ and $\boldsymbol{q}$. Defined only here, $T(\boldsymbol{k},\boldsymbol{p},\boldsymbol{q},\omega_{\boldsymbol{k}},\omega_{\boldsymbol{p}},\omega_{\boldsymbol{q}})$ is the rate of energy injection into wavevector-frequency mode $(\boldsymbol{k},\omega_{\boldsymbol{k}})$ due to nonlinear interaction with modes $(\boldsymbol{p},\omega_{\boldsymbol{p}})$ and $(\boldsymbol{q},\omega_{\boldsymbol{q}})$.

The spatial energy transfers $T(\boldsymbol{k},\boldsymbol{p},\boldsymbol{q})$ can be obtained from the spatio-temporal transfers $T(\boldsymbol{k},\boldsymbol{p},\boldsymbol{q},\omega_{\boldsymbol{k}},\omega_{\boldsymbol{p}},\omega_{\boldsymbol{q}})$ by integrating over all frequencies ($\omega_{\boldsymbol{k}}$, $\omega_{\boldsymbol{p}}$, $\omega_{\boldsymbol{q}}$), which may be proved using Parseval's theorem. We define temporal energy transfers by summing the spatio-temporal transfers over all wavevectors:

$$T(\omega_{\boldsymbol{k}}, \omega_{\boldsymbol{p}}, \omega_{\boldsymbol{q}}) := \sum_{\boldsymbol{k},\boldsymbol{p},\boldsymbol{q}} T(\boldsymbol{k}, \boldsymbol{p}, \boldsymbol{q}, \omega_{\boldsymbol{k}}, \omega_{\boldsymbol{p}}, \omega_{\boldsymbol{q}}). \tag{2.56}$$

The spatio-temporal enstrophy transfers can be written in terms of the spatio-temporal energy transfers:

$$T_{enstrophy}(\boldsymbol{k}, \boldsymbol{p}, \boldsymbol{q}, \omega_{\boldsymbol{k}}, \omega_{\boldsymbol{p}}, \omega_{\boldsymbol{q}}) := k^2 T(\boldsymbol{k}, \boldsymbol{p}, \boldsymbol{q}, \omega_{\boldsymbol{k}}, \omega_{\boldsymbol{p}}, \omega_{\boldsymbol{q}}). \tag{2.57}$$

The spatial enstropy transfers,

$$\begin{align} T_{enstrophy}(\boldsymbol{k}, \boldsymbol{p}, \boldsymbol{q}) &:= \sum_{\omega_{\boldsymbol{k}},\omega_{\boldsymbol{p}},\omega_{\boldsymbol{q}}} k^2 T(\boldsymbol{k}, \boldsymbol{p}, \boldsymbol{q}, \omega_{\boldsymbol{k}}, \omega_{\boldsymbol{p}}, \omega_{\boldsymbol{q}}) \tag{2.58} \\ &= k^2 T(\boldsymbol{k}, \boldsymbol{p}, \boldsymbol{q}), \tag{2.59} \end{align}$$

are straightforwardly related to the spatial energy transfers $T(\boldsymbol{k}, \boldsymbol{p}, \boldsymbol{q})$. However, the temporal enstrophy transfers

$$T_{enstrophy}(\omega_{\boldsymbol{k}}, \omega_{\boldsymbol{p}}, \omega_{\boldsymbol{q}}) := \sum_{\boldsymbol{k},\boldsymbol{p},\boldsymbol{q}} k^2 T(\boldsymbol{k}, \boldsymbol{p}, \boldsymbol{q}, \omega_{\boldsymbol{k}}, \omega_{\boldsymbol{p}}, \omega_{\boldsymbol{q}}) \tag{2.60}$$

have no clear relation to the temporal energy transfers $T(\omega_{\boldsymbol{k}}, \omega_{\boldsymbol{p}}, \omega_{\boldsymbol{q}})$. This lack of a connection between $T(\omega_{\boldsymbol{k}}, \omega_{\boldsymbol{p}}, \omega_{\boldsymbol{q}})$ and $T_{enstrophy}(\omega_{\boldsymbol{k}}, \omega_{\boldsymbol{p}}, \omega_{\boldsymbol{q}})$ implies that we cannot prove that energy and enstrophy must be transferred in opposite directions in ω-space in the same way that one proves that energy and enstrophy must be transferred in opposite dicetions in k-space (*Kraichnan*, 1967).

One can verify detailed energy and enstrophy conservation for spatio-temporal triad interactions:

$$T(\boldsymbol{k},\boldsymbol{p},\boldsymbol{q},\omega_{\boldsymbol{k}},\omega_{\boldsymbol{p}},\omega_{\boldsymbol{q}})+T(\boldsymbol{p},\boldsymbol{q},\boldsymbol{k},\omega_{\boldsymbol{p}},\omega_{\boldsymbol{q}},\omega_{\boldsymbol{k}})+T(\boldsymbol{q},\boldsymbol{k},\boldsymbol{p},\omega_{\boldsymbol{q}},\omega_{\boldsymbol{k}},\omega_{\boldsymbol{p}})\equiv 0, \tag{2.61}$$

$$k^2T(\boldsymbol{k},\boldsymbol{p},\boldsymbol{q},\omega_{\boldsymbol{k}},\omega_{\boldsymbol{p}},\omega_{\boldsymbol{q}})+p^2T(\boldsymbol{p},\boldsymbol{q},\boldsymbol{k},\omega_{\boldsymbol{p}},\omega_{\boldsymbol{q}},\omega_{\boldsymbol{k}})+q^2T(\boldsymbol{q},\boldsymbol{k},\boldsymbol{p},\omega_{\boldsymbol{q}},\omega_{\boldsymbol{k}},\omega_{\boldsymbol{p}})\equiv 0. \tag{2.62}$$

By summing over all $(\boldsymbol{k},\boldsymbol{p},\boldsymbol{q})$ one also obtains detailed energy and enstrophy conservation for the temporal triad interactions as well:

$$T(\omega_{\boldsymbol{k}},\omega_{\boldsymbol{p}},\omega_{\boldsymbol{q}})+T(\omega_{\boldsymbol{p}},\omega_{\boldsymbol{q}},\omega_{\boldsymbol{k}})+T(\omega_{\boldsymbol{q}},\omega_{\boldsymbol{k}},\omega_{\boldsymbol{p}})\equiv 0, \tag{2.63}$$

$$T_{enstrophy}(\omega_{\boldsymbol{k}},\omega_{\boldsymbol{p}},\omega_{\boldsymbol{q}})+T_{enstrophy}(\omega_{\boldsymbol{p}},\omega_{\boldsymbol{q}},\omega_{\boldsymbol{k}})+T_{enstrophy}(\omega_{\boldsymbol{q}},\omega_{\boldsymbol{k}},\omega_{\boldsymbol{p}})\equiv 0. \tag{2.64}$$

Thus, temporal and spatio-temporal triad interactions are similar to spatial triad interactions in terms of following detailed conservation laws.

The effect of a Galilean transformation (or, roughly equivalently, the effect of imposing a mean flow) on the spatio-temporal triad interaction in equation 2.55 is

$$T^{(2)}(\boldsymbol{k},\boldsymbol{p},\boldsymbol{q},\omega_{\boldsymbol{k}},\omega_{\boldsymbol{p}},\omega_{\boldsymbol{q}})=T^{(1)}(\boldsymbol{k},\boldsymbol{p},\boldsymbol{q},\omega_{\boldsymbol{k}}+\boldsymbol{V}\cdot\boldsymbol{k},\omega_{\boldsymbol{p}}+\boldsymbol{V}\cdot\boldsymbol{p},\omega_{\boldsymbol{q}}+\boldsymbol{V}\cdot\boldsymbol{q}), \tag{2.65}$$

where $\boldsymbol{V}$ is the velocity of reference frame (2) in frame (1). The main implication of equation 2.65 is that temporal triad interactions may be made to be more non-local by the imposition of a mean flow or sweeping. This should be expected as it has long been known (*Tennekes*, 1975) that in the presence of sweeping, Kolmogorov-type arguments cannot be made for frequency spectra as they are made for wavenumber spectra, at least at sufficiently high wavenumber.

In the case of spatially isotropic sweeping, one may gain insight into the resulting transfer by integrating equation 2.65 over all directions of $\boldsymbol{V}$ while holding the magnitude $V = |\boldsymbol{V}|$ constant. More general sweeping velocity distributions may be handled by linear superposition. Suppose that the transfer in the absence of sweeping (i.e. in frame 1) takes non-zero values only on the triad $(\boldsymbol{K}_1, \boldsymbol{K}_2, \boldsymbol{K}_3, \Omega_1, \Omega_2, \Omega_3)$, and let the sweeping velocity take the form

$$\boldsymbol{V} = V\cos(\phi)\cos(\theta)\widehat{\boldsymbol{x}} + V\cos(\phi)\sin(\theta)\widehat{\boldsymbol{y}} + V\sin(\phi)\widehat{\boldsymbol{z}}, \tag{2.66}$$

where ϕ is the angle between $\boldsymbol{V}$ and the plane defined by the triad $(\boldsymbol{K}_1, \boldsymbol{K}_2, \boldsymbol{K}_3)$, and θ is the angle between $\boldsymbol{K}_1$ and the projection of $\boldsymbol{V}$ onto that plane.

Restricting the analysis to two spatial dimensions, so that $\phi = 0$, the effect of integrating equation 2.65 over all θ (i.e. the effect of isotropic sweeping) is to redistribute the transfer at $(\Omega_1, \Omega_2, \Omega_3)$ onto a circle in $(\omega_{\boldsymbol{k}}, \omega_{\boldsymbol{p}}, \omega_{\boldsymbol{q}})$-space centered at $(\Omega_1, \Omega_2, \Omega_3)$, with the circle lying in the plane defined by $\omega_{\boldsymbol{k}} = \omega_{\boldsymbol{p}} + \omega_{\boldsymbol{q}}$. In that plane, one may define an orthonormal coordinate system with components (ω'_1, ω'_2) given by $\omega'_1 = \sqrt{3/2}(\omega_{\boldsymbol{p}} + \omega_{\boldsymbol{q}}) = \sqrt{3/2}\omega_{\boldsymbol{k}}$ and $\omega'_2 = \sqrt{1/2}(\omega_{\boldsymbol{p}} - \omega_{\boldsymbol{q}})$. The radius of the circle in the ω'_1-ω'_2 plane is

$$3V\frac{|\boldsymbol{K}_+ \times \boldsymbol{K}_-|}{(K_+^2 + K_-^2)^{1/2}} = \frac{3\sqrt{3}}{2}V\frac{|\boldsymbol{K}_2 \times \boldsymbol{K}_3|}{(K_2^2 + K_3^2 + \boldsymbol{K}_2 \cdot \boldsymbol{K}_3)^{1/2}}, \tag{2.67}$$

where $\boldsymbol{K}_+ := (\boldsymbol{K}_2 + \boldsymbol{K}_3)/\sqrt{2}$ and $\boldsymbol{K}_- := (\boldsymbol{K}_2 - \boldsymbol{K}_3)/\sqrt{6}$. Thus, when $\boldsymbol{K}_2$ and $\boldsymbol{K}_3$ are nearly collinear, the radius is nearly zero, which implies that sweeping has little effect. At the other extreme, when $(\boldsymbol{K}_1, \boldsymbol{K}_2, \boldsymbol{K}_3)$ forms an equilateral triangle, the radius is maximized, in which case sweeping has maximal effect.

The three-dimensional case is a simple extension of the two-dimensional case. In three dimensions the effect of integrating over all θ is to form a circle in the ω'_1-ω'_2 plane exactly as in the two-dimensional case, except that V is replaced by $V\cos(\phi)$. So, upon integrating over all ϕ, the interior of the circle is filled as well, albeit non-uniformly with lowest density near the center of the circle.

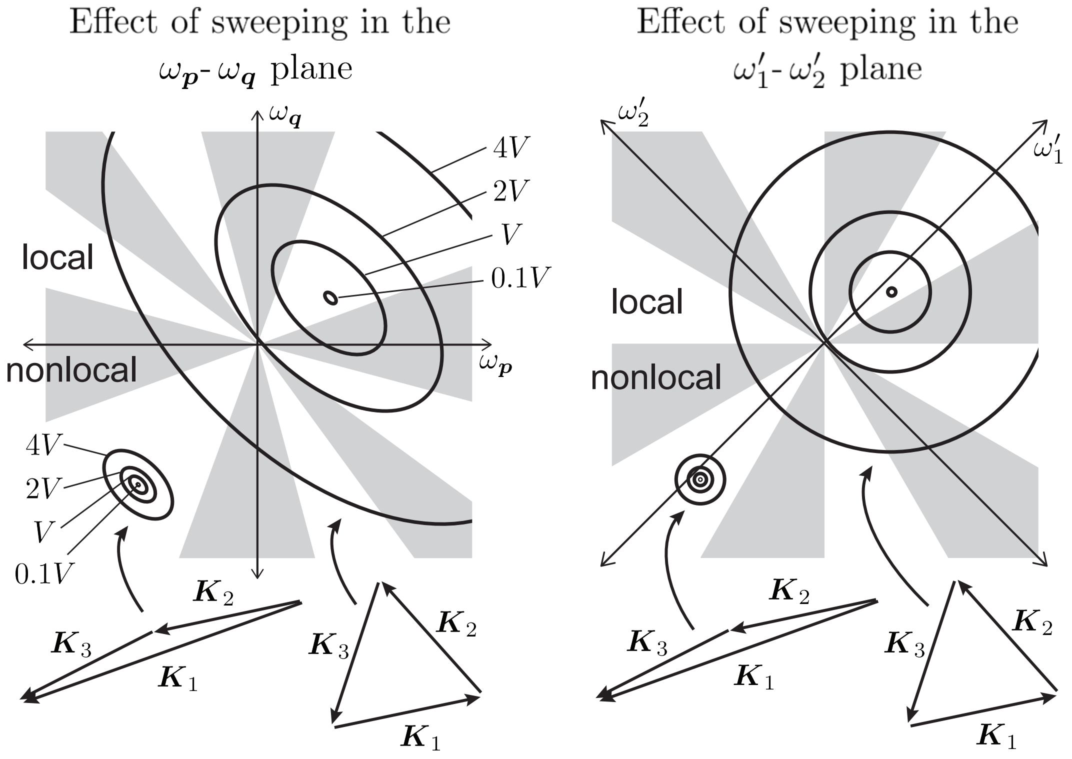

Effect of sweeping in the $\omega_{\boldsymbol{p}}$-$\omega_{\boldsymbol{q}}$ plane

Effect of sweeping in the ω'_1-ω'_2 plane

Figure 2.1: The effect of isotropic sweeping on spatio-temporal triad interactions for two different spatial triads ($\boldsymbol{K}_1, \boldsymbol{K}_2, \boldsymbol{K}_3$). Triad interactions get redistributed onto circles in the (ω'_1, ω'_2)-plane, which is defined by $\omega_{\boldsymbol{k}} = \omega_{\boldsymbol{p}} + \omega_{\boldsymbol{q}}$. The redistributed transfers are shown for four different sweeping velocities $(0.1V, V, 2V, 4V)$ and are projected onto the $(\omega_{\boldsymbol{p}}, \omega_{\boldsymbol{q}})$-plane (left) and shown in the (ω'_1, ω'_2)-plane (right). Regions of each plane that correspond to nonlocal temporal triad interactions (as define by equation 2.68) are shaded. The effect of sweeping by a sufficiently high velocity is to redistribute any given transfer onto a wide array of local and nonlocal transfers. The effect of sweeping on the temporal triad is maximal when the spatial triad is most local.

Figure 2.1 shows the effect of several sweeping velocities on two different spatio-temporal triads: one with a nearly collinear spatial triad and the other with an equilateral spatial triad. The figure shows the projection of the swept transfers onto the $\omega_{\boldsymbol{p}}$-$\omega_{\boldsymbol{q}}$ plane as well as the swept transfers in the ω_1'-ω_2' plane. Shaded regions correspond to nonlocal temporal triads, while unshaded regions correspond to local temporal triads. We define as "local" any temporal triad $(\omega_{\boldsymbol{k}}, \omega_{\boldsymbol{p}}, \omega_{\boldsymbol{q}})$ that satisfies

$$\gamma := \frac{\max(|\omega_{\boldsymbol{k}}|, |\omega_{\boldsymbol{p}}|, |\omega_{\boldsymbol{q}}|)}{\min(|\omega_{\boldsymbol{k}}|, |\omega_{\boldsymbol{p}}|, |\omega_{\boldsymbol{q}}|)} < 3, \tag{2.68}$$

and we note that temporal triads are inherently more nonlocal than spatial triads due to the fact that frequencies are scalars. That is to say, while it is possible to simultaneously satisfy $|\boldsymbol{k}|=|\boldsymbol{p}|=|\boldsymbol{q}|$ and $\boldsymbol{k} = \boldsymbol{p} + \boldsymbol{q}$, it is not possible to satisfy both $|\omega_{\boldsymbol{k}}| = |\omega_{\boldsymbol{p}}| = |\omega_{\boldsymbol{q}}|$ and $\omega_{\boldsymbol{k}} = \omega_{\boldsymbol{p}} + \omega_{\boldsymbol{q}}$. Moreover, the most "local" any temporal triad can possibly be is to have $\gamma = 2$, as defined by (2.68); hence our choice of $\gamma < 3$ as our definition of locality.

According to (2.67), the radii of the circles in the ω_1'-ω_2' plane are directly proportional to the sweeping velocity V and the size K of the spatial triad. Thus for sufficiently large V or K, the circle will be large enough to encompass many regions of locality and nonlocality in the ω_1'-ω_2' plane, causing any originally local temporal triad to be distributed into an equal number of local and nonlocal triads. Of course, there is also dependence on the shape of the spatial triad. Interestingly, it is precisely the most local spatial triads that exhibit the greatest temporal nonlocality due to sweeping, while the most nonlocal spatial triads remain unaffected by sweeping.

It may be possible to test for the sweeping hypothesis by observing the spatio-temporal spectral transfers in the ω_1'-ω_2' plane for several different spatial triads and checking whether the observed transfers are consistent with a single sweeping velocity distribution. Such a diagnostic would take into account more dynamical information than would, say, a simple comparison of the slopes of the spatial and temporal spectral densities.

2.3.4 Interpretation of spatio-temporal and temporal spectral transfers

We now interpret the spatio-temporal and temporal spectral transfers based on the theory in this chapter. Additional interpretation of the transfers based on two-dimensional turbulence simulations can be found in chapter III.

First of all, the spatio-temporal spectral transfers $\mathcal{A}(\boldsymbol{k}, \omega, \tau)$ give the τ-time rate of change of spectral density $E(\boldsymbol{k}, \omega, \tau)$ in wavenumber-frequency mode $(\boldsymbol{k}, \omega)$ straightforwardly analogous to how the spatial spectral transfers give the t-time rate of change of the spectral energy density $E(\boldsymbol{k}, t)$. Summing over wavevectors $\boldsymbol{k}$, the temporal spectral transfers $\mathcal{A}(\omega, \tau)$ give the τ-time rate of change of the spectral density $\mathcal{S}_E(\omega, \tau)$, as defined in equation 2.28. The same can be said for enstrophy, of course.

Imagine forcing a fluid at some well-defined wavenumber-frequency pair (k_F, ω_F), with the initial fluid being at rest. Consider the spatial spectral transfer $\mathcal{N}(\boldsymbol{k}, t)$ corresponding to the nonlinear advection term. In the standard spatial cascade picture we expect at early times to see $\mathcal{N}(\boldsymbol{k}, t)$ take energy out of the forcing wavevectors and inject it into nearby wavevectors, according to triad locality, and then further on toward the dissipation scale, during which time the fluid is non-stationary and has a net injection by $\mathcal{N}(\boldsymbol{k}, t)$ of energy into the inertial range. After a statistically stationary state has been reached, there should be little time-averaged net injection of energy or enstrophy at each wavevector in the inertial ranges: $\langle \mathcal{N}(\boldsymbol{k}, t) \rangle \approx 0$ for $\boldsymbol{k}$ in an inertial range, while the time-averaged spatial transfer $\langle \mathcal{N}(\boldsymbol{k}, t) \rangle$ should be non-zero in the dissipation range and the forcing range such that the sum of all the time-averaged transfer terms equals zero (due to statistical stationarity and assumed ergodicity).

That picture mostly holds true for the spatio-temporal spectral transfers $\mathcal{N}(\boldsymbol{k}, \omega, \tau)$

and $\mathcal{N}(\omega, \tau)$ as well. At early times we might expect energy and enstrophy injected spectrally near the forcing region $(|\boldsymbol{k}|, |\omega|) \approx (k_F, \omega_F)$, that is, assuming that ω_F is not so high that the fluid cannot respond accordingly. At intermediate times τ there should be a positive net injection $\mathcal{N}(\boldsymbol{k}, \omega, \tau)$ at intermediate wavenumber-frequency pairs between the forcing scales and the dissipation scales. After a statistically stationary state has been reached, there should be no net injection outside of the forcing and dissipation ranges. The caveat here is that there is no guarantee of temporal triad locality. Indeed, spatio-temporal triad non-locality is expected at the highest wavenumbers due to the sweeping hypothesis. This issue is important to bear in mind if one is tempted to think of the spatial transfers and temporal transfers as fully analogous – they are not in this one crucial way.

2.4 Conclusion

We have shown how temporal and spatio-temporal spectral transfers in fluid turbulence may be defined quite generally in terms of time-frequency analysis methods such as the short time Fourier transform, or wavelet analysis, or more general time-frequency transforms. Moreover, the standard time-frequency analysis methods can be modified to include a fairly general detrending operation in such a way that the temporal and spatio-temporal spectral budgets remain exact even after detrending. The most general definition of spatio-temporal spectral transfers was given by (2.26) and (2.27) .

We derived various theoretical properties of temporal and spatio-temporal spectral transfers, including the effect of a mean flow and the effect of “sweeping” in the case of homogeneous isotropic turbulence, where the effect is to widen the temporal spectral transfers, consistent with wide temporal spectral fluxes observed in satellite altimeter data, idealized model output, and realistic model output by *Arbic et al.* (2012, 2014). We showed that analogous to results for spatial spectral transfers, we may for temporal and spatio-temporal spectral transfers properly define triad interactions, derive local conservation laws, and discuss locality versus non-locality of the triad interactions in frequency space. We also quantified how sweeping typically makes the temporal triad interactions more non-local than spatial triad interactions.

The issue of locality versus nonlocality of triad interactions is particularly important when discussing temporal or spatio-temporal fluxes. One might be inclined to think of fluxes as arising from a local operator, but in k- or ω- or (k, ω)-space a flux is almost always a non-local functional of the spectral quantity of interest. In three dimensions this operator is expected to be somewhat narrow in k, and in two dimensions a bit wider. However, the operator could be significantly wider in ω due to sweeping. One should always keep this in mind when diagnosing spectral transfers and fluxes in the frequency domain.

CHAPTER III

Wavenumber-frequency spectral transfers: two-dimensional turbulence simulations

3.1 Overview of this Chapter

As an illustrative example of the use of spatio-temporal spectral transfers, we show their application to a simple fluid system: a modified version of the incompressible two-dimensional Navier–Stokes equation, as discussed in the Introduction. This chapter has three parts: Numerical setup, Numerical results, and Conclusion.

In the Numerical setup (section 3.2) we describe our pseudo-spectral simulations of two-dimensional turbulence forced stochastically and dissipated at both large and small spatial scales. In the Numerical results (section 3.3), we diagnose the spatial, temporal, and spatio-temporal spectral transfers and fluxes for these simulations. We show how various limitations of the data may affect the diagnosis of the transfers. Such limitations include poor temporal resolution, inadequate duration of the dataset, and the existence of a trend. We show that for our two-dimensional simulations the temporal transfers and fluxes are fairly robust when applied to imperfect data. We also show how the temporal spectral transfers change in time starting with a fluid at rest, diagnose the effects of detrending, and look for evidence of sweeping in the spatio-temporal spectral transfers. In the Conclusion (section 3.4) we provide further discussion along with a brief summary of the key results.

3.2 Numerical setup

3.2.1 The equation of motion

We numerically simulate the two-dimensional Navier–Stokes equations (in the vorticity formulation) modified by a general dissipation and a forcing term. In spectral space, assuming spatially periodic boundary conditions, the simulated equation takes the following form:

$$\frac{\partial}{\partial t} k^2 \widetilde{\psi}(\boldsymbol{k}, t) = \widetilde{J(\psi, \nabla^2 \psi)}(\boldsymbol{k}, t) - \widetilde{D}(\boldsymbol{k}, t) - \widetilde{F}(\boldsymbol{k}, t), \tag{3.1}$$

where the forcing term $\widetilde{F}$ and the dissipation term $\widetilde{D}$ will be described below. The width of the square, periodic domain is L.

3.2.2 The choice of forcing

Just as studies of the wavenumber cascade in two-dimensional turbulence tend to employ a forcing that is narrowband in wavenumber, here we choose a forcing that is narrowband in *both* wavenumber and frequency. We do so by starting with a stochastic forcing that has a spectral peak at $\omega = 0$, and then shifting the spectral peak via multiplication by $e^{i\omega_F t}$ in the temporal domain, where ω_F is the forcing frequency. We add to that a second (statistically independent, but otherwise identical) forcing shifted via multiplication by $e^{-i\omega_F t}$. The result is a forcing that produces statistically stationary turbulence.

For the initial choice of stochastic forcing we use a version of the force first used by *Lilly* (1969), but slightly modified to be statistically radially symmetric in wavenumber as in *Maltrud and Vallis* (1991). For each wavevector $\boldsymbol{k}$, the force at

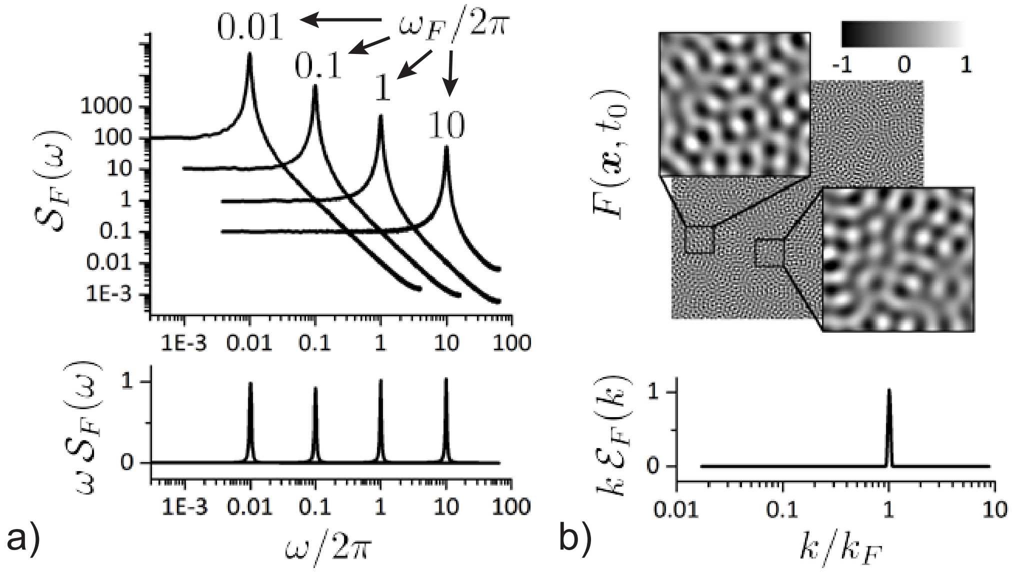

Figure 3.1: Spectral properties of the forcing. (a) Temporal spectral densities $\mathcal{S}_F(\omega)$ of the four different forcing frequencies plotted as log-log (top) and area-preserving spectral densities $\omega\mathcal{S}_F(\omega)$ plotted as semi-log (bottom). (b) Snapshot of the forcing $F(\boldsymbol{x}, t_0)$ at initial time (top) and the corresponding area-preserving spatial spectral density $k\mathcal{E}_F(k)$ (bottom), which was the same for all four forcing frequencies. Vertical axes have arbitrary units.

time-step n is defined in terms of the force at the previous time-step as follows:

$$\widetilde{F}_0^{\pm}(\boldsymbol{k}, t_n) = R\widetilde{F}_0^{\pm}(\boldsymbol{k}, t_{n-1}) + f_0(\boldsymbol{k})\sqrt{1-R^2}e^{i\phi_n^{\pm}(\boldsymbol{k})}, \tag{3.2}$$

where $\{\phi_n^{\pm}(\boldsymbol{k})\}_{n=0}^{\infty}$ is a set of independent, identically distributed random phases on the interval $[0, 2\pi)$. The ± superscript indicates that we are defining two (statistically independent) forcing terms $\widetilde{F}_0^{+}$ and $\widetilde{F}_0^{-}$. This forcing has two adjustable parameters: the real-valued function $f_0(\boldsymbol{k})$ controls the expected magnitude of the forcing, and $R \in [0, 1]$ controls the integral time scale of the forcing. The case $R = 0$ corresponds to white noise forcing, while the case $R = 1$ corresponds to constant forcing. The integral time scale of $\widetilde{F}_0^{\pm}$ is $\tau_{F_0} = 0.5\Delta t(1 + R)/(1 - R)$, where Δt is length of a single time-step. The power spectrum of $\widetilde{F}_0^{\pm}$ is centered at $\omega = 0$ and takes the shape roughly of a Lorentzian.

The forcing used in the numerical simulations is constructed from $\widetilde{F}_0^{+}$ and $\widetilde{F}_0^{-}$ through a shifting of their spectral peaks by $\pm\omega_F$ as described earlier. Thus, the forcing term in equation 3.1 is given by

$$\widetilde{F}(\boldsymbol{k}, t) := \widetilde{F}_0^{+}(\boldsymbol{k}, t)e^{+i\omega_F t} + \widetilde{F}_0^{-}(\boldsymbol{k}, t)e^{-i\omega_F t}. \tag{3.3}$$

One can show that the integral time scale of F is the same as for $F_0^{\pm}$ (i.e. $\tau_F = \tau_{F_0}$). In order to obtain a sharp spectral peak in the power spectrum of the forcing, the integral time scale τ_F must be set sufficiently large relative to the forcing period $2\pi/\omega_F$. We found that $\tau_F = 5 \times 2\pi/\omega_F$ was sufficient for producing a narrow peak, and all of our simulations use that parameter choice. The $\boldsymbol{k}$-dependent forcing amplitude was set to $f_0(\boldsymbol{k}) := ((k_F + \Delta k_F)^2 - k^2)(k^2 - (k_F - \Delta k_F)^2)$ in the range $k_F - \Delta k_F < k < k_F + \Delta k_F$ and $f_0(\boldsymbol{k}) := 0$ for all other k. In our simulations, which had a resolution of 1024^2, we chose $(L/2\pi)k_F = 59$ and $(L/2\pi)\Delta k_F = 4$, which provided roughly one decade (in k-space) each for the development of the energy and enstrophy cascades. Figure 3.1

shows the temporal and spatial spectral densities of the forcing for each the four forcing frequencies ω_F used in this Chapter. For the time-frequency analysis method we used a STFT having a Tukey window with $\sigma_T(t) = 1$ for ninety percent of the full length of the dataset. Figure 3.1 also shows a snapshot of the forcing in physical space for comparison with snapshots of stream function and vorticity shown later in the results section.

Instead of choosing a forcing that is narrowband in frequency, we could have chosen a forcing such that the energy and enstrophy *injection rates* would be narrowband in frequency. In particular we could have defined either $\widetilde{F_0^{\pm}}(\boldsymbol{k}, t) = a^{\pm}(\boldsymbol{k})/\psi^*(\boldsymbol{k}, t)$ or $\widetilde{F_0^{\pm}}(\boldsymbol{k}, t) = b^{\pm}(\boldsymbol{k})\psi(\boldsymbol{k}, t)/\sum_{\boldsymbol{k}} b(\boldsymbol{k})|\psi(\boldsymbol{k}, t)|^2$, the former having been used in *Chen et al.* (2003, 2006) to obtain constant energy injection with $\omega_F = 0$. We chose not to use this type of forcing out of concern for the effects on the spatio-temporal transfers, particularly at high forcing frequencies. It should not be possible to inject energy or enstrophy at arbitrarily high frequencies due to the natural response time-scales of the fluid.

3.2.3 The choice of dissipation

Because simulations are done pseudo-spectrally, we allow a general dissipation term in the form of a wavenumber filter. Thus, instead of multiplication of Fourier mode $\widetilde{\boldsymbol{u}}(\boldsymbol{k}, t)$ by a hyperviscosity term $\nu_n k^{2(n+1)}$ (corresponding to $\nu_n(-\nabla^2)^{n+1}$ in physical space) we allow multiplication by an arbitrary function $f_{diss}(\boldsymbol{k})$. We choose to have the dissipation term in equation 3.1 take the form

$$\widetilde{D}(\boldsymbol{k}, t) := f_{diss}(\boldsymbol{k}) k^2 \widetilde{\psi}(\boldsymbol{k}, t), \tag{3.4}$$

$$f_{diss}(\boldsymbol{k}) := \sum_m \nu_m \begin{cases} (k - k_m)^{|m|}, & k > k_m \quad (m > 0) \\ (k^{-1} - k_m^{-1})^{|m|}, & k < k_m \quad (m < 0) \\ 0, & \text{otherwise.} \end{cases} \tag{3.5}$$

Typically in simulations of 2D turbulence, both a hyperviscosity ($m > 1, \nu_m \neq 0, k_m = 0$) and an inverse viscosity ($m < 0, \nu_m \neq 0, k_m = \infty$) are employed for the purpose of obtaining wider inertial ranges. While it has been shown that these unphysical dissipation terms affect the statistics in the inertial range near the dissipation range (*Lamorgese et al.*, 2005; *Frisch et al.*, 2008; *Bos and Bertoglio*, 2009), for our purpose here we think it to be more important to obtain wide inertial ranges given our limited resolution. To that end, the inertial ranges are extended even further by replacing the hyper- and inverse viscosities by high wavenumber filters ($m > 0$) and "inverse" wavenumber filters ($m < 0$), as defined by equation 3.5. These wavenumber filters depend not only on the exponent m but also on a "cutoff" wavenumber k_m below ($m > 0$) or above ($m < 0$) which there is no dissipation. We report only on our simulations that used these wavenumber filters with cutoffs, because the spatial spectral transfers were cleaner and the inertial ranges were wider than in our simulations that utilized unmodified hyper- or inverse viscosities.

The values of the parameters in equation 3.5 were set to $\nu_8 = 1.3 \times 10^{-11}, k_6 = 366 \approx 0.715 k_N, \nu_{-6} = 1.2 \times 10^9, k_{-6} = 7.9 \approx 0.0154 k_N$, where k_N is the Nyquist wavenumber. All other viscosity parameters were set equal to zero. The cut-off wavenumber for the inverse wavenumber filter was chosen sufficiently high so that the stream function would not be significantly spatially correlated with itself halfway across the domain. Because the cut-off wavenumber was $k_{-6} = 7.9$, the largest structures in the stream function were smaller than the domain size by about a factor of eight. This choice was made in order to be reasonably confident that the lowest frequencies observed in the system were not appreciably affected by the spatial periodicity.

3.2.4 Simulation method and other numerical details

For the numerics we used a parallelized pseudo-spectral method (*Canuto et al.*, 2007a,b), with domain size $L = 2\pi$ and a spatial resolution of 1024^2. Because we needed to save snapshots of vorticity frequently for temporal statistics, we did not increase the spatial resolution further due to data storage limitations. Even at a spatial resolution of only 1024^2 we analyzed over 100 terabytes of data.

Most runs were not fully de-aliased, but the wavenumber filter removed practically all enstrophy at wavenumbers larger than 5/6 times the Nyquist wavenumber. A single fully de-aliased simulation was conducted for comparison, and there was no significant change in the results. The time-stepping increment was either $\Delta t = 2^{-12}$ or 2^{-13} for all runs.

The vorticity was iterated using third-order Adams–Bashforth time-stepping, while the forcing term was iterated separately using Euler's method with a smaller time step. While technically the inclusion of a stochastic forcing term changes the strong (root-mean-square) convergence of the numerical scheme from third order to first order, the error is better represented by $O(\Delta t^3 + \Delta t/M)$, where M is the ratio of the vorticity-term time step to the forcing-term time step. This effectively third-order numerical scheme (for sufficiently large M) bears a resemblance to other schemes developed for stochastic systems with small noise (*Buckwar and Winkler*, 2006, 2007, and references therein). We found that $M = 1$ was actually sufficient for the convergence of all statistics we present.

3.3 Numerical results

3.3.1 Overview of the results section

In this section we show the results of our numerical simulations. We show first the spatial, temporal, and spatio-temporal spectral transfers and fluxes of energy and enstrophy in statistically equilibrated simulations of two-dimensional turbulence forced at four different frequencies (section 3.3.2). To test the robustness of the diagnostic, we then show the effects of varying the window size and sampling rate on the numerically calculated spectral transfers (section 3.3.3). We also show the effect of detrending on temporal spectral fluxes when the simulation output is non-stationary (section 3.3.4). Lastly, we examine spatio-temporal spectral transfers in the dissipation ranges in order to detect the effects of isotropic sweeping (section 3.3.5) predicted in Chapter II.

3.3.2 Effects of varying the forcing frequency

We simulate the two-dimensional vorticity equation 3.1 for four different choices of the forcing frequency, $\omega_F/2\pi \in \{0.01, 0.1, 1, 10\}$, with corresponding integral time scales of $\tau_F = 5 \times 2\pi/\omega_F$. We will discuss nondimensionalization of the time scale in the next two paragraphs. All other parameters are held constant, with numerical values as described in section 3.2. Figure 3.2 shows snapshots of vorticity and stream function, taken after the simulation had reached a statistically steady state, for three of the runs ($\omega_F/2\pi = 0.01$, 1, and 10). The snapshots of vorticity and stream function for the three lowest forcing frequencies ($\omega_F/2\pi = 0.01$, 0.1, and 1) are quite similar, with the exception that the run forced at the lowest frequency ($\omega_f/2\pi = 0.01$) exhibits slightly larger vortices than the other runs. The run forced at the highest frequency ($\omega_F/2\pi = 10$) is significantly less energetic (with a root mean square velocity approximately a factor of five lower) than the other three runs, but otherwise looked qualitatively similar.

There is some freedom in choosing how to nondimensionalize the time scale in this system. We compute two different natural frequencies and show the results in table 3.1. Following the literature on modulated turbulence, the first natural time

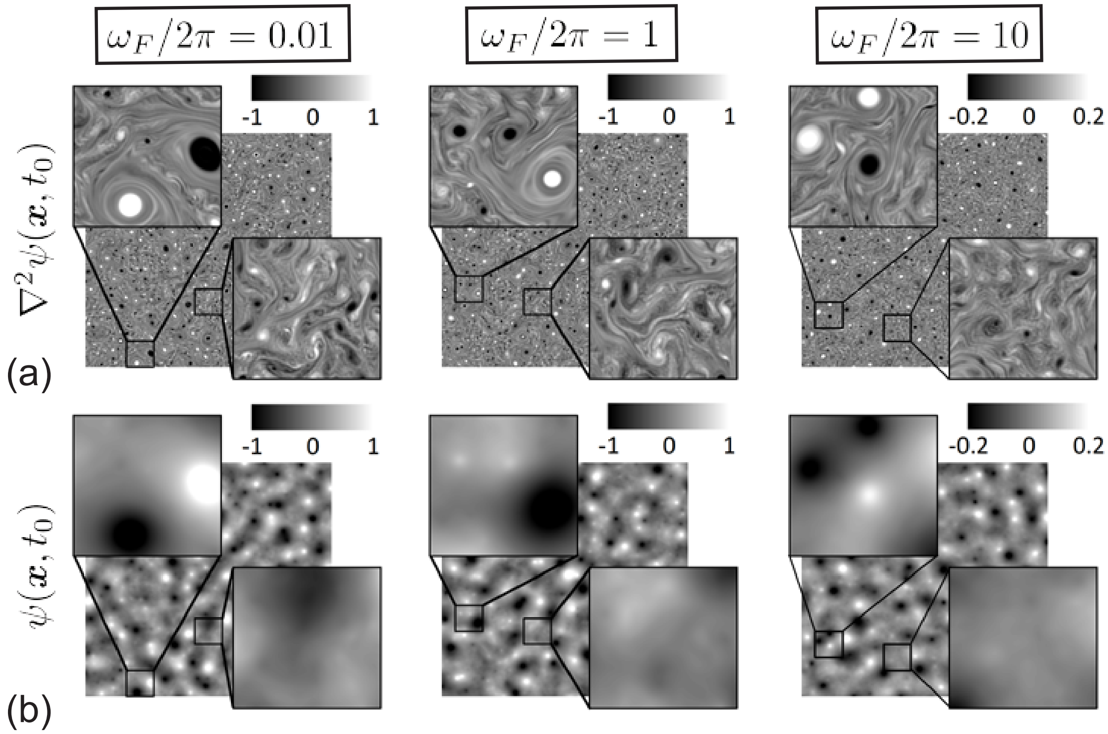

Figure 3.2: Streamfunction and vorticity snapshots. (a) Snapshots of vorticity $\nabla^2\psi(\boldsymbol{x}, t_0)$ at time t_0, taken after statistical equilibrium has been reached for three of the four forcing frequencies. Two magnified (6x) insets are chosen to show regions with and without strong vortices. The vorticity snapshot for the missing forcing frequency ($\omega_F/2\pi = 0.1$) is visually and quantitatively similar to the case $\omega_F/2\pi = 1$. Note the decreased range of scale in the rightmost plots ($\omega_F/2\pi = 10$). (b) Snapshots of stream function $\psi(\boldsymbol{x}, t_0)$ with magnified insets corresponding to the vorticity snapshots above.

scale and corresponding natural frequency is

$$t_{nat} = \frac{c}{\langle|\boldsymbol{u}|\rangle k_F/2\pi} \implies \frac{\omega_{nat}}{2\pi} = \frac{\langle|\boldsymbol{u}|\rangle k_F/2\pi}{c}, \quad c \gtrsim 1, \tag{3.6}$$

where c is some nondimensional constant, $\langle|\boldsymbol{u}|\rangle$ is the average Eulerian speed, and k_F is the forcing wavenumber. The three-dimensional modulated turbulence literature suggests a value of $c = 2.7$ (*von der Heydt et al.*, 2003), yielding a time scale "of the cascade process." We choose a value of c is based on the $\omega_F/2\pi = 10$ simulations. In the $\omega_F/2\pi = 10$ runs, energy and enstrophy are injected not at the forcing frequency but rather within a range of lower frequencies (as can be seen in figure 3.3 or more easily in figure 3.4), centered at a frequency which we take to be the natural frequency of the fluid at the forcing scale. Inserting this frequency into equation 3.6 sets the value $c = 2.0$, which we use for all of our runs. For the simulations forced at the three lowest frequencies, the natural frequency is consistently $\omega_{nat} = 2.0$ in dimensional units. For the simulation forced at the highest frequency the natural frequency is only $\omega_{nat} = 0.4$. Because we would like a scale time by a consistent factor in all simulations, we define the constant $\omega^*_{nat} = 2.0$.

We define the second natural frequency in terms of the locations of the energy and enstrophy dissipation ranges in frequency space. In all of our simulations, energy is dissipated over a wide range of relatively low frequencies while enstrophy is dissipated over a wide range of higher frequencies. Motivated by the notion that a natural forcing frequency should lie between the two dissipation ranges, we define the natural frequency $\omega_{diss}/2\pi$ as the frequency that best divides the ranges. Because the edges of the dissipation ranges in our simulations overlap slightly in frequency, $\omega_{diss}/2\pi$ is easily approximated. For the simulations forced at the three lowest frequencies, the natural frequency consistently lies within the range 0.4–1.0 in dimensional units. For the simulation forced at the highest frequency the natural frequency lies within

$\omega_F/2\pi$	$\omega_{nat}/2\pi$	$\omega_{diss}/2\pi$	$\omega^*_{nat}/2\pi$	$\omega^*_{diss}/2\pi$	ω_F/ω^*_{nat}	ω_F/ω^*_{diss}
0.01	2.0	0.4–1.0	2.0	0.63	0.005	0.016
0.1	2.0	0.4–1.0	2.0	0.63	0.05	0.16
1	2.0	0.4–1.0	2.0	0.63	0.5	1.6
10	0.4	0.08–0.2	2.0	0.63	5.0	16

Table 3.1: Nondimensionalized forcing frequencies. For each forcing frequency $\omega_F/2\pi$, this table shows the corresponding natural frequency $\omega_{nat}/2\pi = 0.5\langle|\boldsymbol{u}|\rangle k_F/2\pi$ as well as an alternative natural frequency $\omega_{diss}/2\pi$ defined as the frequency below which energy is dissipated and above which enstrophy is dissipated. The resulting nondimensionalized forcing frequencies ω_F/ω^*_{nat} and ω_F/ω^*_{diss} are shown in the rightmost columns.

the range 0.08–0.2 in dimensional units (again a factor of five less). In order to nondimensionalize time by a scale factor that is constant over all runs, we define $\omega^*_{diss} = 0.63$ based on the geometric mean of the observed range of natural frequencies for the three lowest forcing frequencies.

To summarize the previous two paragraphs and table 3.1, we have two nondimensionalizations of the time scale in this system. The former gives nondimensional forcing frequencies $\omega_F/\omega^*_{nat} \in \{0.005, 0.05, 0.5, 5\}$ while the latter gives nondimensional forcing frequencies $\omega_F/\omega^*_{diss} \in \{0.016, 0.16, 1.6, 16\}$. Because the dimensional values of $\omega_F/2\pi \in \{0.01, 0.1, 1, 10\}$ lie between these two possibilities, we simply show all results in terms of the dimensional time scale. We indicate one or both of the natural frequencies in later figures where appropriate.

Moving on to the analysis of model output, for each of the four forcing frequencies three datasets (each approximately one terabyte in size) are created by sampling the simulation at three different sampling rates. The longer simulations are sampled less frequently such that $32,768$ snapshots are saved for each dataset. For each dataset the window size used in calculating the spectral transfers is equal to the entire length of the dataset. Thus, the calculated spectral transfers take the form $\mathcal{A}(\boldsymbol{k}, \omega, t_{max}/2; t_{max})$ with $t_{max} \in \{256, 1024, 4096\}$.

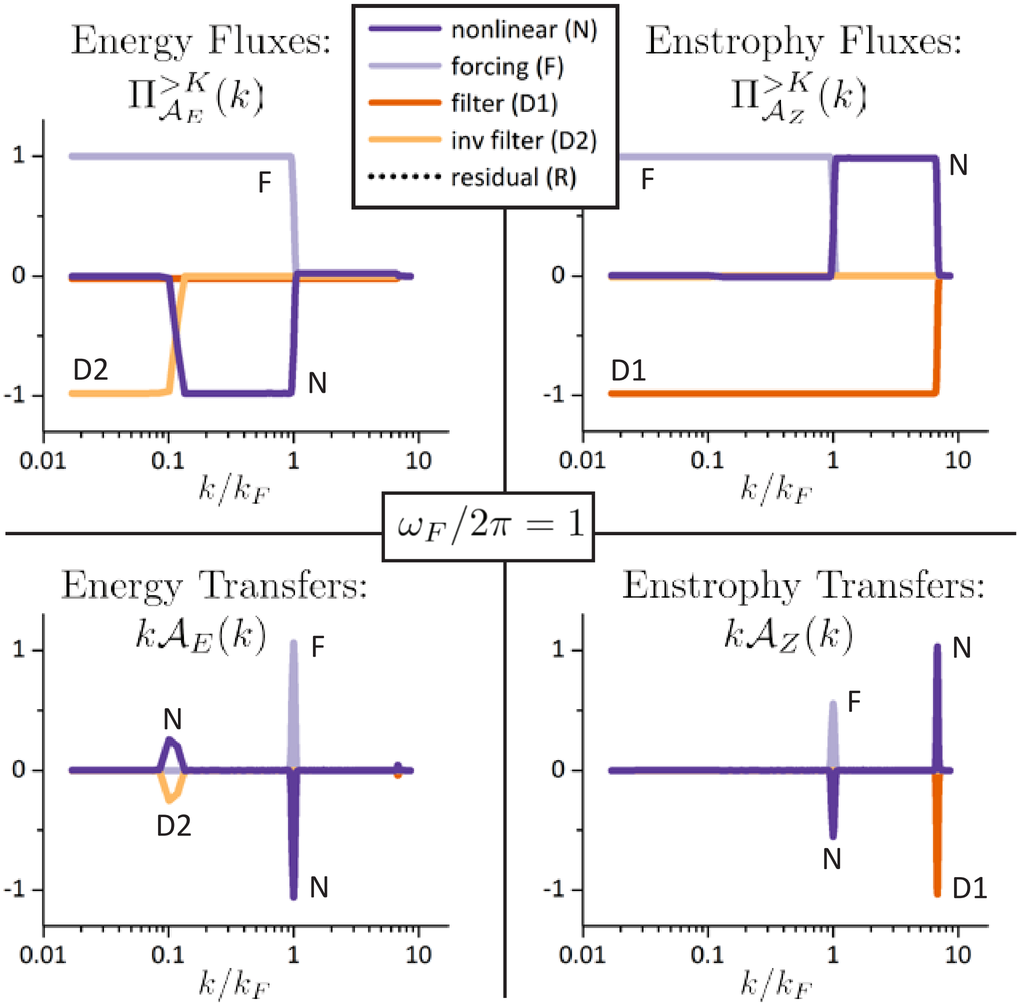

Figure 3.3: Spatial spectral fluxes and transfers. Spatial spectral fluxes "$\Pi^{>K}_{\mathcal{A}}(k)$ vs. k" (top row) of energy and enstrophy (left to right); and the corresponding spatial spectral transfers "$\mathcal{A}(k)$ vs. k" (bottom row); where $\mathcal{A} = \mathcal{N}$, $\mathcal{F}$, $\mathcal{D}_1$ and $\mathcal{D}_2$ are the nonlinear, forcing, filter, and inverse-filter terms, respectively, in the spatial spectral budgets of energy and enstrophy for the $\omega_F/2\pi = 1$ simulation. The fluxes and transfers have been averaged over 32, 768 snapshots. A negatively sloping flux corresponds to a positive transfer, while a positively sloping flux corresponds to a negative transfer.

Figure 3.3 shows the spatial spectral transfers and fluxes for one of the four forcing frequencies ($\omega_F/2\pi = 1$). While the theory presented earlier in this paper focuses primarily on spectral transfers, we show both transfers and fluxes because some readers will be more familiar with spectral fluxes. We also note that many readers will be accustomed to seeing much "noisier" spatial spectral transfers. Our transfers are quite smooth because we average over a very large number of snapshots. We follow the convention that a positive transfer at wavenumber k corresponds to the injection of energy (or enstrophy) at that wavenumber. The convention we follow in the definition of fluxes (equation 2.11) implies that a positive flux corresponds to a downscale transfer (direct cascade) to larger k, and a negative flux corresponds to an upscale transfer (inverse cascade) to smaller k. We note that the spatial spectral transfers and fluxes for the other three forcing frequencies are qualitatively similar, with the main difference being that the run forced at the highest frequency exhibited transfers and fluxes of smaller magnitude.

As expected for two-dimensional turbulence, we see that, regardless of the forcing frequency, energy is injected at spatial scale $2\pi/k_F$ and transferred to larger spatial scales where it is dissipated by the inverse wavenumber filter. Similarly, enstrophy is injected at spatial scale $2\pi/k_F$ and transferred to smaller spatial scales where it is dissipated by the wavenumber filter. Other studies have shown that the spatial transfers are somewhat local, so that energy (or enstrophy) may be considered to "cascade" from spatial-scale to neighboring spatial-scale up (or down) to the dissipation length-scale, in which case the notion of a "flux through spatial scale $2\pi/k$" makes sense. Because the *temporal* spectral fluxes shown next are less local, it may be useful to think of the corresponding transfers when viewing the fluxes.

The temporal spectral transfers and fluxes are shown in Figure 3.4. The second and third columns show the energy and enstrophy fluxes respectively, while the first column shows the corresponding energy transfers (plotted in area-preserving format) for the highest two forcing frequencies. We show the results for all three sampling rates on each plot. There is a large degree of agreement for the results with the different sampling rates, except at the highest and lowest frequencies resolved by each dataset, as must be the case. The large degree of agreement indicates that the temporal spectral transfers and fluxes are reasonably robust diagnostics for datasets that resolve most but not all dynamical time scales.

We are somewhat hesitant to show the temporal results as spectral fluxes rather than spectral transfers, because we think the use of fluxes may bias one's intuition regarding the "locality" of the temporal transfers in ω-space. However, the plots of temporal spectral transfers typically exhibit high spectral peaks at the forcing frequencies, making it difficult to show spectral transfers at other frequencies on the same plot. Moreover, when there is aliasing at high frequencies due to low sampling rates, the temporal spectral transfers tend to be noisy while the temporal spectral fluxes tend to be smooth. Therefore, for graphical clarity we show mainly spectral fluxes here and elsewhere in the results section.

As seen in figure 3.4, the temporal spectral transfers and fluxes may differ considerably for different forcing frequencies. Consider the first three rows of Figure 3.4, corresponding to the three lowest forcing frequencies. In those three cases the spectral flux for the forcing term demonstrates that energy and enstrophy are injected within a narrow band of frequencies surrounding the forcing frequency. The spectral fluxes for the wavenumber (inverse wavenumber) filters indicate enstrophy (energy) dissipation over wide ranges of high (low) frequencies. The spectral fluxes due to the dissipation terms are largely independent of the forcing frequency for these three cases. The spectral fluxes for the nonlinear term show that energy and enstrophy are removed within a narrow band near the forcing frequency and are injected at the dissipation frequencies. The sum of all the flux terms approximately equals zero, implying there is roughly no net energy injection into any of the frequency modes. Because the flux

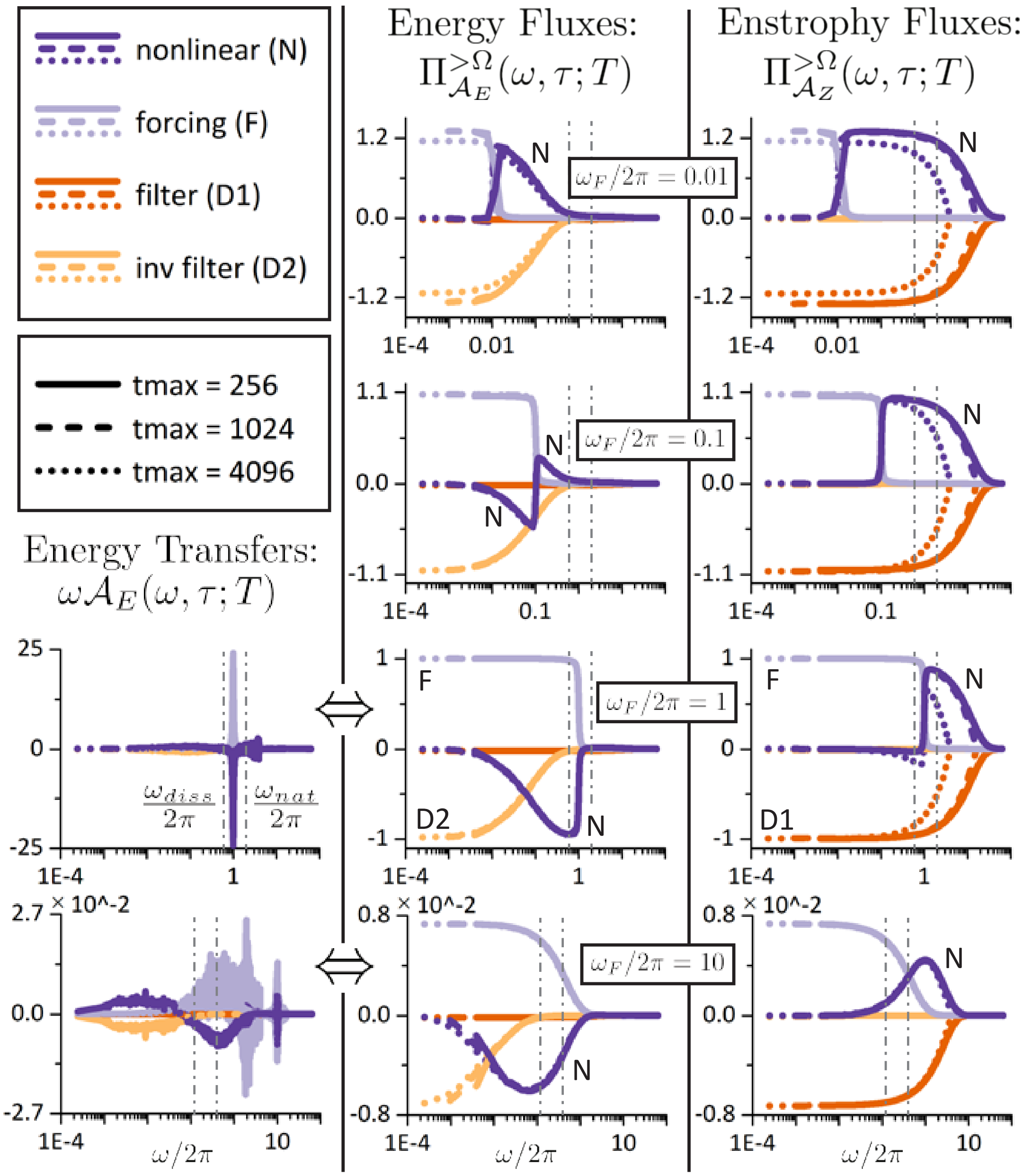

Figure 3.4: Temporal spectral fluxes. For each of the four forcing frequencies (rows) we plot temporal spectral *fluxes* of energy (middle column) and enstrophy (right column). For the two highest forcing frequencies, the temporal spectral *transfers* are shown as well (left column), corresponding to the spectral fluxes directly to their right. The upper legend defines each term in the spectral budget. The lower legend indicates values of t_{max} (and hence sampling rate). The two natural frequencies $\omega_{diss}/2\pi < \omega_{nat}/2\pi$ are indicated by gray vertical dash-dotted lines.

due to the forcing term depends strongly on the forcing frequency but the fluxes due to the dissipation terms do not, a wide range of behaviors for the fluxes due to the nonlinear term are possible: energy can be transferred to lower frequencies, higher frequencies, or both. However, enstrophy is always transferred to higher frequencies.

The lowest forcing frequency case ($\omega_F/2\pi = 0.01$) is particularly interesting, as it shows energy may be injected at very low frequencies and then transferred to higher dissipation frequencies (indicated by a positive flux). This may be related to the positive temporal energy flux calculated by *Arbic et al.* (2012, 2014) for one region of the ocean. In that one region, the time scale associated with energy injection by baroclinic instability is much longer than the eddy time scale, significantly more so than in the other regions considered. There may be other explanations, such as inadequate spatio-temporal resolution of the data, for the positive temporal energy flux observed in *Arbic et al.* (2012, 2014). However, we have shown here that a positive flux is actually possible when energy is injected at low frequencies.

Now consider the fourth row of Figure 3.4, corresponding to the highest forcing frequency ($\omega_F/2\pi = 10$). In that case the spectral flux of the forcing term demonstrates that energy and enstrophy are injected *not* at the forcing frequency but within a wide range of frequencies below the forcing frequency centered at $\omega/2\pi = 0.4$. The spectral fluxes for the wavenumber and inverse wavenumber filters indicate enstrophy and energy dissipation over wide ranges of frequencies that begin at lower frequency than was the case for the other three forcing frequencies. The spectral flux for the nonlinear term demonstrates energy and enstrophy removal from the injection frequency and deposition at relatively lower (for energy) or higher (for enstrophy) frequencies. The injection frequencies are lower than the forcing frequency. The total energy injected by the forcing is lower than the energy injection for the other three forcing frequencies by a factor of about a hundred. This lower injection rate should be expected when the fluid cannot respond to the forcing on short time scales.

While figure 3.4 shows the temporal spectral energy transfers in a noisy unedited form for the highest two forcing frequencies, in figure 3.5 we show cleaned up versions of the temporal spectral energy and enstrophy transfers for these two runs. In order to to make the transfers more presentable for figure 3.5 we choose not to utilize overlapping results from the three datasets with three different durations. Instead we use the longest duration dataset for the lowest frequencies, the shortest duration dataset for the highest frequencies, and the intermediate duration dataset for the intermediate frequencies (without any overlap). That choice removes all of the noise due to aliasing at the highest frequencies and also removes incorrectly calculated transfers at the lowest frequencies. In addition, for the $\omega_F/2\pi = 1$ case, we scaled the vertical axes to make the nonlinear transfer outside of the forcing range more visible. Figure 3.5 clearly shows that for both forcing frequencies there is a transfer of energy to lower frequencies and a transfer of enstrophy to higher frequencies relative to the forcing injection frequency. When the fluid is forced at the highest frequency ($\omega_F/2\pi = 10$) the injection of energy and enstrophy by the forcing occurs at frequencies lower than $\omega_F/2\pi$ centered near $\omega/2\pi = 0.4$.

Figure 3.6 shows the full spatio-temporal spectral transfers for all four forcing frequencies. The top plot combines the results for the three lowest forcing frequencies. The combination of these three cases in one plot is possible because the transfers due to dissipation remain largely unchanged while the transfers due to the forcing do not overlap. The transfers due to the nonlinear term are not shown, because they can be simply calculated based on the fact that the sum of all the transfers is zero everywhere in (k, ω)-space (the residual was effectively zero). Any of the fluxes or transfers shown in figure 3.4 or figure 3.5 can be obtained by integrating the spatio-temporal transfers shown in figure 3.6 over all k and (for the fluxes) partially over ω. One feature highlighted by the spatio-temporal spectral transfers is that energy (or enstrophy) is typically injected at the forcing frequency unless the forcing frequency

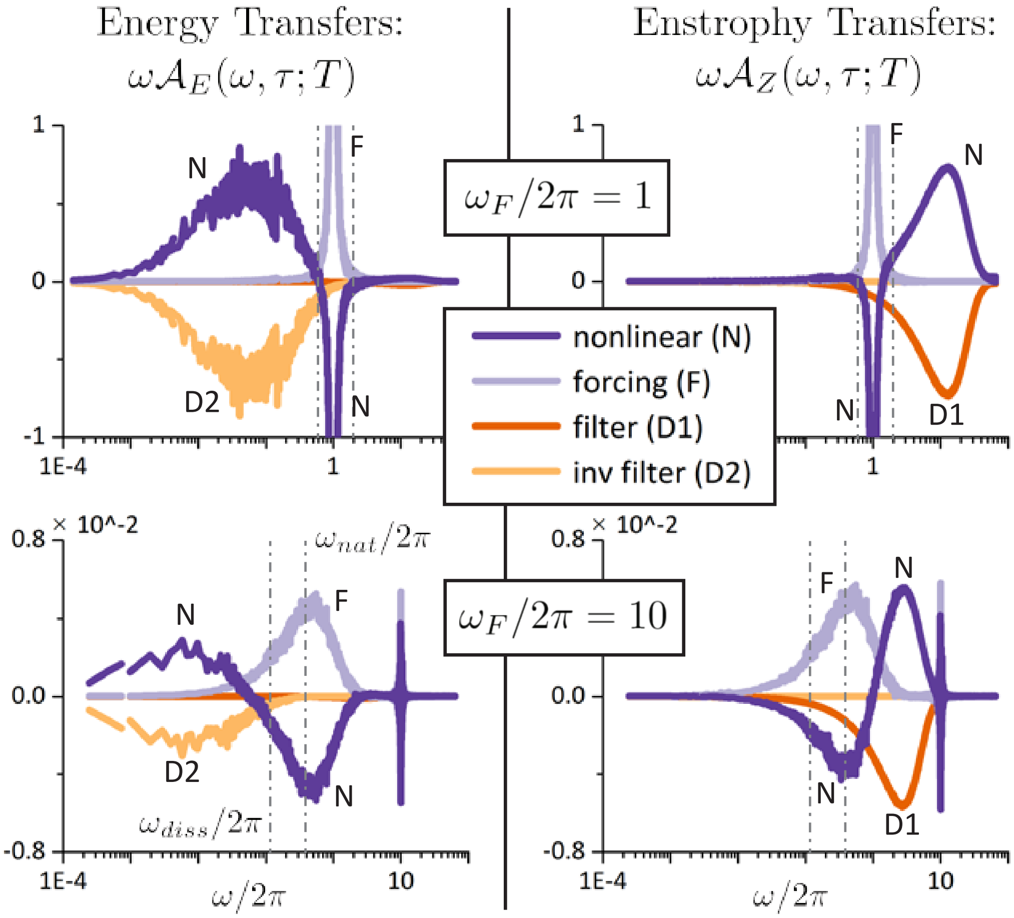

Figure 3.5: Temporal spectral transfers "$\omega\mathcal{A}(\omega,\tau;T)$ vs. $\omega/2\pi$" of energy (left) and enstrophy (right) for the simulations forced at the two highest forcing frequencies, $\omega_F/2\pi = 1$ and $\omega_F/2\pi = 10$, displayed in area-preserving format. The multiplicative factor of ω preserves the area under the transfers on the semi-log plot. Each plot is created using the same data as in figure 3.4. Unlike the transfers shown in figure 3.4, the noisiest regions of each dataset are removed. In bottom row, the transfers near $\omega/2\pi = 10$ are noisy, but they integrate to zero (the total transfer in that frequency range is negligible), which is made clear by the smoothness of the fluxes in that region as shown in figure 3.4. The two natural frequencies $\omega_{diss}/2\pi < \omega_{nat}/2\pi$ are indicated by gray vertical dash-dotted lines.

is too high. In the latter case significantly less energy (or enstrophy) is injected, and the injection takes place over a much wider range of lower frequencies. While the spatio-temporal transfers for this particular two-dimensional fluid are quite simple when viewed as in figure 3.6, we note that the usefulness of the transfers is in the *quantification* of the spatial- and time-scales involved in the injection of energy and enstrophy.

Lastly, figure 3.7 shows how the fluxes of energy and enstrophy change in time τ during spin-up beginning at rest and forced at either $\omega_F/2\pi = 1$ or $\omega_F/2\pi = 10$. This is somewhat of a test of our interpretation of the temporal spectral transfers, though perhaps the range of frequencies involved is too narrow to be conclusive. For the run forced at the lower frequency ($\omega_F/2\pi = 1$), energy and enstrophy are consistently injected at the forcing frequency. As the central time τ increases, energy is transferred to even lower frequencies while enstrophy is transferred to even higher frequencies, though the effect is somewhat small. For the $\omega_F/2\pi = 1$ simulation, the injection frequency range for both energy and enstrophy shifts to higher frequencies as time progresses. This shift of injection frequency to higher frequencies is likely due to the increase of the average velocity of the fluid. The dissipation ranges of energy and enstrophy also evolve over time, with the energy dissipation range moving to lower frequencies and the enstrophy dissipation range moving to higher frequencies. This evolution of the dissipation ranges corresponds to the development and widening of the spatial cascades of energy and enstrophy.

3.3.3 Effects of varying the window size and sampling rate

We calculated the temporal spectral transfers $\mathcal{A}(\boldsymbol{k}, \omega, \tau; T)$ for a wide range of window sizes T and for a wide range of sampling rates. The former tests the dependence of the temporal spectral transfers on a parameter inherent to the time-frequency method as discussed at the end of section 2.3.4, while the latter tests the dependence

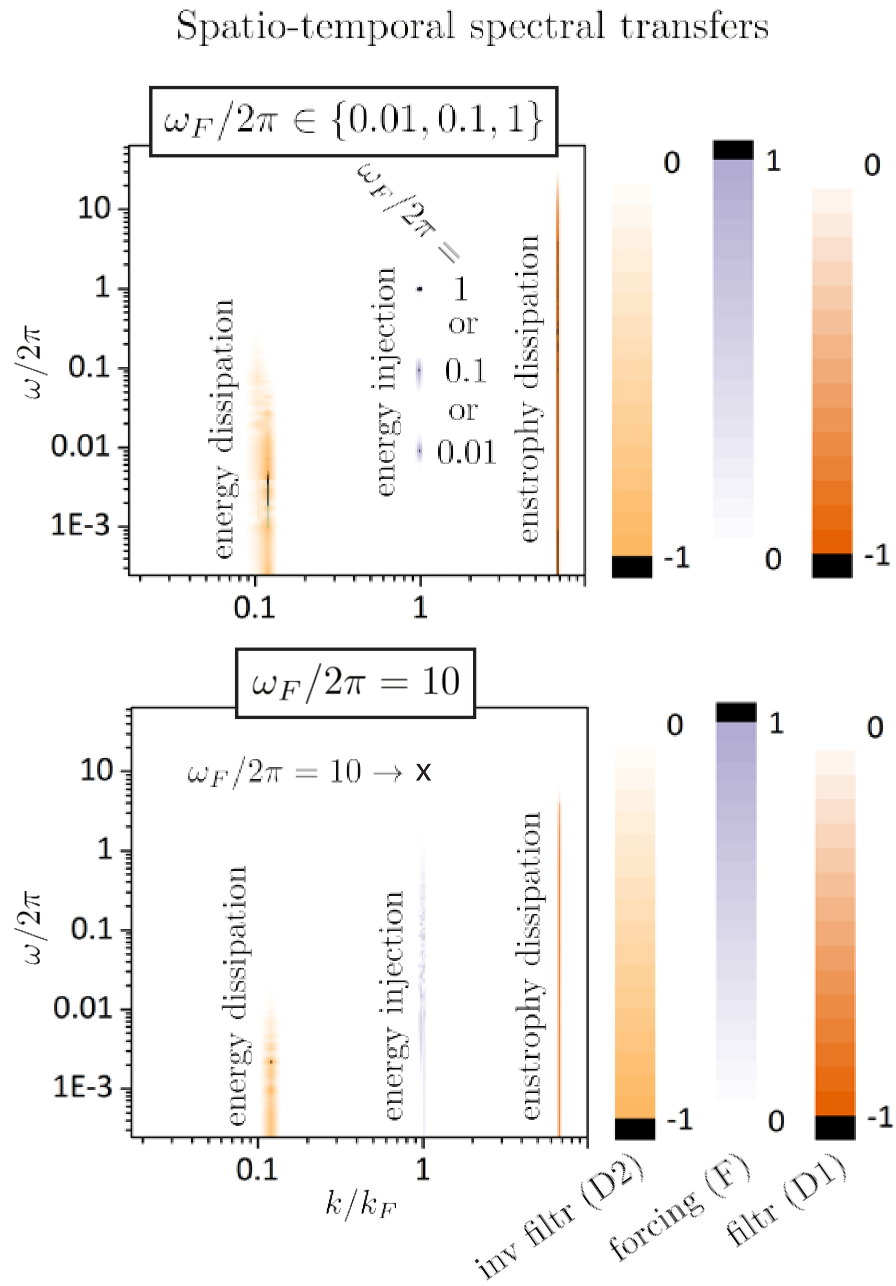

Figure 3.6: Spatio-temporal spectral transfers for the three lowest forcing frequencies (top) and the highest forcing frequency (bottom). We only show the forcing and dissipation terms, because the nonlinear term is approximately the negative of the sum of the other terms. Transfers of both energy and enstrophy are shown, because the dominant features do not overlap in (k, ω)-space, except at the forcing frequencies for which only energy transfers are shown. Because the dissipation terms are quantitatively similar for the three lowest forcing frequencies, the upper plot shows only the case $\omega_F/2\pi = 1$. The lower half of each plot is based on the longest dataset ($t_{max} = 4096$), while the upper half of each plot is based on the shortest dataset ($t_{max} = 256$). In the bottom plot, the symbol "x" marks the location of (k_F, ω_F), which is notably outside the range of frequencies in which energy is injected by the forcing.

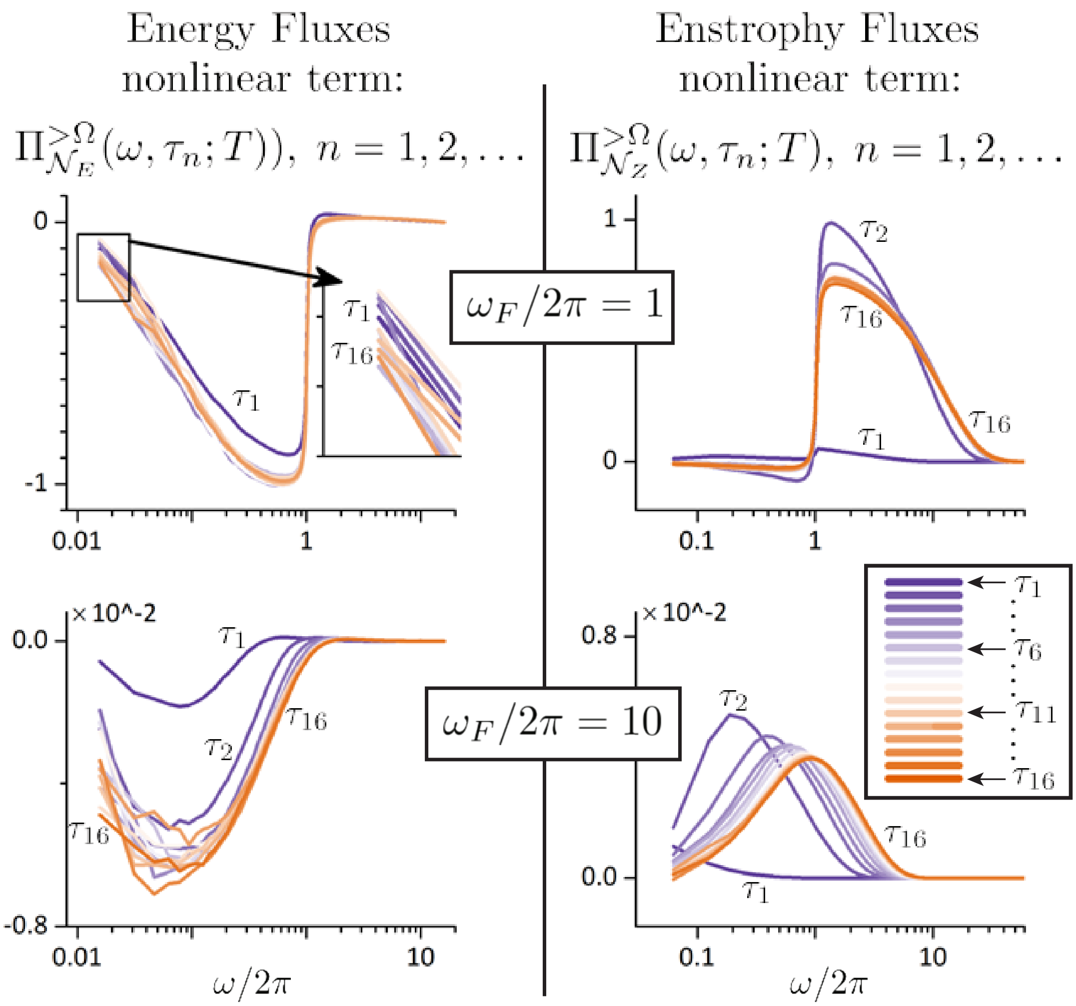

Energy Fluxes nonlinear term: $\Pi^{>\Omega}_{\mathcal{N}_E}(\omega, \tau_n; T)), \; n = 1, 2, \dots$

Enstrophy Fluxes nonlinear term: $\Pi^{>\Omega}_{\mathcal{N}_Z}(\omega, \tau_n; T), \; n = 1, 2, \dots$

Figure 3.7: Temporal spectral fluxes during spin-up. Temporal spectral fluxes “$\Pi^{>\Omega}_{\mathcal{N}}(\omega, \tau; T)$ vs. $\omega/2\pi$” of energy (left) and enstrophy (right) for sixteen values of the central time $\tau = \tau_1 < \tau_2 < \cdots < \tau_{16}$ corresponding to contiguous non-overlapping windows starting from the spin-up of a fluid beginning at rest. For the energy fluxes, we choose the duration of each window to be $T = 64$, while for the enstrophy fluxes we choose $T = 16$. We only show results for the simulations forced at the highest two frequencies, $\omega_F/2\pi = 1$ and $\omega_F/2\pi = 10$. In both cases one observes a change in the transfer of energy to lower frequencies, and of enstrophy to higher frequencies, as τ increases.

of the transfers on the limited temporal resolution of discrete datasets (an issue not discussed in Chapter II which assumed the datasets to be continuous in time).

In Figure 3.8 we show the temporal spectral transfers $\mathcal{A}(\boldsymbol{k}, \omega, \tau; T)$ for window sizes $T \in \{2^{12}, 2^{10}, 2^8, 2^6, 2^4\}$ and sampling rates chosen so that the total number of snapshots is always 512, purposely on the small end of what might be considered good number of samples in a realistic dataset. Results for both energy (upper plots) and enstrophy (lower plots) are shown. Each column corresponds to a single forcing frequency, with the leftmost column forced at the lowest frequency. In each column, the lowest dataset is sampled the least frequently while the highest dataset is sampled most frequently. Each y-axis shows the scale for the lower-leftmost plot on that axis. The remaining plots have been shifted vertically so that they do not all overlap with each other. Each column "leans" to the right, because the sampling rate increases from bottom to top while the number of samples remains constant. To save space, we overlapped the graphs for the four forcing frequencies, with the graphs for the lowest three forcing frequencies sharing the same vertical scale.

Because there is a lot of information in Figure 3.8, it helps to examine the figure systematically, one flux term at a time. Considering first the energy dissipation by the inverse wavenumber filter ("inv filter"), we see that the flux calculated at each resolved frequency remains roughly constant throughout all figures, demonstrating that even when the datasets are not long enough to capture all of the dynamics, the temporal spectral fluxes remain fairly accurate down to the lowest resolved frequencies. As for datasets that are too infrequently sampled, the temporal spectral fluxes become inaccurate only at the very highest resolved frequencies, due to aliasing of the unobserved higher-frequency modes into lower modes. Fluxes due to the dissipation of enstrophy by the wavenumber filter ("filter") exhibit similar behaviors, except that the aliasing effect at higher frequencies is more readily apparent. Despite the aliasing, the total transfer (given by the flux at the lowest resolved frequency)

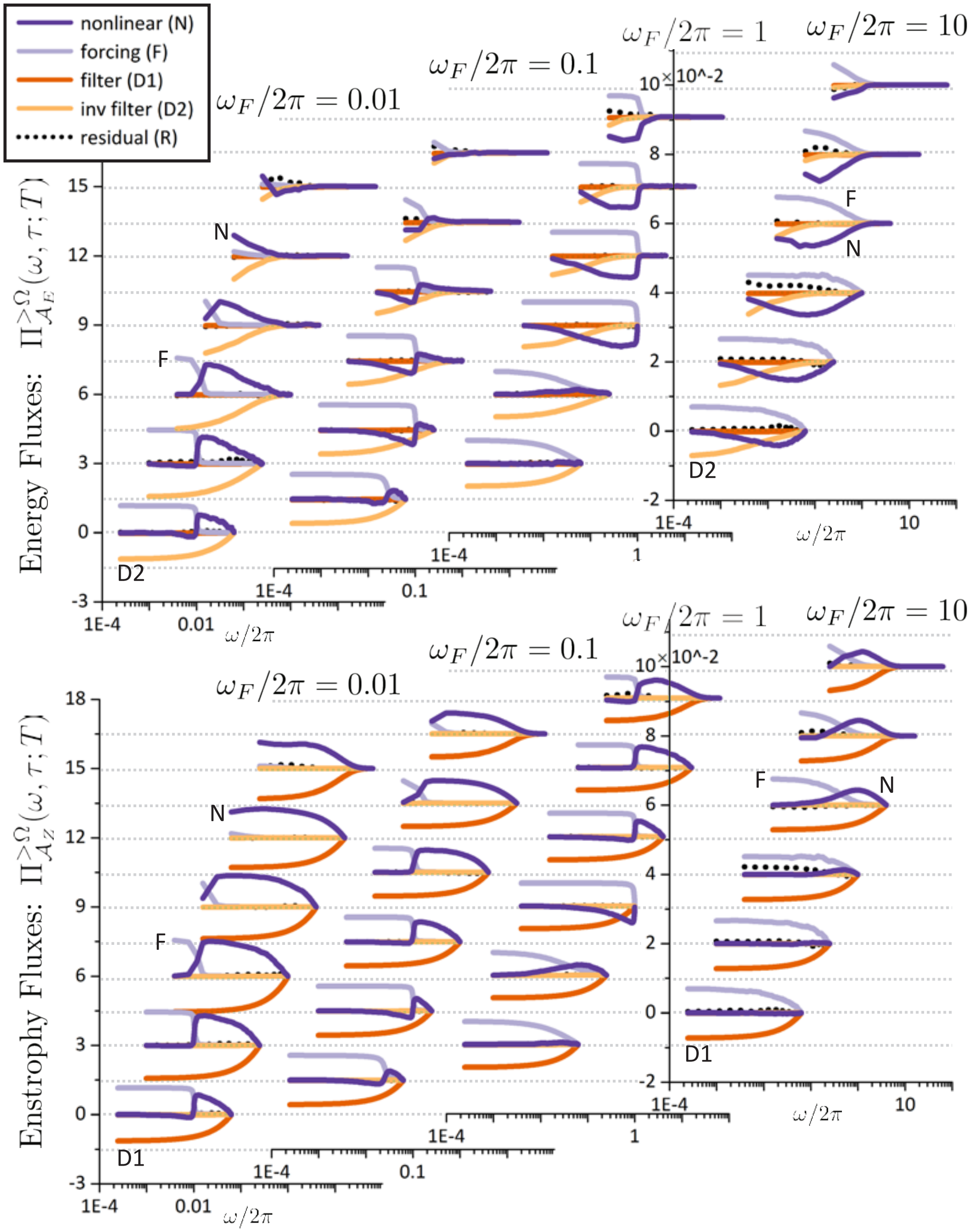

Figure 3.8: Effect of window size and sampling rate on temporal spectral fluxes. Temporal spectral fluxes of energy (top half) and enstrophy (bottom half) for the four forcing frequencies (columns) using datasets created by sampling at six different sampling rates (rows), while keeping the total number of samples in each dataset constant ($N = 512$). Each column corresponds to a single simulation. In each column, the bottom set of fluxes uses the least frequently sampled dataset while the top set of fluxes uses the most frequently sampled dataset. For each vertical axis, the lower-leftmost set of fluxes is plotted correctly centered at zero, while all other fluxes are plotted to-scale but shifted vertically.

remains roughly the same throughout the datasets, indicating that aliasing effects are localized to higher frequencies.

Turning to the forcing term ("forcing") for both energy and enstrophy, we see that the calculated fluxes are basically correct if and only if the forcing frequency is not too close to the edge of the interval of resolved frequencies. For example, when the forcing frequency is far too low to be resolved by a short dataset, or when the forcing frequency is far too high to by resolved by the sampling rate, the calculated flux is basically correct at each frequency (except for the very highest frequencies in the latter case, due to unavoidable aliasing in the highest frequencies). When the forcing frequency is near the edge of the interval of resolved frequencies, then the flux due to the forcing tends to flatten out, particularly as seen in the case for the energy flux when $\omega_F/2\pi = 1$ and $T = 2^{10}$ (second set of fluxes from the bottom). When the forcing frequency is just a bit lower than the smallest resolved frequency, as in the case $\omega_F/2\pi = 0.01$ and $T = 2^8$ (third from the bottom), one again sees the representative flattening of the flux.

Due to the effectively zero residual flux for all of the evaluated datasets, the effect of the window size and sampling rate on the temporal flux due to the nonlinear advection term ("nonlinear") is a combination of the effects on the forcing and dissipation terms. We note that the nonlinear flux term tends to have the correct sign and roughly the correct shape, *except* when the forcing frequency is barely *un*resolved by the sampling rate, as characterized by the energy fluxes when $\omega_F/2\pi = 1$ and $T = 2^{10}$ or by the enstrophy fluxes when $\omega_F/2\pi = 1$ and $T = 2^{10}$ or $T = 2^8$. Those cases give particularly inaccurate temporal spectral fluxes because neither the forcing frequency nor the enstrophy dissipation range are resolved by the sampling rate. These problematic cases may actually be representative of real world datasets (for large systems, like the ocean, where the shortest time scales are not resolved by data). However, the fluxes are inaccurate only at the highest resolved frequencies, while the fluxes at the remaining resolved frequencies seem to be reliable.

3.3.4 Effects of varying the detrending method

For most of our simulations we calculate temporal spectral transfers both with and without the use of a temporal detrending operation (specifically, the removal of a linear trend). In previous sections, we reported only on results that did not include a detrending operation. For datasets with sufficiently long duration (figures 3.4, 3.5 and 3.6), because the simulations are statistically stationary, the trends are effectively zero and the detrending operation has no effect on the spectral fluxes. For datasets with shorter durations (as in figure 3.8), the effect of the detrending on the temporal fluxes is only seen at the lowest two or three resolved frequencies.

To study the effect of the detrending operation on the lowest resolved frequencies, we specifically looked at datasets that had durations significantly shorter than the forcing period, with the intent of interpreting the forcing as an externally imposed trend. Figure 3.9 shows temporal spectral fluxes calculated without and with detrending for eight independent datasets of length $t_{max} = 16$ that were forced at the longest forcing period, $2\pi/\omega_F = 100$. For comparison, the "true" values of the temporal spectral fluxes, determined from a much longer dataset, are indicated by arrows. The temporal flux due to the forcing term is brought much closer to the true value of the flux through the act of detrending. The same result holds for the dissipation term as well. The flux due to the nonlinear term, on the other hand, was not consistently brought closer to the true value after applying a detrending operation. However, we note that the discrepancy between the true nonlinear flux and the calculated nonlinear flux in both the detrended and non-detrended cases is never very large. In summary, the detrended transfers are typically closer to the "true" transfers (except for the nonlinear term), but usually not by much and only at the very lowest frequencies.

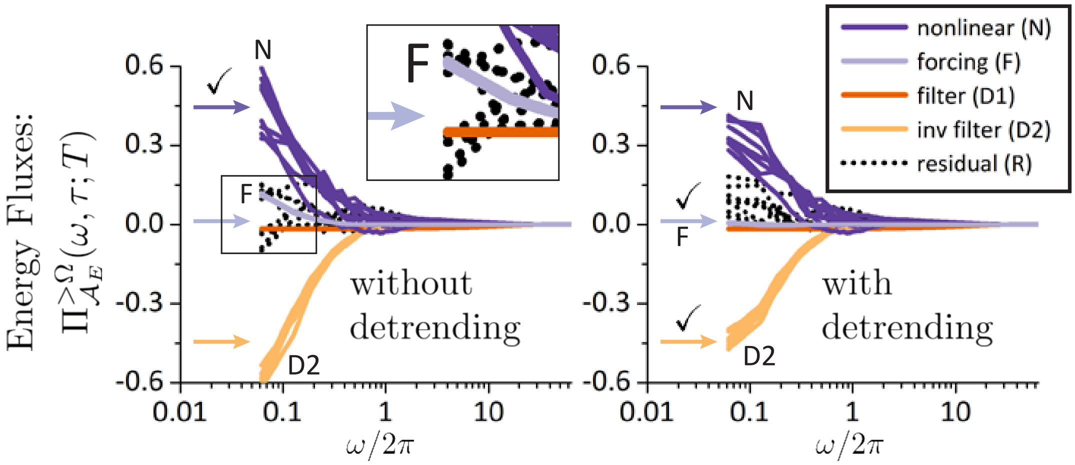

Figure 3.9: Effect of detrending on temporal spectral fluxes. Temporal spectral fluxes of energy calculated for eight independent datasets each of length $t_{max} = 16$ and forced at the lowest forcing frequency, $\omega_F/2\pi = 0.01$. The low-frequency forcing is the source of the trend. The resulting eight transfers are shown using the STFT *without* detrending (left) and *with* detrending (right). The arrows indicate the "true" values for the fluxes (at frequency $\omega = 2\pi/16$) obtained from a much longer data set with the same temporal resolution. Good matches with the correct fluxes are indicated by check marks (✓).

3.3.5 Evidence for the sweeping hypothesis in 2D turbulence

Recall that in Chapter II we predicted the effects of isotropic sweeping on the spatio-temporal spectral transfers. One of our predictions was that the spatio-temporal transfers $\mathcal{A}(k,\omega,\tau)$ should become ω-independent when k is large and ω sufficiently small (relative to a threshold that is dependent on the distribution of sweeping velocities). Indeed, as expected we see this effect in the enstrophy dissipation range but not in the energy dissipation range.

Figure 3.10 displays the spatio-temporal spectral transfers of energy and enstrophy due to the two dissipation terms. We show the transfers due to the dissipation terms, but we could have just as well shown the transfers due to the nonlinear advection term, since the total transfer adds to (effectively, although not numerically) zero at each (k,ω) pair. The results are shown for two of the four forcing frequencies, namely $\omega_F/2\pi = 1$ and $\omega_F/2\pi = 10$, with the former being representative of the other two runs. In each plot we show the line $\omega/2\pi = k\langle|\boldsymbol{u}|\rangle/2$. We see that at frequencies below approximately $\omega/2\pi = k\langle|\boldsymbol{u}|\rangle/2$ the spatio-temporal transfers of enstrophy become roughly ω-independent. Moreover, more than half of the total transfer occurs at frequencies below that rough cutoff. Note the changes in scale of the $\omega/2\pi$-axes between the upper and lower plots, indicating that the more energetic $\omega_F/2\pi = 1$ run has the widest range of frequency-independence, consistent with a higher sweeping velocity. Whether or not this is to be considered evidence for sweeping, it is at least perfectly consistent with the predictions made using the simple model for sweeping in section 2.3.2.

3.4 Conclusion

In this chapter, we provided illustrative examples of the theory presented in the previous chapter, through simulating homogeneous isotropic two-dimensional turbulence forced by a range of frequencies and diagnosing the resulting temporal and spatio-temporal spectral transfers. We examined the effects on the spectral transfers of varying the forcing frequency, varying the window size and sampling rate, and varying the detrending method. We also examined how temporal transfers of energy and enstrophy evolve in time in a forced fluid spun up from an initial at rest.

In completed, ongoing, and planned future work we have diagnosed (or will diagnose) spatio-temporal spectral transfers in complicated systems (e.g. ocean datasets and realistic-domain ocean models) that are not perfectly resolved by the available data. With that in mind, the main practical result of this Chapter is that the temporal and spatio-temporal spectral transfers and fluxes as calculated for finite datasets are quite robust to limitations typical of realistic data. Changes to window size, sampling rate, and detrending method usually have little effect on the temporal spectral transfers or fluxes except at marginal frequencies. For short duration datasets, temporal spectral fluxes tend to be accurate even when the lowest frequencies in the

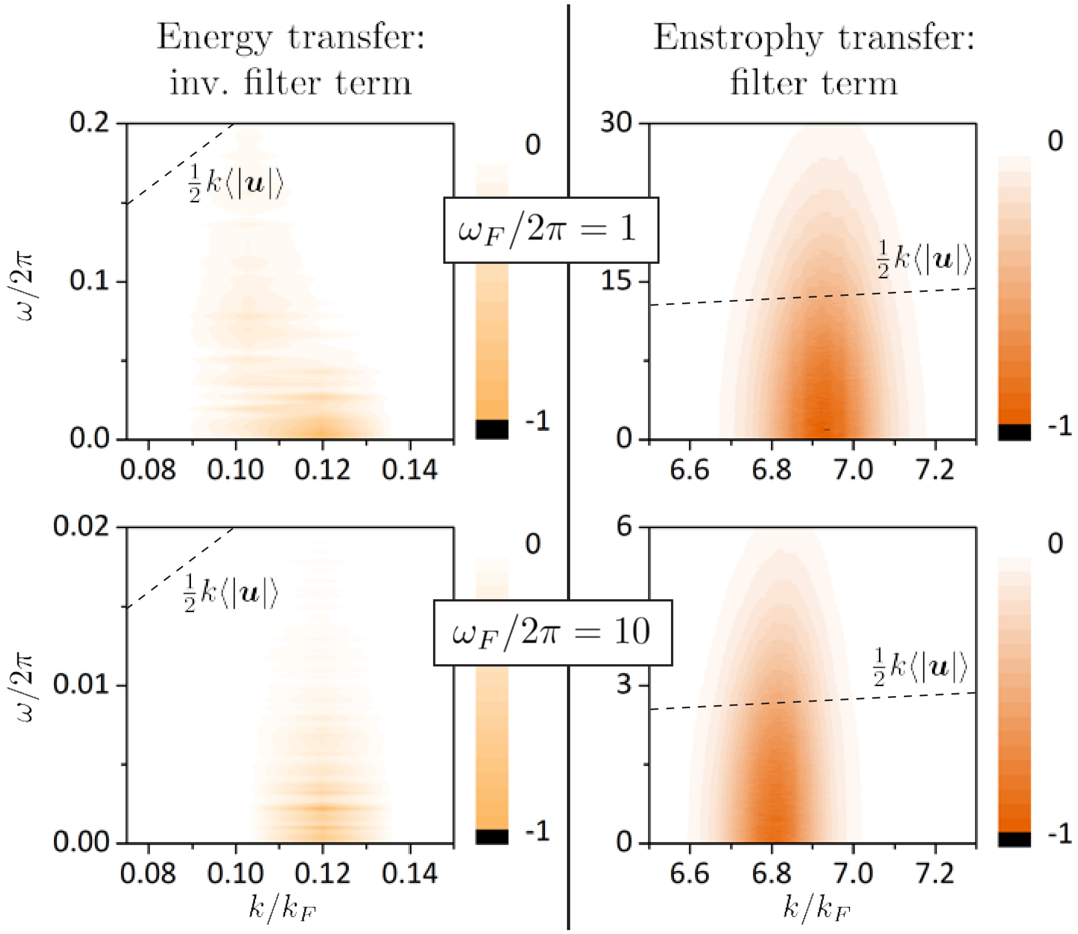

Figure 3.10: Effect of sweeping on spatio-temporal spectral transfers. Spatio-temporal spectral transfers of energy and enstrophy due to the dissipation terms for the runs forced at the highest two forcing frequencies. These are the same transfers as the dissipation terms shown in Figure 3.6, except that here the x- and y-axes use linear rather than log scales. If there is sweeping, then there should be frequency independence of the spatio-temporal spectral fluxes at sufficiently high wavenumber and low frequency. This effect is seen in the enstrophy dissipation range at frequencies below $k\langle|\boldsymbol{u}|\rangle/2$, where $\langle\cdot\rangle$ represents spatial or temporal averaging. Note the changes in scale of the $\omega/2\pi$-axes between the plots, indicating that the more energetic run ($\omega_F/2\pi = 1$) had the widest range of frequency-independence, consistent with the higher sweeping velocity. As expected, the effect of sweeping is not observed in the energy dissipation range, because k is not sufficiently large.

system are not resolved by the data. When the highest frequencies are not resolved, then there is aliasing into the highest resolved frequencies, but the temporal spectral fluxes at the remaining lower frequencies remain accurate. We found that one must be careful in the special case when the forcing frequency is close to (above or below) the highest resolved frequency, as the temporal spectral fluxes become particularly untrustworthy at nearby frequencies (but, importantly, only at nearby frequencies). In that case the worst effect (fluxes having the wrong sign) occurs only when the forcing frequency is slightly too high to be resolved and the dissipation range is also not resolved, a situation in which one should in any case be skeptical of the highest resolved frequencies.

We found that when the temporal window is narrow, a detrending operation may increase the accuracy of the temporal spectral transfers when the forcing frequency is unresolved, but the effect is small and only important at the few lowest resolved frequencies. Perhaps a study of detrended temporal spectral transfers would be better suited for a less idealized fluid than the one modeled here, which exhibits no long-term trend once statistical stationary states are reached.

Moving beyond testing of the diagnostic, a physical result found here is that while the spatial spectral transfers change little over a wide range of forcing frequencies, with energy cascading spatially upscale and enstrophy cascading spatially downscale, the temporal spectral transfers are quite sensitive to the forcing frequency, allowing both downscale and upscale temporal spectral transfers of energy, but only downscale transfers of enstrophy. This can be easily understood, as described in the following paragraph, in terms of the requirement that the sum of the spectral transfer terms be zero everywhere in (k, ω)-space for a statistically stationary flow.

The spatio-temporal spectral transfers due to the dissipation terms are largely unaffected by the forcing frequency as long as the forcing frequency is not too high. The spectral transfers due to the forcing term vary in (k, ω)-space according to the choice of the forcing frequency ω_F. Because the spectral transfers due to the nonlinear advection term must equal minus the sum of the other terms in a statistically stead state, the differences in nonlinear spectral transfers are explained entirely be the difference in the forcing spectral transfers. A physical explanation is that at forcing frequencies that are not too high the fluid allows energy and enstrophy to be injected and removed right at the forcing frequency, which may be incidentally lower or higher than the frequencies at which dissipation occurs. The resulting temporal spectral transfer of energy or enstrophy to the dissipation frequency scale may be partially or fully non-local, bypassing any need for a cascade through frequency space.

In the simulation with the highest forcing frequency, the fluid can not respond to the dominant time-scale of the forcing. Turbulence still develops but at a less energetic level, as was previously found in other studies of “modulated” turbulence in three-dimensions. Because the fluid cannot respond to arbitrarily high frequencies (without changing the forcing amplitude), there is an upper limit for the frequency at which enstrophy can be injected. If this limiting injection frequency is lower than the highest frequencies associated with the enstrophy dissipation range, then there cannot be a transfer of enstrophy to frequencies below the injection frequency. Thus, while energy can be transferred either upscale or downscale from the injection frequency, enstrophy probably can only be transferred downscale in two-dimensional turbulence (likewise for energy in three-dimensional turbulence).

CHAPTER IV

Wavenumber-frequency analysis: single-layer shallow water quasi-geostrophic equation

4.1 Outline

This chapter has three main parts: Numerical setup (section 4.2), Numerical results (section 4.3), and Summary of results (section 4.4). In the Numerical setup (section 4.2) we describe the single-layer shallow-water quasi-geostrophic model (on the beta plane) and discuss the possible ways to nondimensionalize the system. We settle on three nondimensional parameters constructed as ratios of various length scales in the system. Based on these three parameters, we design a parameter sweep that we argue is oceanographically relevant and that is quite comprehensive, consisting of a total of fifty-four distinct cases. This large number of cases spans a wide range of behaviors, including isotropic turbulence, westward propagating vortices, vortices co-existing with jets, meandering jets, and strong nearly zonal jets.

In the Numerical results (section 4.3) we investigate the wavenumber-frequency spectra and spectral transfers for this large collection of simulations. We have diagnosed zonal and meridional wavenumber-frequency spectra and spectral transfers for all of these runs. However for the sake of brevity we focus on the select few figures that demonstrate the phenomona of interest. The Summary of results (section 4.4) distills the many and varied lines of evidence in the Numerical results section into a more compact narrative.

4.2 Numerical Setup

The equation of motion for forced-dissipated single-layer shallow-water quasi-geostrophic turbulence is

$$\partial_t(\nabla^2 - k_d^2)\psi + J(\psi, \nabla^2\psi + \beta y) = (\nu_{-2}\nabla^{-2} + \nu_6\nabla^6)\nabla^2\psi + F. \tag{4.1}$$

As in the two-dimensional vorticity equation 2.7 studied in Chapters II and III, $\psi(\boldsymbol{x}, t) = \psi(x\widehat{\boldsymbol{x}} + y\widehat{\boldsymbol{y}}, t)$ is the stream function, $J(\cdot, \cdot)$ is the Jacobian, and F is an imposed external forcing. In contrast to equation 2.7, equation 4.1 contains a finite deformation radius $L_d \equiv 1/k_d$ and a non-zero meridional gradient β of the Coriolis parameter. Whereas in Chapter III we used wavenumber cutoff filters for dissipation at large and small scales, here we use smoother operators: low order hypoviscosity (∇^{-2}) with coefficient ν_{-2} and moderately low order hyperviscosity (∇^6) with coefficient ν_6. A future study could also include a linear drag term ($\nu_0\nabla^2\psi$) instead of or in addition to hypoviscosity.

We simulate equation 4.1 using a fully de-aliased pseudospectral method with third-order Adams–Bashforth time-stepping. The pseudospectral method is based on the spatial Fourier transform of equation 4.1, which is

$$\partial_t(k^2 + l^2 + k_d^2)\widetilde{\psi} = J(\widetilde{\psi, \nabla^2\psi + \beta y}) - (\nu_{-2}|\boldsymbol{k}|^{-2} + \nu_6|\boldsymbol{k}|^6)|\boldsymbol{k}|^2\widetilde{\psi} + \widetilde{F}, \tag{4.2}$$

assuming spatially periodic boundary conditions. For mathematical convenience, the the spatial period is set to $L = 2\pi$ in each direction, so the smallest non-zero zonal and meridional wavenumbers are $k = 1$ and $l = 1$. As is customary in oceanographic applications, in this chapter we define the zonal wavenumber $k := \widehat{\boldsymbol{x}} \cdot \boldsymbol{k}$ and the meridional wavenumber $l := \widehat{\boldsymbol{y}} \cdot \boldsymbol{k}$. This differs from the notation of the previous two chapters, in which k was the isotropic wavenumber $|\boldsymbol{k}|$. While this may seem confusing, we simply follow what is standard in the literature.

The forcing F is chosen to be statistically isotropic in space, narrowband in wavenumber, and effectively white noise in time (having a very short integral timescale). The forcing is defined in Chapter III (equation 3.2). We set the integral timescale $\tau_{F_0} = 0.1$, which is relatively short compared to the enstrophy containing timescales in all of our simulations. Unlike the forcing used in Chapter III, the forcing used here has no periodic modulation. The forcing is narrowband in wavenumber, having nonzero values only in the range $k_F - \Delta k_F < |\boldsymbol{k}| < k_F + \Delta k_F$, where $\Delta k_F = 2$. As part of our parameter sweep, four different forcing wavenumbers will be considered: $k_F \in \{6, 15, 30, 90\}$. The amplitude of the forcing is chosen such that the (expected value of the) spatial root mean square of the forcing is numerically equal to one.

The dissipation coefficients are set dynamically during spin-up and then set to fixed values after statistical equilibrium is reached. The coefficient of hypoviscosity is chosen such that on average one tenth of the total potential energy is in spatial modes $|\boldsymbol{k}| \leq 3$. The coefficient of hyperviscosity is chosen such that on average 1×10^{-10} of the total enstrophy is in spatial modes $|\boldsymbol{k}| \geq 2k_{Ny}/3 \approx 342$, where k_{Ny} is the Nyquist wavenumber. This choice ensures an effective de-aliasing of the nonlinear term via the 2/3 rule (*Canuto et al.*, 2007a,b), giving an error of order 10^{-10} while maximizing the use of the available spatial resolution.

In order to construct a parameter sweep for equation 4.2, we need to determine the important non-dimensional parameters. We do so by determining the important length scales in this system and then taking their ratios. Two obvious candidates are the deformation radius $L_d = 1/k_d$ and the forcing scale $2\pi/k_F$. In forced-dissipated simulations, two more length scales are set by the large-scale dissipation of potential energy and the small-scale dissipation of enstrophy. These dissipation scales may be defined by the wavenumber centroids of potential energy and enstrophy:

$$k_{PE} := \frac{\int\int d^2k|\boldsymbol{k}||\widetilde{\psi(\boldsymbol{k},t)}|^2}{\int\int d^2k|\widetilde{\psi(\boldsymbol{k},t)}|^2} \quad \text{and} \quad k_Z := \frac{\int\int d^2k|\boldsymbol{k}||\boldsymbol{k}|^4|\widetilde{\psi(\boldsymbol{k},t)}|^2}{\int\int d^2k|\boldsymbol{k}|^4|\widetilde{\psi(\boldsymbol{k},t)}|^2}. \tag{4.3}$$

Our use of dynamic hypoviscosity ensures that a certain fixed fraction of potential energy is at the smallest wavenumbers, which in turn sets a fairly uniform value of k_{PE} for all of our equilibrated runs. Generally, $4 < k_{PE} < 5$ in every simulation that has reached statistical equilibrium.

Several recent studies (*Sukoriansky et al.*, 2007, 2008; *Galperin et al.*, 2010) have argued for the importance of the large-scale dissipation scale when the deformation radius is infinite (they do not consider the finite case). We follow their lead by letting k_{PE} be one of our chosen length scales. We select also the deformation radius and the forcing wavenumber, which gives a total thus far of two nondimensional parameters:

$$\gamma_d := \frac{k_d}{k_{PE}} \quad \text{and} \quad \gamma_F := \frac{k_F}{k_d}. \tag{4.4}$$

Based on the measurements of eddy size in the North Atlantic by *Eden* (2007), we chose three values of deformation radius $L_d \equiv k_d^{-1}$ that span the observed values of the ratio k_d/k_{PE}. Given that $k_{PE} \approx 4.5$ in equilibrated simulations, we choose $k_d \in \{6, 15, 30\}$, so approximately $\gamma_d = k_d/k_{PE} \in \{1.3, 3, 6\}$. The middle value of γ_d is the most common in the North Atlantic and the outer values lie near the extrema of the observations. In order to mimic baroclinic instability we try several $k_F \in \{6, 15, 30, 90\}$ restricted by requiring $\gamma_F = k_F/k_d \geq 1$.

There may be an additional length scale associated with the choice of β, which may govern the transition to jets. There are several contenders in the literature.

There is the Rhines wavenumber (*Rhines*, 1975)

$$k_{Rh} := \sqrt{\beta/2U_{rms}}, \tag{4.5}$$

where U_{rms} is the root mean square velocity of the fluid. However, the derivation of the Rhines scale does not take into account a finite deformation radius, so its applicability to our simulations is questionable. Taking into account a finite deformation, one can derive a modified Rhines wavenumber (*Okuno and Masuda*, 2003):

$$k'_{Rh} := \sqrt{k_{Rh}^2 - k_d^2}, \tag{4.6}$$

which is sometimes purely imaginary, in which case the beta-effect is small relative to nonlinearity. This "inhibition of the beta-effect" by a finite deformation radius (and hence inhibition of jets) has been useful in explaining the positions of stormy regions on Jupiter (*Theiss*, 2006) and Saturn (*Penny et al.*, 2010).

An alternative to the Rhines wavenumber (and its modification) is the transitional wavenumber (*Vallis and Maltrud*, 1993),

$$k_\beta := (\beta^3/\mathcal{C}^{3/2}\epsilon)^{1/5}, \tag{4.7}$$

where ϵ is the mean energy injection rate by the forcing, and by assumption $k_d = 0$. Equation 4.7 is derived by equating the Rossby wave period with the eddy turnover time, where the eddy turnover time is calculated based on an assumed form of the wavenumber spectra $E(k)$ (in this case assumed to follow Kolmogorov scaling $E(k) = \mathcal{C}\epsilon^{2/3}k^{-5/3}$). If we allow for a finite deformation radius, we obtain a modified transitional wavenumber k'_β defined implicitly by

$$k'_\beta := \text{largest } k \text{ that solves } \; a \cdot (k/k_d) = (k/k_d)^6 + 1, \tag{4.8}$$

where $a = \beta/(\mathcal{C}^{1/2}\epsilon^{1/3}k_d^{5/3})$, as is shown in *Smith* (2004). When equation 4.8 has no solution, then there is expected to be no anisotropy.

It is not clear from the literature which of these length scales is the most useful. Additionally, they all depend on a *post priori* quantity such as U_{rms} or ϵ, so their values cannot be directly chosen beforehand. Thus, we simply vary β over a wide range and report the resulting values of k_{Rh} and k'_{Rh} in Appendix A. We also report in Appendix A the related nondimensional parameters $\gamma_{Rh} := k_{Rh}/k_{PE}$ and $\gamma'_{Rh} := k'_{Rh}/k_{PE}$, as well as the dimensional values of U_{rms} used in their calculation.

At mid-latitudes in Earth's ocean, $\beta \approx 2 \times 10^{-11}$ m^{-1}s^{-1} (e.g. *Vallis*, 2006), $L_d \approx 3$–5×10^4 m (*Chelton et al.*, 1998), and $U_{rms} \approx 10$–100 cm s^{-1} (*Stammer*, 1997). Therefore, the Rhines wavenumber lies within the range $k_{Rh} \approx 3$–10×10^{-6} m^{-1}. Given the range of values for L_d, we get the nondimensional ratio $k_{Rh}/k_d \approx 0.1$–0.5, which can be compared to the same ratio in our simulations. In Appendix A we report both k_{Rh} and k_d as well the ratio $\gamma_{Rh} := k_d/k_{PE}$. Because $k_d/k_{PE} \approx 1$–7 in the ocean, this gives $\gamma_{Rh} \approx 0.1$–3. We do not argue whether k_{Rh}/k_d or k_{Rh}/k_{PE} is more relevant for comparison with the ocean. Our simulations give ratio values which more than span the oceanic regime. Simulations that lie outside the oceanic regime by either measure, due to large β and the formation of nearly zonal jets, may be more appropriate for comparison with the atmospheres of Jupiter or Saturn.

In summary, we conduct the following parameter sweep. Based on the measurements by *Eden* (2007) we choose $k_d \in \{6, 15, 30\}$, which approximately corresponds to $\gamma_d \in \{1.3, 3, 7\}$. We select $k_F \in \{6, 15, 30, 90\}$, but consider only forcing at scales equal to or smaller than the deformation radius (i.e. $k_F/k_d \geq 1$). For example, when $k_d = 6$ we conduct simulations for each $k_F \in \{6, 15, 30, 90\}$, but when $k_d = 30$ we only consider $k_F \in \{30, 90\}$. As discussed above, because the remaining nondimensional parameter is determined *post priori*, we simply vary β over a wide range. We conduct simulations for all $\beta \in \{0, 0.1, 1, 10, 100, 1000\}$, yielding a wide range of flow regimes.

4.3 Numerical Results

In this section we primarily focus on wavenumber-frequency spectra, with a limited focus on wavenumber-frequency spectral transfers. We display kinetic energy spectra,

$$E(k,l,\omega) := (k^2+l^2)|\widehat{\widehat{\psi}}(k,l,\omega)|^2, \tag{4.9}$$

and note that the same general features are seen in spectra of potential energy and enstrophy. We show zonal wavenumber-frequency spectra,

$$E(k,\omega) := \sum_l E(k,l,\omega), \tag{4.10}$$

meridional wavenumber-frequency spectra,

$$E(l,\omega) := \sum_k E(k,l,\omega), \tag{4.11}$$

and various slices of $E(k,l,\omega)$ at constant l or k. Note that $E(k,\omega)$ and $E(l,\omega)$ are two completely different functions, whose meanings are made clear by context and by their use of different inputs.

The nonlinear spectral transfers are

$$T(k,l,\omega) := \mathrm{Re}[\widehat{\widehat{\psi}}(k,l,\omega)^* \widehat{\widehat{J(\psi,\nabla^2\psi)}}], \tag{4.12}$$

where the "hat" operator is a detrended, windowed, discrete Fourier transform, and a^* indicates the complex conjugate of a. Zonal and meridional wavenumber-frequency spectral transfers, $T(k,\omega)$ and $T(l,\omega)$, are defined by summing over either all l or all k.

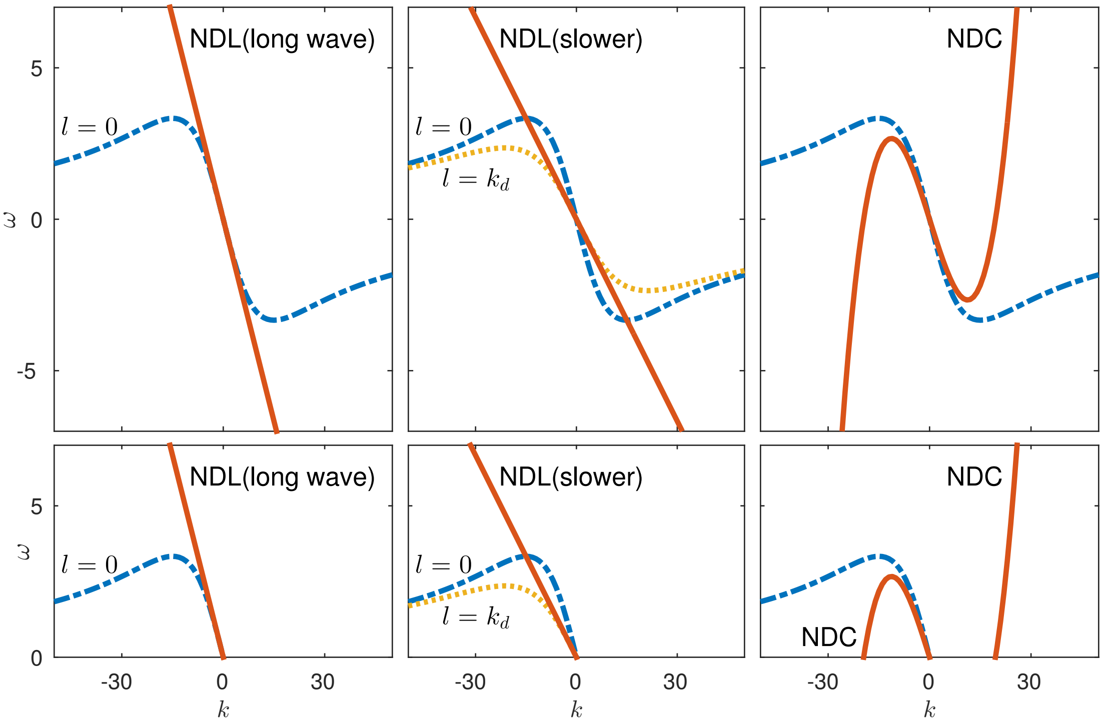

Figure 4.1: A schematic of the linear Rossby dispersion relation, the nondispersive line (NDL), and the nonlinear dispersive curve (NDC). The top row displays both positive and negative frequencies and zonal wavenumbers, thus clarifying the form of the NDC. The bottom row shows only positive frequencies, as do all other plots of $k\omega$-spectra in this chapter. When plotted as in the bottom row, the NDC appears as two disjoint sections. The dash-dotted curves show the $l = 0$ Rossby dispersion relation, while the dotted curves show the $l = k_d$ Rossby dispersion relation. The slope of the NDL indicates the uniform propagation speed. The "long-wave" NDL corresponds to the Rossby wave speed when $(k, l) = (0, 0)$. The "slower" NDL corresponds to the Rossby wave speed when $(k, l) = (0, k_d)$.

4.3.1 A schematic of observed phenomena

Figure 4.1 is a schematic of the various phenomena we observe in zonal wavenumber-frequency spectra. Real spectra (such as in Figure 4.2) are noisy and display scatter in the $k\omega$-plane, while Figure 4.2 displays simple curves that can be thought of as representing local maxima of idealized two-dimensional spectra. The top three panels show schematics of $k\omega$-spectra for both positive and negative values of k and ω. However, because of the symmetry $E(k, \omega) = E(-k, -\omega)$, it is redundant to show all wavenumbers and frequencies. Removing the redundancy, the bottom three panels show the same schematics limited to just the upper half-plane ($\omega \geq 0$). It is instructive to show the spectra both ways in figure 4.1 in order to emphasize the fact that the nonlinear dispersive curve (NDC) is one continuous curve. The NDC appears as two disjoint curves when $k\omega$-spectra are viewed in the upper half-plane. All other plots of $k\omega$-spectra in this chapter show only the upper half-plane. In like manner, all plots of $l\omega$-spectra in this chapter show only the upper right quadrant, due to an additional symmetry in the equation of motion.

For equation 4.1 the linear dispersion relation, otherwise known as the Rossby dispersion relation, is

$$\omega = \frac{-\beta k}{k^2 + l^2 + k_d^2}. \tag{4.13}$$

The phase speed is

$$\frac{\omega}{k} = \frac{-\beta}{k^2 + l^2 + k_d^2}, \tag{4.14}$$

such that the long-wave Rossby speed is $-\beta/k_d^2$, obtained in the limit $|\boldsymbol{k}| \to 0$.

In contrast to Rossby waves, which are dispersive, a uniformly zonally propagating feature will show up as a straight line in $k\omega$-spectra. The slope of such a line is the zonal propagation speed (negative for westward propagation). We often see such a line in spectra and refer to it as a "non-dispersive line" (NDL). The left panels of figure 4.1 show a NDL corresponding to the long-wave Rossby speed when $l = 0$. The middle panels show a NDL corresponding to a slower speed (the Rossby phase speed with $(k, l) = (0, k_d)$).

Aside from Rossby waves and uniform propagation, we sometimes will see another feature in $k\omega$-spectra which we refer to as a “non-dispersive curve” (NDC). The right panels of figure 4.1 show a prototypical NDC. At the time of writing, because we have no theoretical prediction for this curve, we have simply plotted a third degree polynomial that approximates the form of the NDC.

With reference to figure 4.1 we can easily summarize the main features of our $k\omega$-space investigations. At moderate values of β, we observe a NDL with slope approximately equal to the long-wave Rossby speed. At β large enough to produce jets we also observe a NDL, but sometimes with a slower velocity. At these values of β we also sometimes observe a NDC, or both a NDC and a NDL. At very high β, we observe the linear Rossby dispersion relation.

4.3.2 The importance of statistical equilibrium

A few of the simulations presented in this chapter are not as yet fully equilibrated. In particular, all of the runs with $\beta = 1000$ and some of the runs with $\beta = 100$ are still ongoing. Equation 4.1 is notorious for long equilibration times. The beta effect increases the equilibration time because the inverse cascade must proceed anisotropically, an inefficient and slow process. The finite deformation radius implies that the inverse cascade to large scales is dominated by a cascade of potential energy, which, dimensional arguments show, slows down the cascade further.

Fortunately, we have strong evidence for the unimportance of equilibration to the various features observed in the spectra. When a run is slow to equilibrate, it is because the potential energy takes a very long time to reach the large-scale dissipation range. However, kinetic energy and enstrophy reach equilibrated values much sooner. Despite a very slow cascade of k_{PE} to smaller wavenumber, features (such as a NDL or NDC) observed in kinetic energy $k\omega$-spectra remain unchanged, beginning from very early stages of the spin-up from rest.

As a typical example of the unimportance of equilibration on the form of the spectra, consider the case $(k_d, k_F, \beta) = (15, 90, 100)$, which exhibits a strong NDC and NDL. The potential energy is nearly equilibrated after two months (computational time) of spin-up, but the form of the spectra has not changed since day two, although the magnitude has changed. In that time the potential energy has increased by a factor of 100, but the enstrophy only increased by a factor of two, and the form of the NDC and the NDL has barely changed at all. Including this example, all of our unequilibrated simulations have spun up more than a factor of ten times longer than what was needed for the spectral features to stabilize.

4.3.3 Zonal wavenumber-frequency spectra

Figures 4.2–4.8 show $k\omega$-spectra of kinetic energy, and snapshots of vorticity $\nabla^2\psi$ for a wide range of runs. Each figure corresponds to a choice of k_d and k_F, and shows results for all six values of $\beta \in \{0, 0.1, 1, 10, 100, 1000\}$. Table 4.1 gives the values of the parameters k_d and k_F, for the runs shown in figures 4.2–4.8. For each of the three values of $k_d \in \{6, 15, 30\}$ we show results for $k_F = k_d$ (deformation radius scale forcing) and $k_F = 90$ (small-scale forcing). Because we wish to show one run with intermediate scale forcing, and because the $k_d = 15$ case is the most oceanographically relevant, when $k_d = 15$ we also show results for $k_F = 30$ (intermediate-scale forcing).

Figures (4.x)	$k_d \equiv 1/L_d$	k_F
2, 3	6	6, 90
4, 5, 6	15	15, 30, 90
7, 8	30	30, 90

Table 4.1: Parameter choices k_d and k_F for the simulations shown in figures 1–7.

To begin, figure 4.2 shows the case $(k_d, k_F) = (6, 6)$, which has the largest deformation radius and the largest scale forcing in the simulations shown in this chapter.

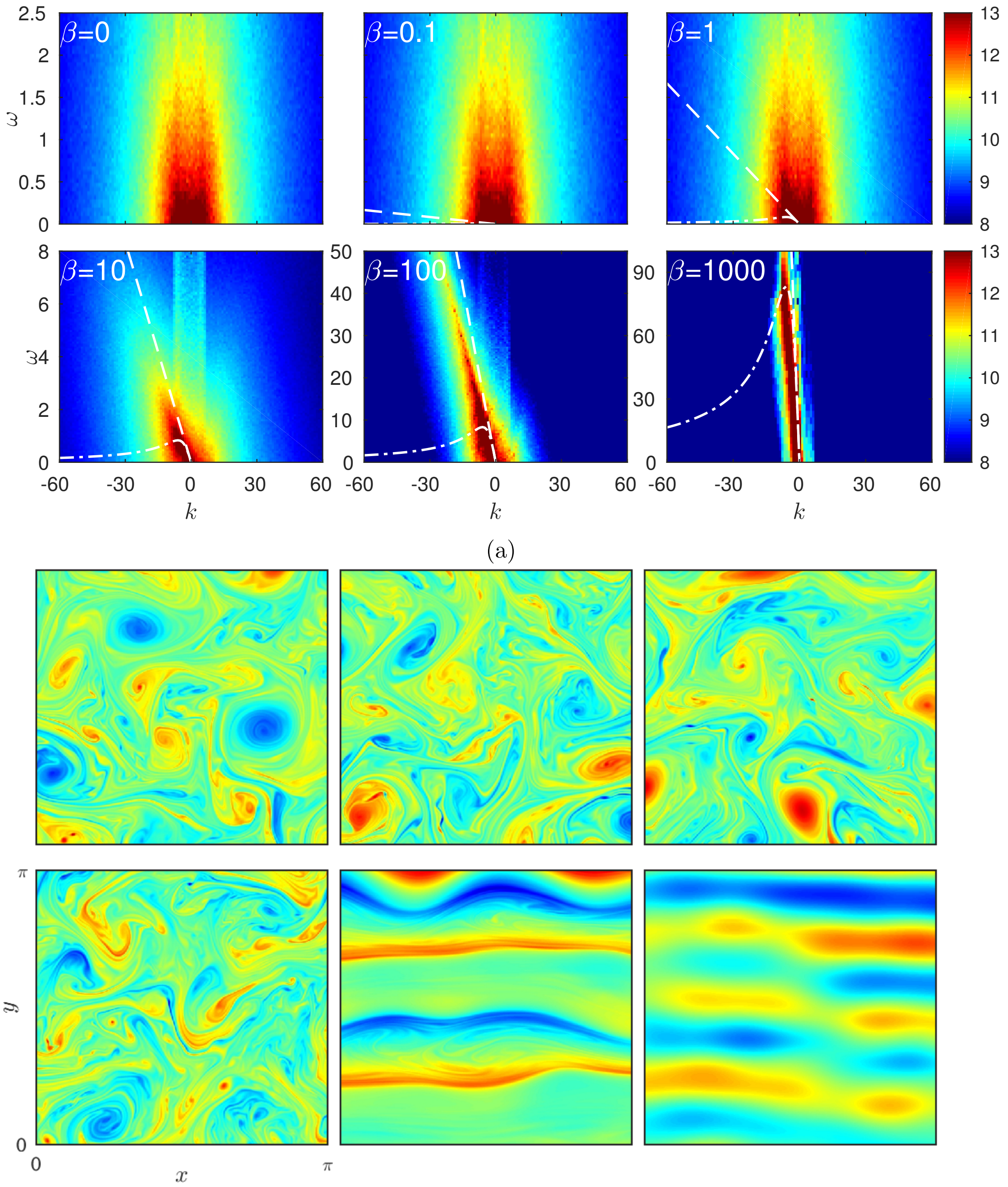

(a)

(b)

Figure 4.2: Zonal wavenumber-frequency spectra and vorticity snapshots for simulations with $(k_d, k_F) = (6, 6)$ and six values of β. The beta values are given in the upper plots. The lower plots are organized such that the β values correspond to those in the upper plots. (a) Kinetic energy spectra, $\log_{10} E(k, \omega)$. Dashed lines denote propagation at the long-wave Rossby speed. Dash-dotted curves show the $(l = 0)$ Rossby dispersion relation. The observed NDLs correspond to speeds slower than the long-wave Rossby speed. (b) The corresponding snapshots of vorticity.

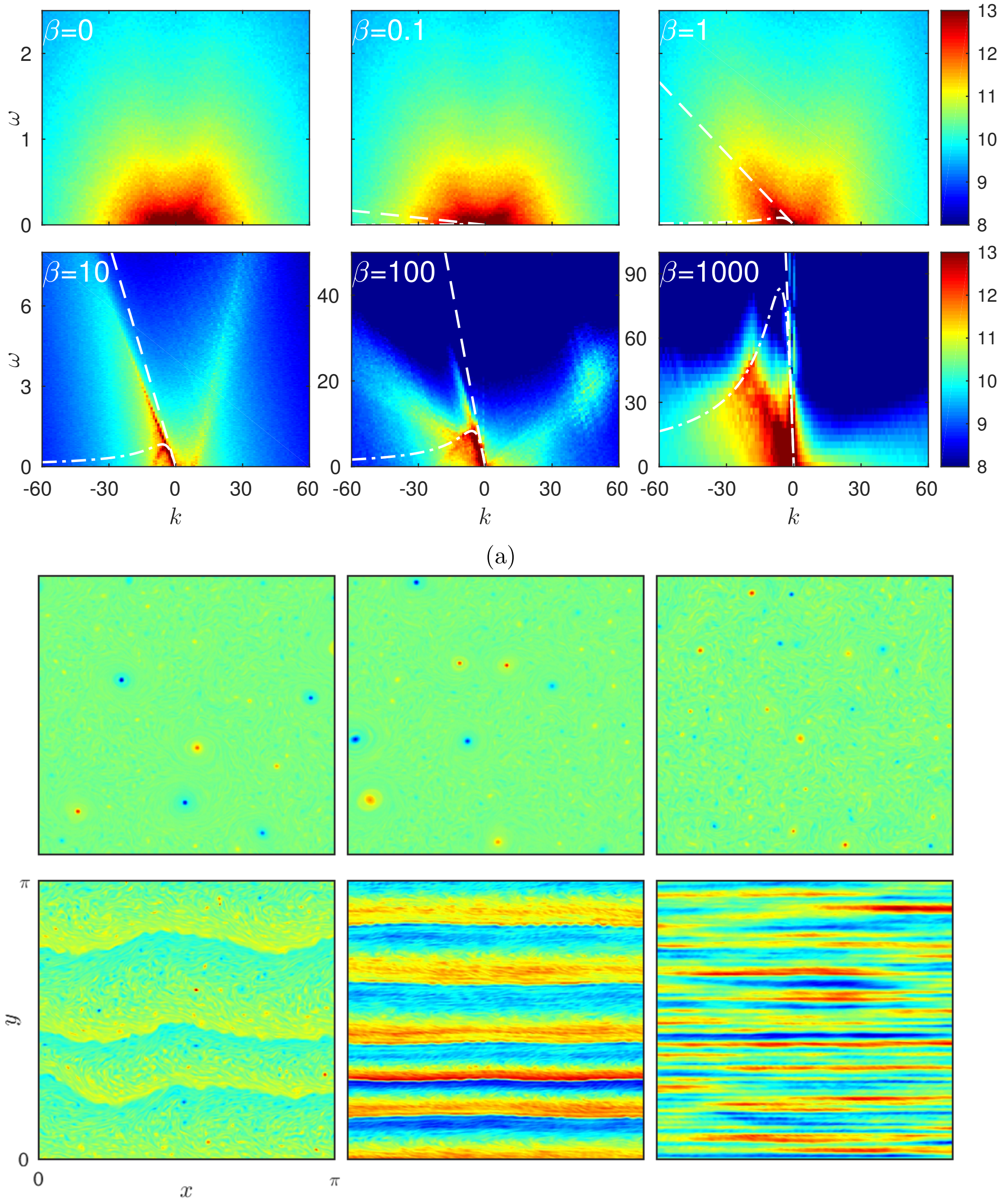

(a)

(b)

Figure 4.3: As in figure 4.2 but for simulations with $(k_d, k_F) = (6, 90)$. (a) Kinetic energy spectra, $\log_{10} E(k, \omega)$. Dashed and dash-dotted lines are as in figure 4.2. The observed NDLs correspond to speeds slower than the long-wave Rossby speed. There are prominent NDCs when $\beta = 10$ and $\beta = 100$. (b) The corresponding snapshots of vorticity. The $\beta = 10$ case corresponds to meandering jets co-existing with coherent vortices.

Judging from the $k\omega$-spectra, for the smallest three values of β there is not much sensitivity to β in the system. All of the corresponding vorticity snapshots exhibit coherent vortices. The size of the vortices reaches the deformation radius, which we note again is at the same scale as the forcing. When $\beta = 10$, the $k\omega$-spectra exhibits a wide NDL, indicating a tendency for uniform westward propagation. The westward propagation speed appears to be somewhat slower than the long-wave Rossby speed (indicated by a dashed line in each plot), but the discrepancy is not conclusive due to the great width of the NDL. The snapshot of vorticity in the $\beta = 10$ case shows weaker coherent vortices. The $\beta = 100$ case has no vortices and is instead dominated by jets. The $k\omega$-spectra in this case shows a much narrower NDL, indicating uniform westward propagation at a speed that is clearly slower than the long-wave Rossby speed. When $\beta = 1000$ there appears to still be a NDL, but it mostly coincides with the linear Rossby dispersion relation at low k and does not extend much into larger k. In order to distinguish a NDL from Rossby waves in this and similar cases, we must also consider $l\omega$-spectra or various slices of $E(k, l, \omega)$.

Next, figure 4.3 shows the case $(k_d, k_F) = (6, 90)$, i.e. the case employing the largest deformation radius and the smallest scale forcing of the values used in this chapter. The snapshots of vorticity indicate that the system is quite different from the previous case. Here the size of the coherent vortices does not exceed the forcing scale, which is much smaller than the deformation radius. In the $(k_d, k_F) = (6, 90)$ case, when $\beta = 1$ we get a hint of uniform westward propagation at roughly the long-wave Rossby speed. Indeed, in animations of vorticity snapshots one sees westward propagation of the coherent vortices. The $\beta = 10$ case is the first example thus far of a NDC in addition to a NDL. The NDL indicates uniform propagation at a speed slower than the long-wave Rossby speed. The NDC is clearly visible at both negative and positive k, indicating both westward and eastward phase speeds. For the NDC, at high k the phase speed appears to be independent of k (i.e. is linear), but the phase velocity does not equal the group velocity since the line does not pass through the origin. The vorticity snapshot shows coherent structures co-existing with meandering (i.e. non-zonal) jets. When $\beta = 100$, the coherent vortices are gone, and again we observe both a “slow” NDL and a NDC. When $\beta = 1000$ it appears that the $(l = 0)$ Rossby dispersion relation acts as a boundary of the spectra, consistent with the possibility that the spectra consists of Rossby waves for all l-values. We investigate whether these are Rossby waves later in this chapter.

Figures 4.4–4.6 show $k\omega$-spectra for $(k_d, k_F) = (15, 15)$, $(15, 30)$, and $(15, 90)$, arguably the most relevant cases for the ocean. We summarize the main points of these figures below. First, the size of the coherent vortices decrease along with the forcing scale. Second, the NDL appears in runs with only vortices (no jets) and in runs with only jets (no vortices), but the slope of the NDL appears to differ in the two cases. When there are no jets, the NDL indicates propagation at or near the long-wave Rossby speed, but when there are jets the uniform westward propagation appears to be slower. Third, while we observe NDLs regardless of the forcing scale, we only observe NDCs when the forcing scale is smaller than the deformation radius. When the forcing scale is large ($k_F = 15$), we observe no NDC. When the forcing scale is intermediate ($k_F = 30$) we see a hints of NDCs when $\beta = 10$ and 100. When the forcing scale is small ($k_F = 90$) we see clear NDCs for both of those values of β. Fourth, all of the cases that exhibit a NDC also exhibit meandering (i.e. non-zonal) jets. Fifth, when β takes its largest value, the jets become nearly purely zonal, the NDC disappears, and the linear Rossby dispersion relation appears to become important.

Figures 4.7–4.8 show $k\omega$-spectra for the smallest deformation radius cases, which are $(k_d, k_F) = (30, 30)$ and $(30, 90)$. Again, we do not see a NDC when $k_d = k_F$, but we do when $k_d < k_F$, and we only see a NDC when there are meandering jets. The NDL follows the long-wave Rossby speed when there are no jets, but follows a slower

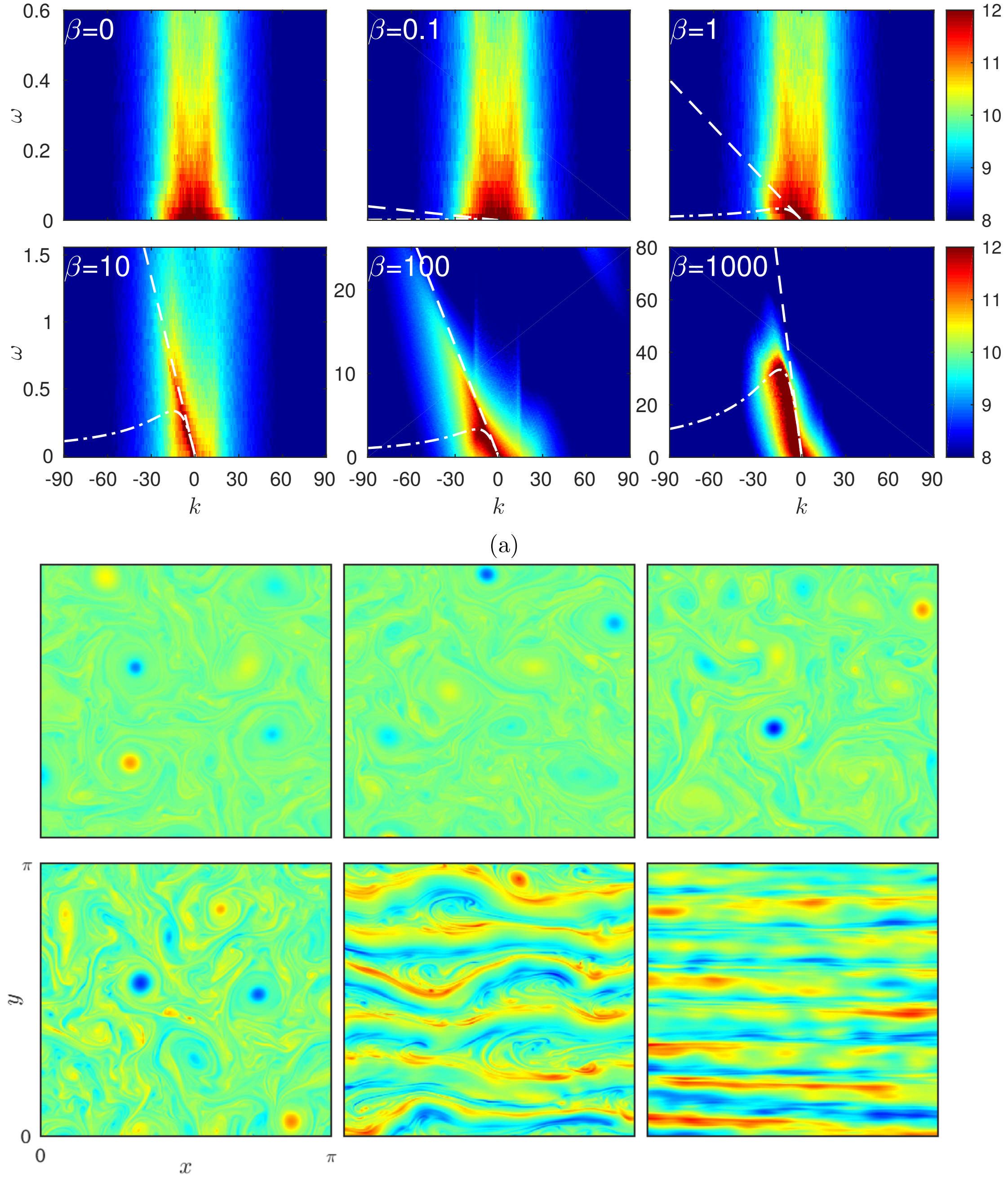

(a)

(b)

Figure 4.4: As in figure 4.2 but for simulations with $(k_d, k_F) = (15, 15)$. (a) Kinetic energy spectra, $\log_{10} E(k, \omega)$. Dashed and dash-dotted lines are as in figure 4.2. In the $\beta = 10$ case, which exhibits no jets, the NDL appears at the long-wave Rossby speed. In the $\beta = 100$ case, which exhibits meandering jets, the NDL is slower. (b) The corresponding snapshots of vorticity.

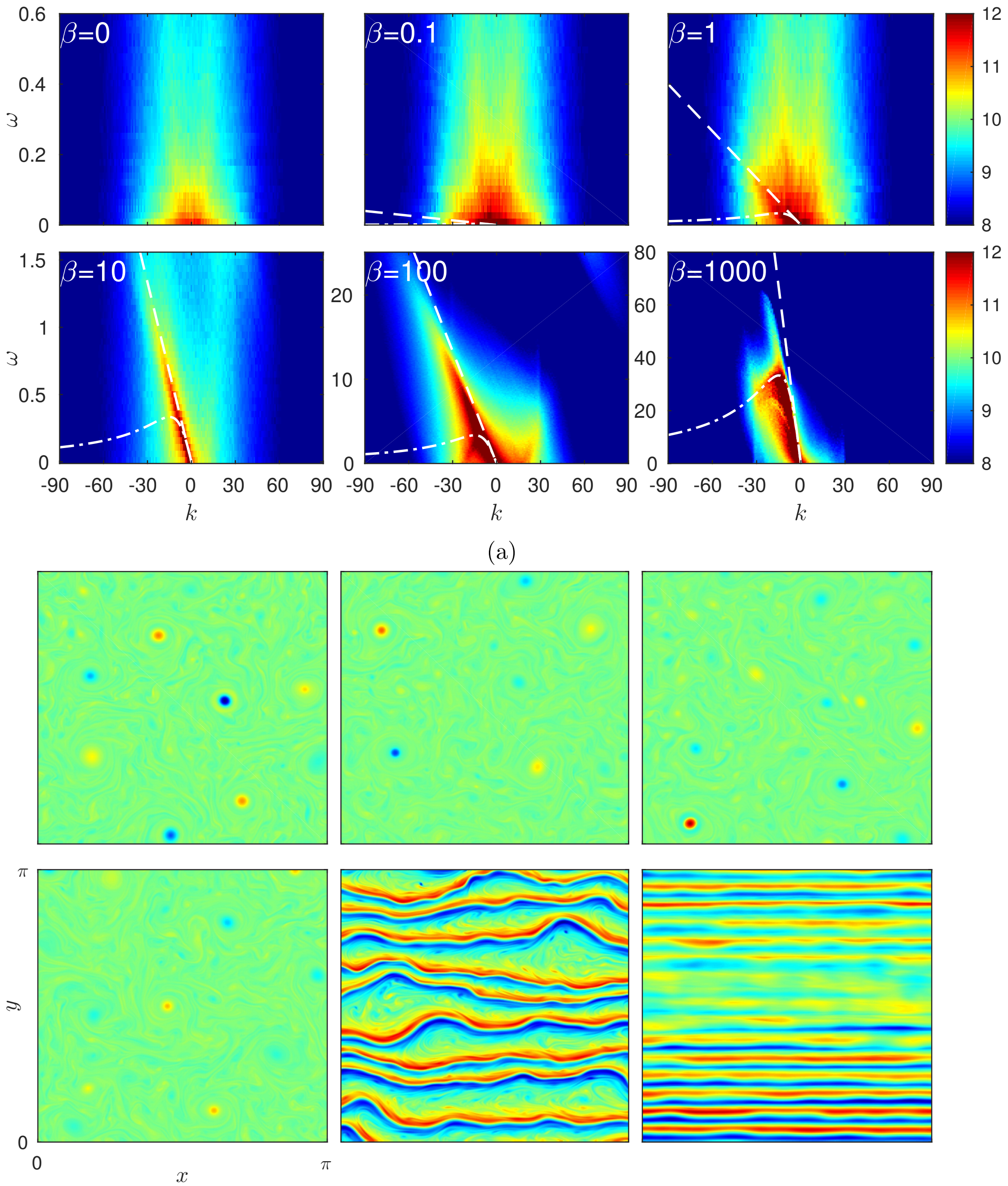

(a)

(b)

Figure 4.5: As in figure 4.2 but for simulations with $(k_d, k_F) = (15, 30)$. (a) Kinetic energy spectra, $\log_{10} E(k, \omega)$. Dashed and dash-dotted lines are as in figure 4.2. In the $\beta = 10$ case, which exhibits no jets, the NDL appears at the long-wave Rossby speed. In the $\beta = 100$ case, which exhibits meandering jets, the NDL is slower. There is a NDC when $\beta = 100$. (b) The corresponding snapshots of vorticity. The $\beta = 100$ case corresponds to meandering jets with no long-lived vortices.

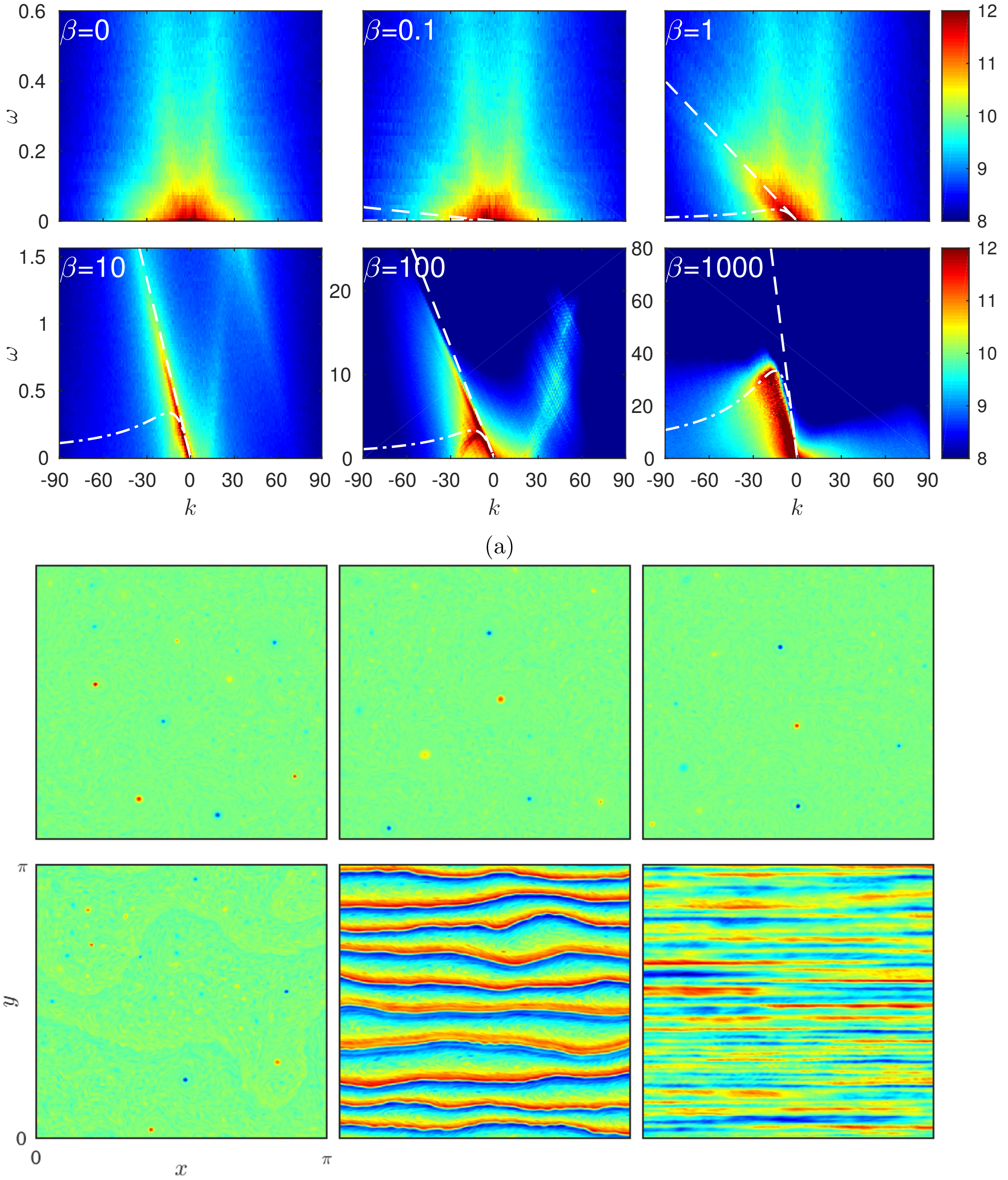

(a)

(b)

Figure 4.6: As in figure 4.2 but for simulations with $(k_d, k_F) = (15, 90)$. (a) Kinetic energy spectra, $\log_{10} E(k, \omega)$. Dashed and dash-dotted lines are as in figure 4.2. In the $\beta = 10$ case, there are weak meandering jets, the NDL is slightly slower than the long-wave Rossby speed, and a weak NDC is apparent at positive k. In the $\beta = 100$ case, the NDL is even slower, and there is a clear NDC. There is a NDC when $\beta = 100$. (b) The corresponding snapshots of vorticity.

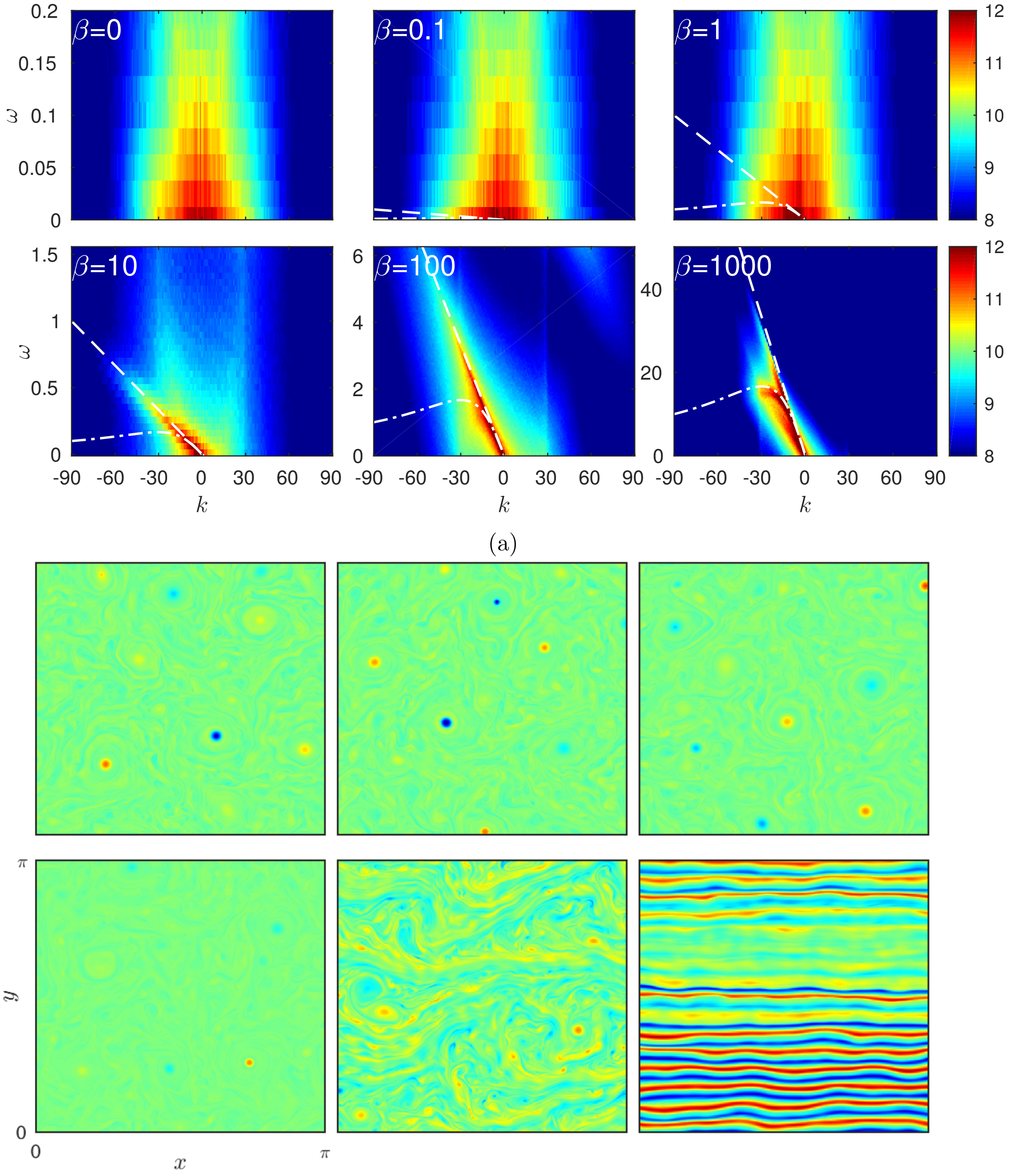

(a)

(b)

Figure 4.7: As in figure 4.2 but for simulations with $(k_d, k_F) = (30, 90)$. (a) Kinetic energy spectra, $\log_{10} E(k,\omega)$. Dashed and dash-dotted lines are as in figure 4.2. In the $\beta = 10$ case, which exhibits no jets, the NDL appears at the long-wave Rossby speed. In the $\beta = 1000$ case, the NDL is slightly slower. (b) The corresponding snapshots of vorticity.

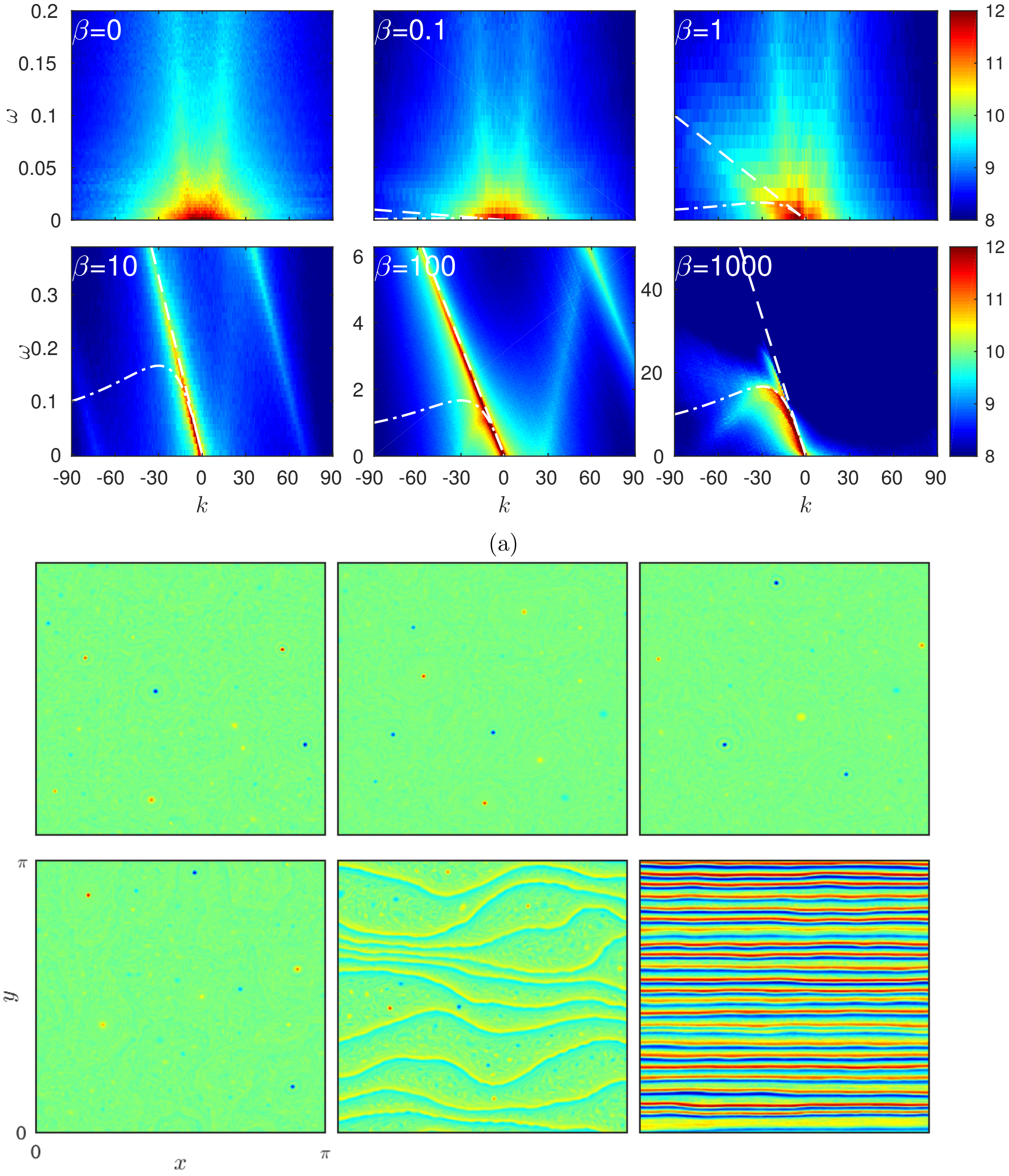

(a)

(b)

Figure 4.8: As in figure 4.2 but for simulations with $(k_d, k_F) = (90, 90)$. (a) Kinetic energy spectra, $\log_{10} E(k,\omega)$. Dashed and dash-dotted lines are as in figure 4.2. In the $\beta = 10$ case, which exhibits no jets, there is a narrow NDL at the long-wave Rossby speed. In the $\beta = 100$ case, which exhibits meandering jets co-existing with vortices, the NDL is slightly slower, and there is a weak NDC. In the $\beta = 100$ case, there is a less pronounced, slower NDL. (b) The corresponding snapshots of vorticity.

propagation speed when when there are jets. The highest β case, which involves nearly zonal jets, still show a NDL in addition to what will later prove to be Rossby waves.

To summarize, we see that for the three values of k_d used here and for a wide range of k_F there is a consistent progression of features as one increases β: isotropic vortices, westward propagating vortices with a NDL at the long-wave Rossby speed, meandering jets with a slower NDL for all k_F and a NDC for $k_F > k_d$, and finally (nearly) zonal jets which roughly follow the linear Rossby dispersion relation. Although this story is consistent from figure to figure, we note large differences in the appearance of the jets from case to case. These differences in the jets make it worthwhile to show snapshots for all of these runs.

4.3.4 Zonal investigation of the NDL and NDC

In this section we look at the NDC in more detail. Whereas before we showed the kinetic energy spectra $E(k, \omega) := \sum_l E(k, l, \omega)$, summed over all meridional wavenumbers, here we show $E(k, l, \omega)$ for various fixed values of l. In addition to the spectra we also show the nonlinear spectral transfers $T(k, \omega) := \sum_l T(k, l, \omega)$ and $T(k, l, \omega)$ for various l.

For each of the three values of $k_d \in \{6, 15, 30\}$, we examine the case that produced the most prominent NDC. We examine te $(k_d, k_F, \beta) = (6, 90, 10)$ case in figure 4.9, the $(15, 90, 100)$ case in figure 4.10, and the $(30, 90, 100)$ case in figure 4.11. As a reminder, the top-left panel of each figure shows the $k\omega$-spectra, already shown earlier, in order to highlight the NDCs again. While all these cases display a NDC, the corresponding jets are quite different.

Figure 4.9a shows $E(k, \omega)$ and $E(k, l, \omega)$ at fixed l for the $(k_d, k_F, \beta) = (6, 90, 10)$ case, which exhibits both a NDL and a NDC. For small l the NDC is strong and there is no NDL. In contrast, for large l the NDL is strong and there is no NDC. Thus, the

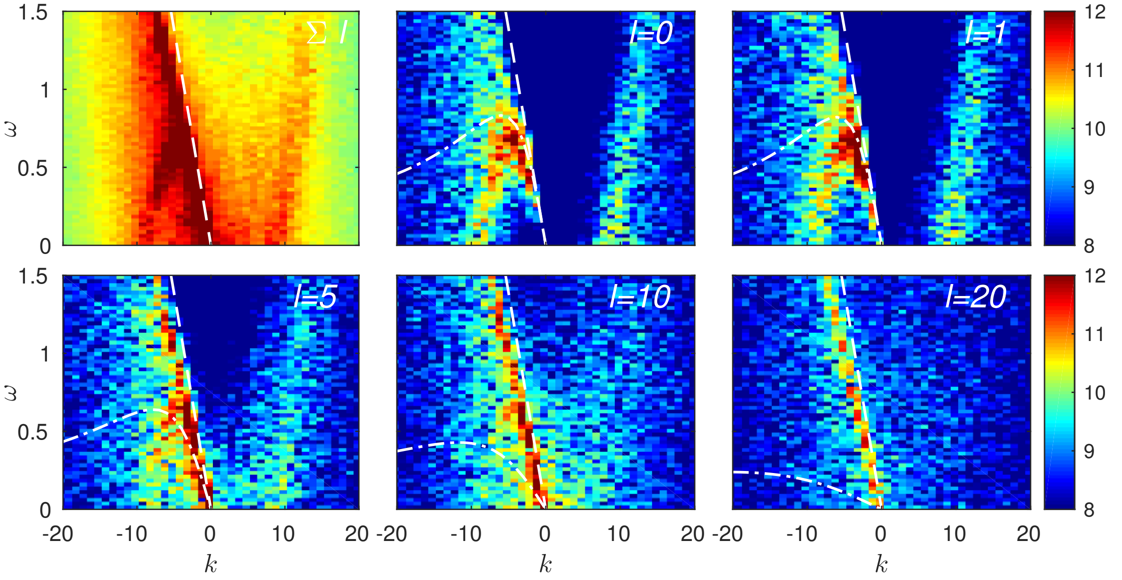

(a)

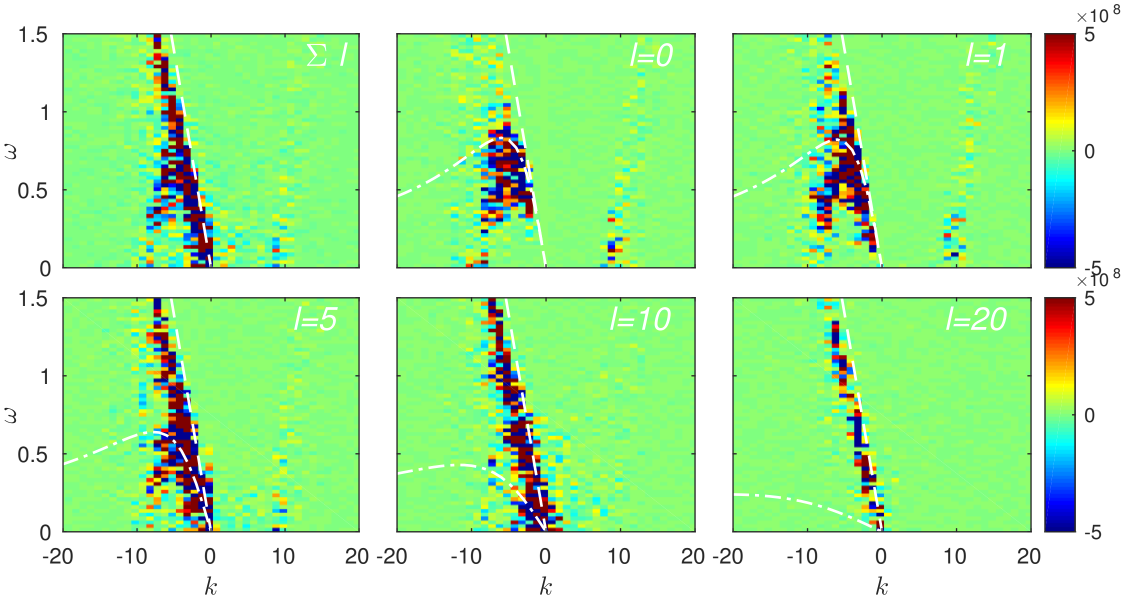

(b)

Figure 4.9: Zonal wavenumber-frequency spectra and nonlinear spectral transfers sliced at constant l for the case $(k_d, k_F, \beta) = (6, 90, 10)$. The corresponding vorticity snapshot can be found in figure 4.3. Dash-dotted line shows propagation at the long-wave Rossby speed. Dash-dotted curve shows the Rossby dispersion relation. (a) Top left shows kinetic energy $\log_{10} E(k, \omega) := \log_{10} \sum_l E(k, l, \omega)$. Other five plots show $\log_{10} E(k, l, \omega)$ at fixed values of $l \in \{0, 1, 5, 10, 20\}$. (b) As in (a), but for nonlinear spectral transfers.

NDC is roughly a meridional phenomena, because typically $k > l$ along the NDC. The NDL involves both zonal and meridional structures, since both $k < l$ and $k > l$ along the NDL.

Figure 4.9b shows the nonlinear spectral transfers $T(k, \omega)$ and $T(k, l, \omega)$ for the same values of l. Displaying the nonlinear transfers explicitly implicates the involvement of nonlinearity in the formation of the NDC and NDL. The transfers behave in a similar manner as the spectra: the NDC dominates at small l while the NDL dominates at large l.

Figure 4.10 shows $E(k, \omega)$, $E(k, l, \omega)$, $T(k, \omega)$ and $T(k, l, \omega)$ at fixed l for the $(k_d, k_F, \beta) = (15, 90, 100)$ case. We remind the reader that $k_d = 15$ is the most oceanographically relevant case, and that figure 4.10 displays the $k_d = 15$ case having the most prominent NDC. The spatio-temporal resolution is much better than in the previous figure, and the story is very clear: the NDC is again most prominent at small l while the NDL dominates at large l. The main difference between the $k_d = 15$ case shown in figure 4.10 and the $k_d = 6$ case shown in figure 4.9 is that the cutoff value of l above which the NDC disappears is now higher. In other words, the meridional modes accessible by the NDC appear to depend on the deformation radius.

Figure 4.11 shows $E(k, \omega)$, $E(k, l, \omega)$, $T(k, \omega)$ and $T(k, l, \omega)$ at fixed l for the $(k_d, k_F, \beta) = (30, 90, 100)$ case, in which the deformation radius is smaller than in the previous two cases. This case differs from the previous two in that the NDC appears to be much weaker. The NDC is clearly seen in the spectra when $l < k_d$, but is barely noticeable in the spectral transfers. Unlike the previous two cases, the NDL is prominent at all l.

4.3.5 Meridional investigation of the NDL and NDC

In this section we examine cross-sections of $E(k, l, \omega)$ at constant zonal wavenumber k, in contrast with the sections at constant l shown in the previous section. We

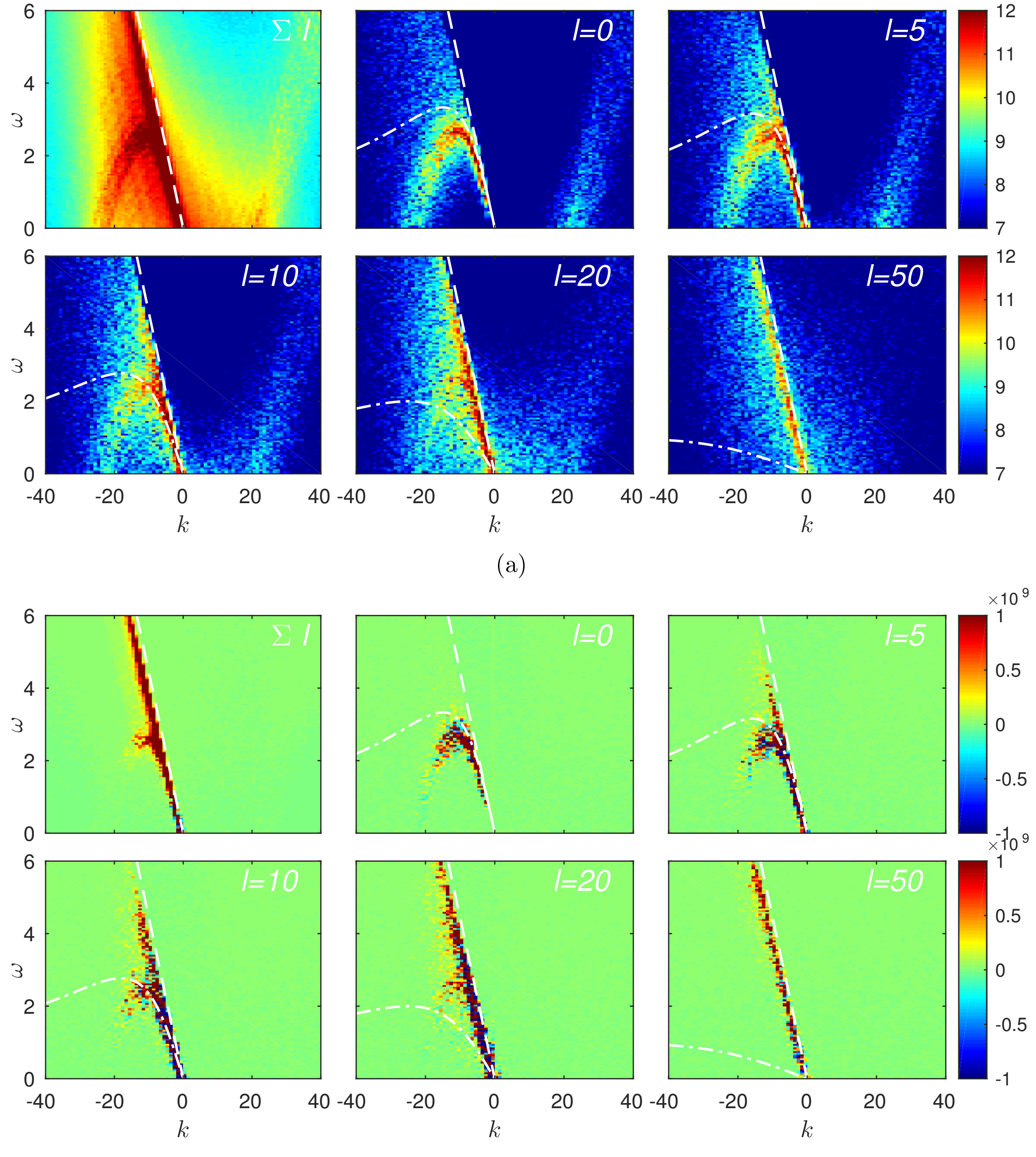

(a)

(b)

Figure 4.10: As in figure 4.9 but for the $(k_d, k_F, \beta) = (15, 90, 100)$ case with $l \in \{0, 5, 10, 20, 50\}$. The corresponding vorticity snapshot can be found in figure 4.6. Dashed and dash-dotted lines are as in figure 4.9.

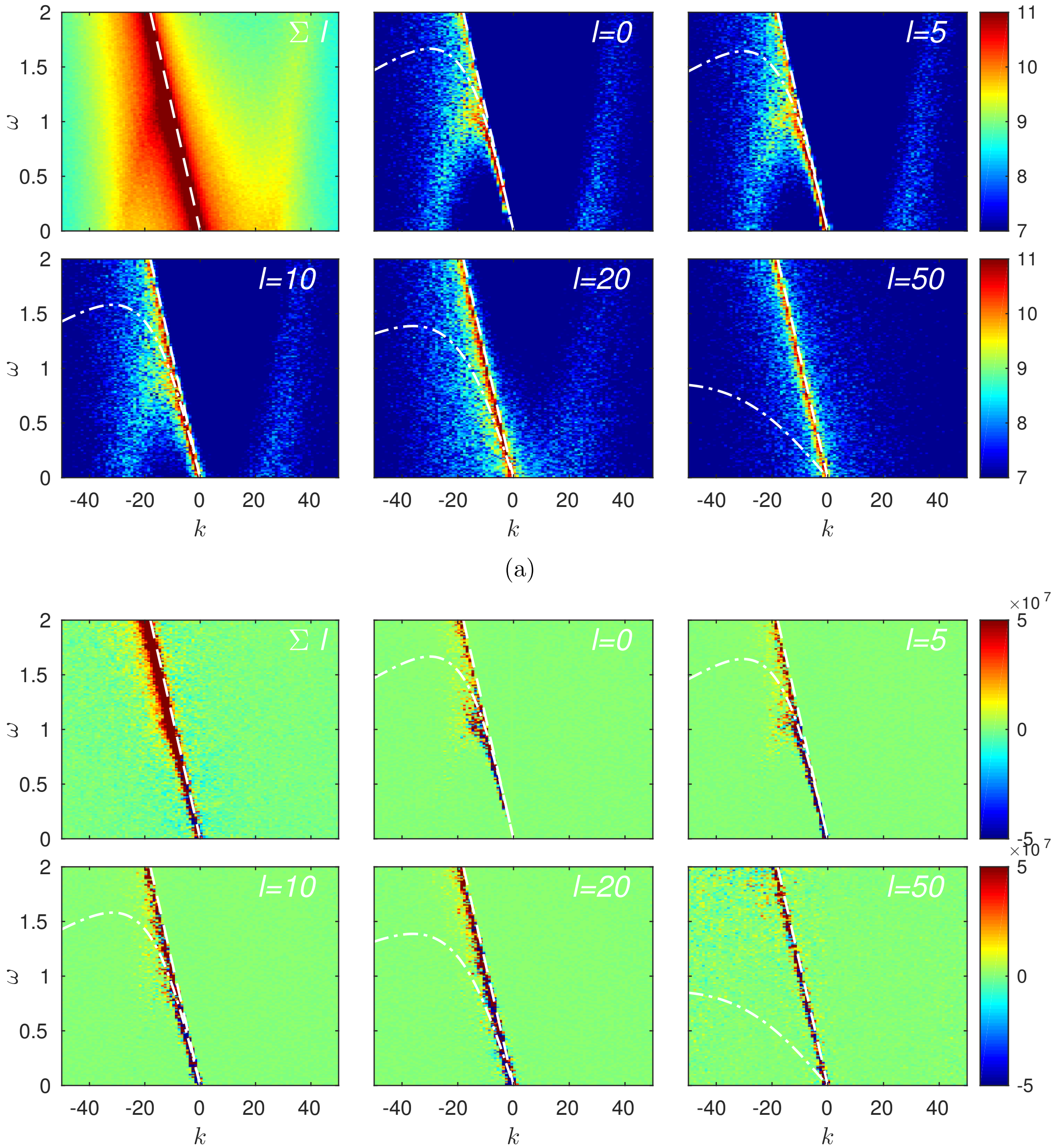

(a)

(b)

Figure 4.11: Zonal wavenumber-frequency spectra and nonlinear spectral transfers sliced at constant l when $(k_d, k_F, \beta) = (30, 90, 100)$. This run produces a strong NDL and a weak NDC. The corresponding vorticity snapshot can be found in figure 4.8. Dashed and dash-dotted lines are as in figure 4.9.

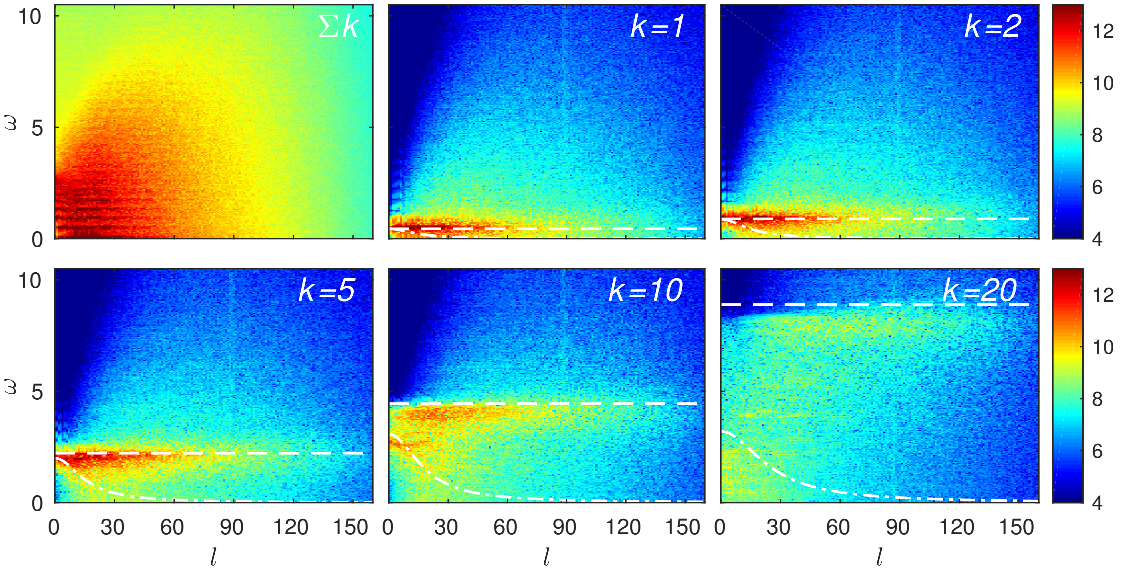

Figure 4.12: Meridional wavenumber-frequency spectra sliced at constant k for the $(k_d, k_F, \beta) = (15, 90, 100)$ case. The corresponding vorticity snapshot can be found in figure 4.6. Dashed lines, as in previous figures, indicate the signature of uniform westward propagation at the long-wave Rossby speed. Dash-dotted curves show the linear Rossby dispersion relation. Top left panel shows kinetic energy $\log_{10} E(l, \omega) := \log_{10} \sum_k E(k, l, \omega)$. Other five plots show $\log_{10} E(k, l, \omega)$ at fixed values of $k \in \{1, 2, 5, 10, 20\}$.

show only a single case, with $k_d = 15$, $k_F = 90$, and $\beta = 100$. This run has the most prominent NDC of all of the $k_d = 15$ runs; recall that $k_d = 15$ has been deemed the most oceanographicaly relevant case. In addition to a NDC this run exhibits a prominent NDL.

Figure 4.12 shows $E(l, \omega) := \sum_k K.E.(k, l, \omega)$ and $E(k, l, \omega)$ for various fixed values of k. The top-left panel shows that $E(l, \omega)$ consists of a sequence of horizontal lines, most clearly at small frequency and wavenumber. For uniform zonal propagation at speed U, the dispersion relation is $\omega = Uk$, which is independent of l and scales linearly with k. Thus, the signature of a NDL in $l\omega$-space is a horizontal line at constant frequency, with the frequency directly proportional to k. In the figure we include dashed lines indicating the location of a hypothetical NDL at the long-wave Rossby speed. We also show the linear Rossby dispersion relation (dash-dotted lines). The figure clearly demonstrates that most of the energy lies along a NDL with speed

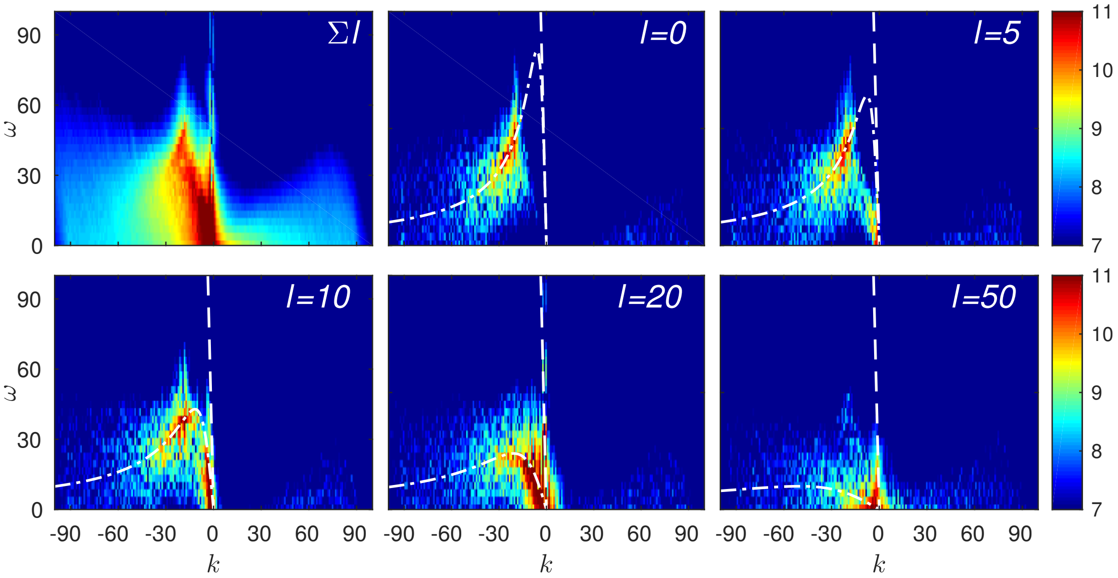

Figure 4.13: Zonal wavenumber-frequency spectra sliced at constant l for the $(k_d, k_F, \beta) = (6, 90, 1000)$ case, which produces strong zonal jets. The corresponding vorticity snapshot can be found in figure 4.3. Dashed and dash-dotted lines are as in figure 4.9. Top left shows kinetic energy $\log_{10} E(k, \omega) := \log_{10} \sum_l E(k, l, \omega)$. Other five plots show $\log_{10} E(k, l, \omega)$ at fixed values of $l \in \{0, 5, 10, 20, 50\}$.

slightly slower than the long-wave Rossby speed. Each stripe in the top-left panel corresponds to one of the discrete values of k, and corresponds to a peak in the frequency spectrum, $E(\omega) := \sum_{k,l} E(k, l, \omega)$, not shown here. Although this run has a prominent NDC, there is no clear signature of the NDC in $l\omega$-space.

4.3.6 Zonal investigation of strong jets

In this section we again examine kinetic energy spectra $E(k, l, \omega)$ for various fixed values of l, but now in simulations with very large values of β, which produce strong nearly zonal jets. In section 4.3.4, investigations of zonal wavenumber-frequency spectra $E(k, \omega)$ could not conclusively determine whether these jets (or waves on the jets) satisfy the linear Rossby dispersion relation.

For each of the three values of $k_d \in \{6, 15, 30\}$, we consider the run with the smallest scale forcing and the highest value of β. Thus, we examine the following three simulations: $(k_d, k_F, \beta) = (6, 90, 1000)$ in figure 4.13, $(15, 90, 1000)$ in figure 4.14, and

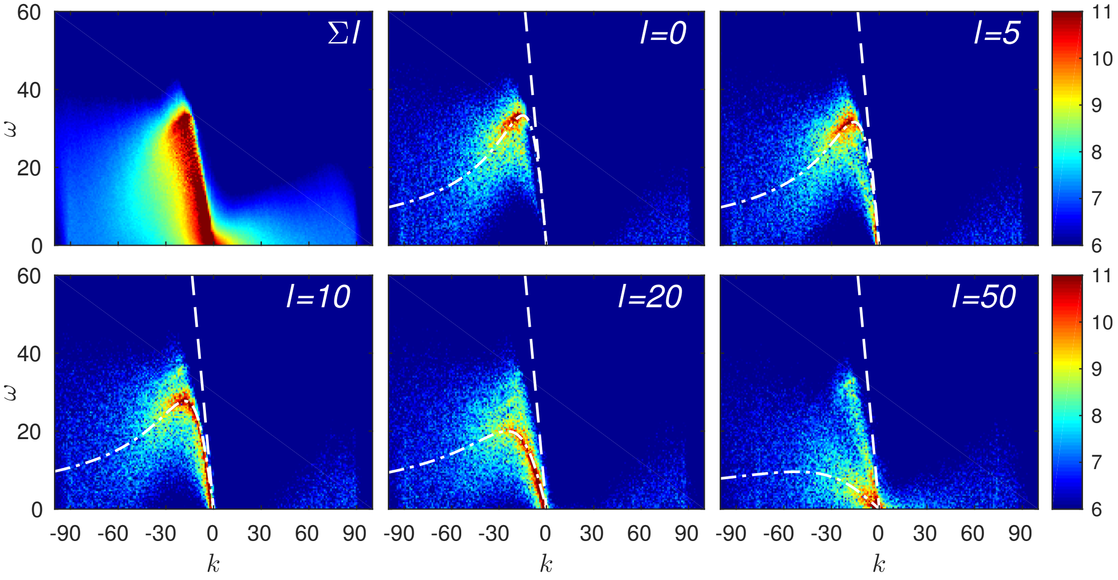

Figure 4.14: As in figure 4.13 but for the $(k_d, k_F, \beta) = (15, 90, 1000)$ case. The corresponding vorticity snapshot can be found in figure 4.6. Dashed and dash-dotted lines are as in figure 4.9.

$(30, 90, 1000)$ in figure 4.15. The top-left panel of each figure shows the $E(k, w)$ while the remaining panels show $E(k, l, \omega)$ for fixed $l \in \{0, 5, 10, 20, 50\}$.

We can summarize these three figures as follows. When $l <= 20$ most of the energy lies along the linear Rossby dispersion relation. When $l = 50$ some energy also appears along a NDL. Specifically in the case $k_d = 30$, when $l = 50$ there is another curve between the NDL and the linear Rossby dispersion relation. It appears in the same location as a NDC would, but it is too short to convincingly claim it is the same phenomenon seen in other runs with lower β.

4.3.7 Meridional investigation of strong jets

To continue our investigation of the simulations with strong zonal jets ($\beta = 1000$), we now show $E(l, \omega) := \sum_k E(k, l, \omega)$ and $E(k, l, \omega)$ at fixed values of k. We use the same runs as in the previous section, but because the $k_d = 6$ has poor resolution we only show the $k_d = 15$ and $k_d = 30$ cases. Those runs had forcing at the smallest scales ($k_F = 90$). We also show the $(k_d, k_F, \beta) = (15, 30, 1000)$ case, which has intermediate-

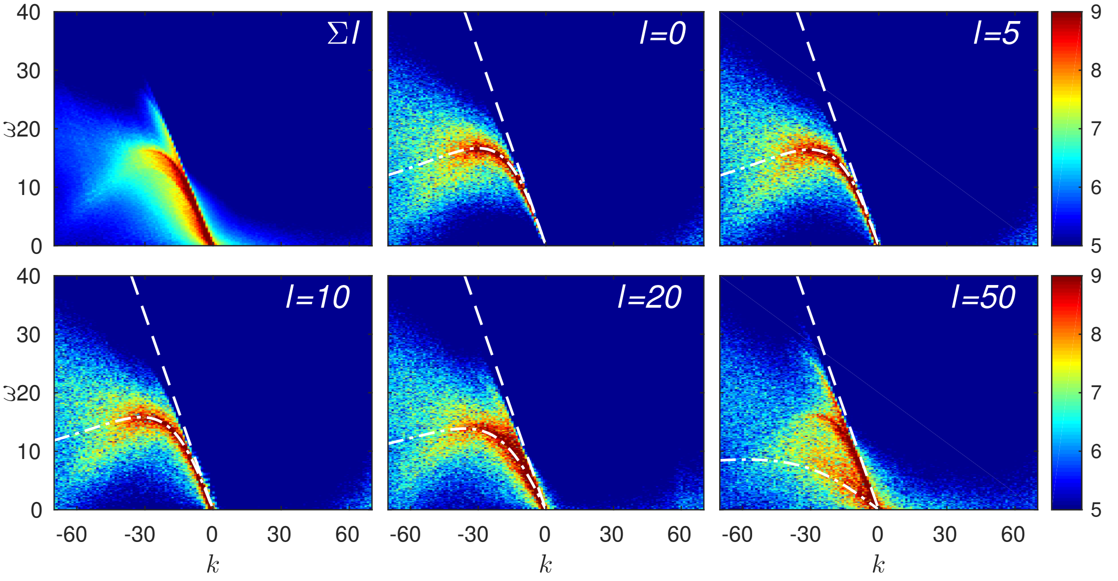

Figure 4.15: As in figure 4.13 but for the $(k_d, k_F, \beta) = (30, 90, 1000)$ case. The corresponding vorticity snapshot can be found in figure 4.8. Dashed and dash-dotted lines are as in figure 4.9.

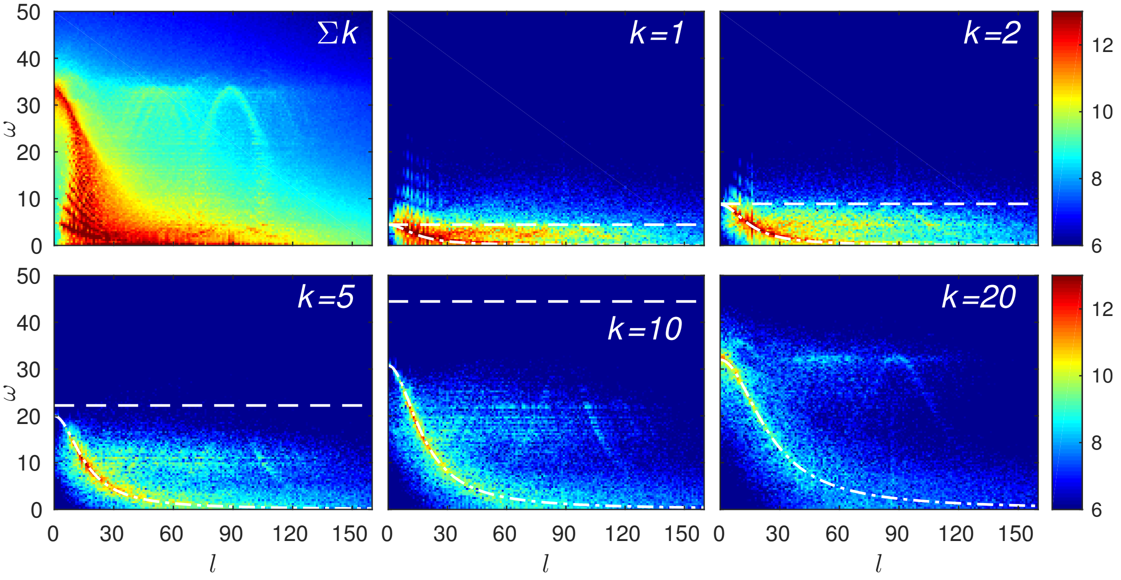

Figure 4.16: Meridional wavenumber-frequency spectra sliced at constant k for the $(k_d, k_F, \beta) = (15, 90, 1000)$ case, which produces strong nearly zonal jets. The corresponding vorticity snapshot can be found in figure 4.6. Dashed lines, as in previous figures, indicate the signature of uniform westward propagation at the long-wave Rossby speed. Dash-dotted curves show the linear Rossby dispersion relation. Top left panel shows kinetic energy $E(l, \omega) := \sum_k E(k, l, \omega)$. Other five plots show $E(k, l, \omega)$ at fixed values of $k \in \{1, 2, 5, 10, 20\}$.

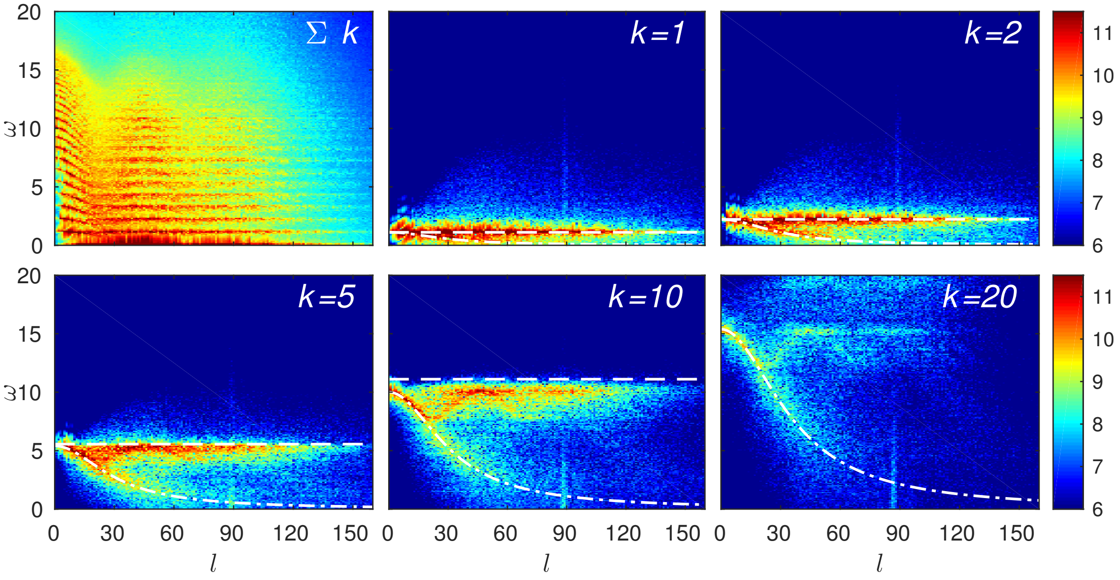

Figure 4.17: As in figure 4.16 but for the $(k_d, k_F, \beta) = (30, 90, 1000)$ case. The corresponding vorticity snapshot can be found in figure 4.8. Dashed and dash-dotted lines are as in figure 4.16.

scale forcing and features a surprising sinusoidal pattern in the spectra that is only hinted at in the other cases.

Figure 4.16 shows $E(l, \omega)$ and $E(k, l, \omega)$ at fixed k for the case $k_d = 15$ (most oceanographically relevant deformation radius) and $k_F = 90$. The top-left panel shows that $E(l, \omega)$ consists of a series of stripes in $l\omega$-space. The remaining panels show that each stripe corresponds to the linear Rossby dispersion relation (dash-dotted curves) for each fixed k. We also see some features that do not follow the linear Rossby dispersion relation: faint hints of additional curves that look somewhat sinusoidal.

Figure 4.17 shows $E(l, \omega)$ and $E(k, l, \omega)$ at fixed k for the case $k_d = 30$ (smallest deformation radius) and $k_F = 90$. The spectra $E(k, \omega)$ is again a series of stripes, but they are not solely attributed to Rossby waves. The stripes are horizontal at large l, indicating uniform westward propagation. As can be seen in the various slices at fixed k, there are three types of curves present in the spectra: the linear Rossby dispersion relation (especially at small l), a NDL with propagation slightly slower than the long-

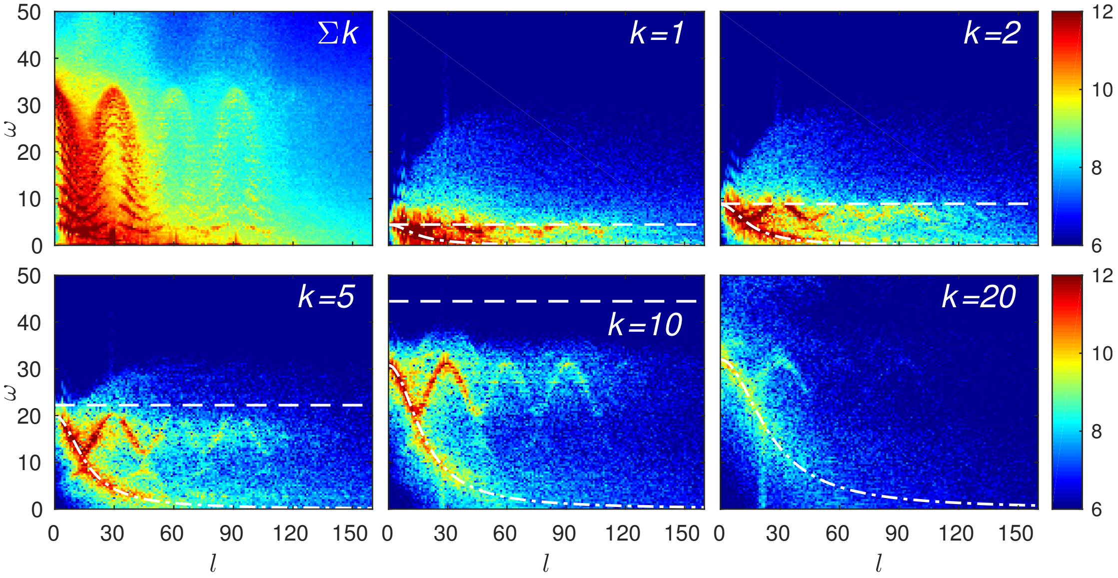

Figure 4.18: As in figure 4.16 but for the $(k_d, k_F, \beta) = (15, 30, 1000)$ case. The corresponding vorticity snapshot can be found in figure 4.5. Dashed and dash-dotted lines are as in figure 4.16.

wave Rossby speed (especially at larger l), and hints of various horizontal sinusoidal curves that coincide with the linear Rossby dispersion relation at small l. The period of each sinusoid appears to be $l_{period} = 45 = k_F/2$, and the maxima occur at $l = 0$, $l = k_F/2$, and $l = k_F$.

Figure 4.17 shows $E(l, \omega)$ and $E(k, l, \omega)$ at fixed k for the case $k_d = 30$ (smallest deformation radius) and $k_F = 30$ (intermediate-scale forcing). There is still energy along the linear Rossby dispersion relation, but we also see a remarkable new feature; for each fixed value of k there is an unambiguous sinusoidal curve. Each sinusoidal curve coincides with the Rossby dispersion relation at small l, and reaches its first minimum at $l = k_d = 15$ where it departs from the linear Rossby dispersion relation. The period of each sinusoid appears to be $l_{period} = 30 = k_F$, and that maxima occur at $l = 0$, $l = k_F$, and $l = 2k_F$.

In all three cases, there is a maxima of the sinusoid at $l = k_F$, and k_F is also an integer multiple of k_d. We suspect these are not coincidences, but are unable to say more here. Further investigation of this phenomenon will be left for future work.

4.4 Summary of Results

We conclude with a summary of the main results of this chapter. We investigate beta-plane turbulence in the wavenumber-frequency domain in the case of a finite deformation radius. Several values of the deformation radius are considered, spanning a range that we argue is most relevant oceanographically. Based on the measurements of eddy size in the North Atlantic by *Eden* (2007), we chose three values of deformation radius $L_d \equiv k_d^{-1}$ that span the observed values of the ratio k_d/k_{PE}. We chose $k_d/k_{PE} \approx 1.3$, 3, and 6, with the middle value being the most common in the North Atlantic, and the outer values being near the extrema of the observations.

We conduct a broader parameter sweep than other recent studies of beta-plane turbulence with a finite deformation radius. We vary a total of three non-dimensional parameters, defined in terms of ratios of length scales. The corresponding wavenumbers are k_{PE}, k_d, k_F, and a fourth wavenumber associated with β (there are several possibilities).

Among several features we report, the most interesting may be the appearance of a non-dispersive curve (NDC) observed in $k\omega$-spectra of kinetic energy when β is just large enough to allow the formation of jets. This NDC involves both westward and eastward phase and group velocities, with the smallest scales traveling eastward. The NDC corresponds to neither Rossby waves nor the previously reported non-dispersive line (NDL) indicative of uniform westward propagation. The formation of a NDC is fairly robust in that it appears for all values of k_d considered here and for all values of $k_F > k_d$ (forcing at scales smaller than but not equal to the deformation radius). The formation of a NDC appears to correspond to the formation of meandering jets (as opposed to purely zonal jets), although the meridional excursion of the jets need not be large.

Besides the discovery of the NDC, we also report on the occurrence, strength, and slope of a NDL for various parameters. Even in the cases where a NDC appears, it bears mentioning that the NDL is still the dominant feature of the spectra. While the NDL can be attributed largely to westward propagating vortices when β is relatively small, the NDL still dominates the $k\omega$-spectra when β is large enough such that jets form (with no or relatively weak vortices). However, if β is turned much higher, the NDL appears to shorten or vanish. Additionally, while it appears that westward propagating vortices propagate westward at approximately the long-wave Rossby speed (consistent with ideas about monopole propagation), when jets dominate the system the resulting NDL indicates a westward propagation speed substantially *slower* than the long-wave Rossby speed. This slower propagation speed is clearest when the potential energy containing scale is not much larger than the deformation radius (i.e. $k_{PE} \lesssim k_d$). The speed of the westward translation of the jets appears to be closer to the phase speed of a Rossby wave with wavevector $\boldsymbol{k}_{jet}$, where $\boldsymbol{k}_{jet}$ is the most energetic mode.

When β is very large, so that strong nearly zonal jets are produced, the $k\omega$-spectra display the signature of Rossby waves. In some cases at high meridional wavenumber l there is evidence of a NDL as well, but the linear Rossby dispersion relation always appears at low l.

We examine $l\omega$-spectra as well as $k\omega$-spectra. Investigations in $l\omega$-space of runs that exhibit a NDC show that the NDC is strongest at low zonal wavenumber k, unlike the NDL which dominates at higher k. This is consistent with the premise that the NDC corresponds to meandering (i.e. non-zonal) jets. When jets are very strong (nearly purely zonal), $l\omega$-spectra indicate that the linear Rossby dispersion is obeyed by a significant fraction of the energy, although sometimes there are significant nonlinear effects as well, such as a perplexing sinusoidal curve in $l\omega$-spectra when sliced at constant k.

Finally, we remark on the effects that forcing scale has on this system. In simulations without jets, the forcing scale appears to determine the size of the vortices (as measured by half-widths of the vorticity peaks). Because of this, the centroids, k_{KE} and k_Z, of kinetic energy and enstrophy are greatly affected by the choice of forcing scale. Furthermore, only when the forcing scale is smaller than the deformation radius, i.e. $k_F > k_d$, do we observe a NDC, and the larger the ratio k_F/k_d the more prominent the NDC. It may be that the appearance of the NDC depends on the formation of narrow jet barriers and that larger scale forcing more easily disrupts such barriers.

CHAPTER V

Conclusion

In this dissertation we developed spatio-temporal spectral transfer and flux diagnostics and applied them to simulations of two-dimensional and quasi-two-dimensional fluids. We also conducted a comprehensive study of wavenumber-frequency spectra over a wide range of parameter space for a quasi-two-dimensional system, specifically the single-layer shallow-water quasi-geostrophic equation. In this final section of the dissertation we discuss some limitations of the research presented here and proposed topics for further investigation.

The theory of spatio-temporal spectral transfers presented in Chapter II is quite general but still has limitations. One limitation is that everything (the data, the time-frequency transform, the detrending) was assumed to be continuous rather than discrete in time. The motivation for assuming temporal continuity is that the original equation of motion involves a time derivative and the mathematical treatment of the continuous case is much cleaner. However, realistic data is always discrete. There are subtle, but important, differences between continuous and discrete time-frequency methods, particularly in wavelet analysis. Rigorously deriving spatio-temporal spectral transfers in the discrete case would be a clear next step for this research.

The model for isotropic sweeping used in Chapter II could also be improved upon. This is not so much a criticism of the model used here as it is a acknowledgment that all models of sweeping, including our own, tend to be quite simplistic. In fact, models of sweeping found in the literature (*Heisenberg*, 1948; *Tennekes*, 1975; *Chen and Kraichnan*, 1989; *Nelkin and Tabor*, 1990; *He and Zhang*, 2006) are often even more simplistic than ours, particularly in regards to the angle between the sweeping velocity and the wavevector of interest. We have made some attempt to develop a more rigorous model of sweeping, but the work is incomplete and was therefore left out of this thesis. A more nuanced treatment of isotropic sweeping in turbulence would be highly welcome, and we note that some progress has already been made (*Kaneda*, 1993; *Kaneda et al.*, 1999; *Cholemari and Arakeri*, 2006; *Dekker*, 2011).

There is also a need for careful interpretation of the spatio-temporal spectral transfer and flux diagnostics. In particular, one could easily be misled by the significance of zero versus non-zero values of spectral energy transfers due to the nonlinear advection term. A value of zero for nonlinear spectral energy transfer at any given wavenumber-frequency mode (k, ω) provides no indication of whether nonlinear triad interactions are active at (k, ω). This is because wavenumber-frequency triad interactions obey local conservation laws, implying that in statistical equilibrium nonlinear transfers should be zero outside of the forcing and dissipation ranges. In the idealized cascade picture, spatial spectral transfers due to nonlinear advection are exactly zero in the cascade range, even though that is precisely the range where nonlinearity plays the dominant role.

One way to circumvent this issue is to note that the nonlinear advection term in spectral space takes the form of a convolution sum. Each term in the sum can be considered to be a separate term in the equation of motion, with a corresponding spectral transfer. Alternatively, the full convolution sum can be separated into a few physically motivated parts. For instance, focusing on the transfer at wavevector $\boldsymbol{k}$, the sum can be split into three parts: transfers into $\boldsymbol{k}$ from larger wavenumbers, transfers into $\boldsymbol{k}$ from smaller wavenumbers, and transfers into $\boldsymbol{k}$ from similar wavenumbers. In the inertial range, while the sum of all three terms would be zero, the individual terms would be non-zero indicating the direction of the cascade. A similar decomposition could take into account frequency triads. Separating the nonlinear spectral transfer into different components as just described would make it more useful as a measure of the role of nonlinearity in moving energy around in wavenumber-frequency space outside of the forcing and dissipation ranges.

Another issue is the effect that persistent vortices may have on the spatio-temporal spectral transfers. In our simulations much of the energy and enstrophy resides within vortices. Perhaps one could calculate the spectral transfers in spatial regions that contain no vortices separately from regions of high vorticity while also calculating the spectral transfers due to the resulting cross-terms. We felt that such an analysis would have been too lengthy for the current presentation, and therefore leave it for future work.

Suppose we were to attempt to calculate spectral transfers within vortices, within the background, and between the two, as suggested in the preceding paragraph. Then, a spatial or temporal wavelet analysis might be more appropriate than a Fourier transform, which is spatially and temporally nonlocal. Because our simulations did have strong vortices, for that reason alone a wavelet analysis may have been better. A Fourier analysis was deemed much simpler as a first step, but future studies of spatio-temporal spectral transfers in systems that have localized features (in space or time) would surely benefit from moving beyond the Fourier transform.

The numerical results in Chapter III performed little investigation of locality versus nonlocality of spatio-temporal spectral triad interactions. In Chapter II we utilized a simple sweeping model to predict the nonlocality of the temporal triads, but in Chapter III we performed no direct investigation of the effect. It would be interesting to quantify the non-locality of the temporal triad interactions analogous to similar studies of spatial triad interactions (*Kraichnan*, 1971; *Burgess and Shepherd*, 2013).

There is a long-running debate over whether the slope of frequency spectra can be derived from Kolmogorov-like arguments, or whether isotropic sweeping causes the slopes in the frequency domain to equal the slopes in the wavenumber domain. Whether a Kolomorov-like argument can be made for frequency spectra depends on whether the temporal spectral transfers are sufficiently local in the inertial range. One might suppose that the simulations in Chapter III could address this issue, but there is a significant obstacle: coherent structures greatly effect spatial spectral slopes, and therefore Kraichnan's spectral slope predications ($-5/3$ and -3) are not applicable. There are plenty of examples in the two-dimensional turbulence literature (*Chen et al.*, 2003, 2006; *Boffetta*, 2007; *Xiao et al.*, 2009; *Boffetta and Musacchio*, 2010) that produce the predicted spectral slopes in the inertial ranges. What distinguishes those simulations from our own is a (perhaps unphysical) choice of forcing that inhibits the production of vortices. If we used such a forcing, which would permit the predicted spatial cascades, in that case a study of the non-locality of temporal triad interactions would be a noteworthy contribution to the cascade picture.

Another limitation of Chapters II and III is that we did not consider the effects of a linear dispersion relation on the spectral transfers. Our simulations were for homogeneous isotropic turbulence for which there is no dispersion relation and for which the effects of "sweeping" provide the only relation between spatial and temporal statistics, at least at small scales. In an energy or enstrophy spatio-temporal spectral budget, the linear dispersion terms are only involved in the time-evolution (or more accurately, τ-evolution) of the complex phase of the spatio-temporal Fourier modes. That means that the linear dispersion relation terms do not take part in a transfer of energy or enstrophy, rendering it unclear precisely what spectral transfers can say about systems dominated by linear waves. Of course, if the nonlinear spectral transfer convolution sum is decomposed into individual triad interactions, then certainly the spectral transfers can say something about interactions among the various linear waves. Further investigation on this topic is needed.

The inclusion of a "planetary beta" term as in the β-plane approximation of a geophysical fluid (e.g. *Vallis*, 2006) may provide an instructive example of a simple case with a linear dispersion relation. Some work has already been done along these lines, as *Chen* (2013); *Chen et al.* (2015) made use of an independently derived spatio-temporal flux to diagnose the effects of striations in barotropic quasi-geostrophic turbulence. We also studied this system in Chapter IV, but we emphasized spectra over spectral transfers, and in most cases the dispersion relation was not at all apparent in the spectra (we mostly observed NDLs and NDCs).

Another limitation of Chapters II and III is that we only applied the diagnostic to numerical simulations of a simple two-dimensional system. Ongoing and future studies of more complicated systems (e.g. the ocean) will surely have to check for effects of data limitations as well. However, such studies will typically not have access to longer or higher resolution datasets for comparison. Our thorough study of the robustness of the diagnostic for two-dimensional turbulence simulations may be regarded as evidence that the diagnostic will be robust in other applications.

In Chapter IV we numerically investigated the single-layer shallow-water quasi-geostrophic equation. We conducted a wide sweep of parameter space, varying the deformation radius, the forcing scale, and planetary beta. We found a range of behaviors in physical space and discovered new features in wavenumber-frequency space. One newly discovered phenomenon is the nonlinear dispersive curve that appears to be a signature of meandering jets. Another discovery is a nondispersive line corresponding to speeds slower than the long-wave Rossby speed when there are jets, in contrast with the nondispersive line at the long-wave Rossby speed when there are propagating vortices without jets. We also detect nonlinear sinusoidal features in $l\omega$-spectra in simulations with very high planetary beta. While the observations of spectral features are interesting in their own right, we would also like to be able to explain them. We conclude this thesis by suggesting some possible research directions that may help to explain the observed spectra.

The existence of the NDL for small β (before the onset of jets) is likely due to westward propagating vortices. There is already much research on the existence of such vortices for various values of k_d and β. In the absence of forcing and dissipation, there exist fully nonlinear, steady state or uniformly propagating, localized solutions called modons, Rossby vortices, or Rossby solitons. Modons were first proposed by *Stern* (1975) for the case $k_d = 0$. *Larichev and Reznik* (1976) considered the case $k_d \neq 0$, and *McWilliams and Flierl* (1979); *Flierl et al.* (1980) considered a two-layer model. Many subsequent studies have made refinements, looked at instability properties, and studied the effects of various background flow regimes (*Antipov et al.*, 1983; *Flierl*, 1987, 1988; *Chassignet and Cushman-Roisin*, 1991; *Nycander and Sutyrin*, 1992; *Smith*, 1997; *Kizner et al.*, 2003; *van Leeuwen*, 2007). In theory westward propagating modons have a north-south anti-symmetry. However, westward propagating coherent vortices observed in simulations or the ocean are typically nearly radially symmetric. A recent study (*Reznik*, 2010) considers this issue and looks at the dynamics of westward propagating non-stationary monopoles.

In theory, Rossby solitons travel faster than the long wave Rossby speed, but our simulations show a NDL at the long wave Rossby speed. According to *Reznik* (2010), sufficiently strong and large ($L_{vortex} > L_d$) monopoles radiate Rossby waves, thus slowing the vortex until its propagation speed reaches the long wave Rossby speed $-\beta L_d^2$. At that speed wave radiation is greatly diminished, and the so-called self-binding effect (*Horton*, 1989) kicks in, which greatly increases the lifetime of the vortex. Thus, the NDL that we observe in experiments without jets can be explained by slowly decaying westward propagating monopoles traveling at the long wave Rossby speed.

An explanation of the NDL for large beta simulations, dominated by meandering jets, is more difficult. The NDLs in large beta simulations correspond to propagation speeds slower than the long wave ($l = 0$) Rossby speed. It is likely not a coincidence that the propagation speed is near the long wave ($l = l_{jet}$) Rossby speed, where l_{jet} is the meridional wavenumber of the dominant mode. A time series of vorticity snapshots shows that the jets translate nearly uniformly westward. That is different from saying that the jets have westward flows, which they of course do. The NDL indicates nearly uniform westward propagation of the structure of the meandering jets, not the direction of the flow within the jets.

We are not aware of any theory for uniform westward propagation of jets. Possibly, such a theory could be derived by modifying the theory for westward propagating modons. One would replace the requirement that the velocity decays to zero at infinity with a requirement of spatial periodicity (perhaps only along the zonal direction). While this may sound simple, it may actually be impossible to find analytical solutions for such a setup. Modons only admit exact solutions for circular geometries and simple relations between stream function and potential vorticity. The geometry of meandering jets is necessarily more complicated.

Explanations of the NDC for large beta (simulations with meandering jets) and for the sinusoidal features seen in $l\omega$-space for very large beta (strong zonal jets) also await theoretical explanations. Perhaps these phenomena can be explained in terms of solitary waves, which take into account some degree of nonlinearity. Most theories of solitary Rossby waves assume that the background flow is zonally uniform, likely a poor assumption in the case of the NDC which appears to correspond to meandering jets. *Hodyss and Nathan* (2002) considered the case of solitary Rossby waves in a zonally varying background, possibly relevant to the NDC. Another possible avenue for explaining the large-beta NDCs is stochastic structural stability theory using second-order cumulant expansions as in *Srinivasan and Young* (2012); *Constantinou et al.* (2014); *Bakas and Ioannou* (2014). Such theories are capable of predicting the emergence of non-zonal structures. Perhaps the form of the NDC could be predicted in terms of modulational instability, as studied recently in *Connaughton et al.* (2010). Finally, *McIntyre* (2008) looked at the interaction of Rossby waves and jets, which might be relevant to the formation of the NDC or the sinusoidal $l\omega$-spectra.

As can be seen, there are a variety of theoretical approaches that could be tried. Different approaches might be needed for different cases (meandering jets versus strong nearly zonal jets). Any successful approach could be generalized to a two-layer model, making it more oceanographically relevant.

APPENDICES

APPENDIX A

Simulation parameters for Chapter IV

k_d	k_F	β	U_{rms}	k_{PE}	k_{Rh}	k_{Rh}/k_d	$\gamma_{Rh} :=$ k_{Rh}/k_{PE}	k'_{Rh}	k'_{Rh}/k_d	$\gamma'_{Rh} :=$ k'_{Rh}/k_{PE}
6	6	0	0.27	4.4	0.0	0.0	0.0	$6.0i$	$1.0i$	$1.4i$
6	6	0.1	0.27	4.4	0.4	0.1	0.1	$6.0i$	$1.0i$	$1.4i$
6	6	1	0.28	4.2	1.3	0.2	0.3	$5.8i$	$1.0i$	$1.4i$
6	6	10	0.25	4.2	4.5	0.7	1.1	$4.0i$	$0.7i$	$0.9i$
6	6	100	1.60	4.6	5.6	0.9	1.2	$2.2i$	$0.4i$	$0.5i$
6	6	1000	1.96	5.7	16.0	2.7	2.8	14.8	2.5	2.6
6	15	0	0.23	5.2	0.0	0.0	0.0	$6.0i$	$1.0i$	$1.2i$
6	15	0.1	0.27	4.8	0.4	0.1	0.1	$6.0i$	$1.0i$	$1.3i$
6	15	1	0.22	5.0	1.5	0.2	0.3	$5.8i$	$1.0i$	$1.2i$
6	15	10	0.26	4.2	4.4	0.7	1.1	$4.1i$	$0.7i$	$1.0i$
6	15	100	1.05	5.6	6.9	1.2	1.2	3.4	0.6	0.6
6	15	1000	0.70	9.2	26.8	4.5	2.9	26.1	4.3	2.8
6	30	0	0.19	5.3	0.0	0.0	0.0	$6.0i$	$1.0i$	$1.1i$
6	30	0.1	0.19	5.6	0.5	0.1	0.1	$6.0i$	$1.0i$	$1.1i$
6	30	1	0.16	5.1	1.8	0.3	0.3	$5.7i$	$1.0i$	$1.1i$
6	30	10	0.22	4.5	4.8	0.8	1.1	$3.6i$	$0.6i$	$0.8i$
6	30	100	0.91	6.4	7.4	1.2	1.2	4.4	0.7	0.7
6	30	1000	0.57	9.3	29.7	4.9	3.2	29.1	4.8	3.1
6	90	0	0.10	5.8	0.0	0.0	0.0	$6.0i$	$1.0i$	$1.0i$
6	90	0.1	0.10	6.1	0.7	0.1	0.1	$6.0i$	$1.0i$	$1.0i$
6	90	1	0.07	5.0	2.7	0.5	0.5	$5.3i$	$0.9i$	$1.1i$
6	90	10	0.17	4.5	5.5	0.9	1.2	$2.5i$	$0.4i$	$0.6i$
6	90	100	0.43	6.3	10.8	1.8	1.7	9.0	1.5	1.4
6	90	1000	0.38	10.7	36.5	6.1	3.4	36.0	6.0	3.4

Table A.1: Dimensional and nondimensional parameters for Chapter IV simulations with $k_d = 6$. Asterisks on k_{PE} values indicate runs that have not reached statistical equilibrium. The modified Rhines wavenumber k'_{Rh} and the resulting nondimensional parameters can be purely imaginary, indicated with $i = \sqrt{-1}$.

k_d	k_F	β	U_{rms}	k_{PE}	k_{Rh}	k_{Rh}/k_d	$\gamma_{Rh} :=$ k_{Rh}/k_{PE}	k'_{Rh}	k'_{Rh}/k_d	$\gamma'_{Rh} :=$ k'_{Rh}/k_{PE}
15	15	0	0.20	4.5	0.0	0.0	0.0	$15.0i$	$1.0i$	$3.3i$
15	15	0.1	0.19	5.1	0.5	0.0	0.1	$15.0i$	$1.0i$	$3.0i$
15	15	1	0.19	4.7	1.6	0.1	0.3	$14.9i$	$1.0i$	$3.2i$
15	15	10	0.16	4.9	5.7	0.4	1.2	$13.9i$	$0.9i$	$2.8i$
15	15	100	0.30	5.4	13.0	0.9	2.4	$7.5i$	$0.5i$	$1.4i$
15	15	1000	0.63	8.1	28.2	1.9	3.5	23.8	1.6	3.0
15	30	0	0.16	4.8	0.0	0.0	0.0	$15.0i$	$1.0i$	$3.1i$
15	30	0.1	0.17	4.8	0.5	0.0	0.1	$15.0i$	$1.0i$	$3.1i$
15	30	1	0.16	5.0	1.8	0.1	0.4	$14.9i$	$1.0i$	$3.0i$
15	30	10	0.13	4.6	6.1	0.4	1.3	$13.7i$	$0.9i$	$3.0i$
15	30	100	0.32	6.0	12.6	0.8	2.1	$8.2i$	$0.5i$	$1.4i$
15	30	1000	0.47	11.3	32.6	2.2	2.9	29.0	1.9	2.6
15	90	0	0.08	4.8	0.0	0.0	0.0	$15.0i$	$1.0i$	$3.1i$
15	90	0.1	0.08	4.7	0.8	0.1	0.2	$15.0i$	$1.0i$	$3.2i$
15	90	1	0.07	4.8	2.6	0.2	0.5	$14.8i$	$1.0i$	$3.1i$
15	90	10	0.08	4.6	8.0	0.5	1.8	$12.7i$	$0.8i$	$2.8i$
15	90	100	0.30	5.7	12.9	0.9	2.3	$7.7i$	$0.5i$	$1.4i$
15	90	1000	0.39	15.0	36.0	2.4	2.4	32.8	2.2	2.2

Table A.2: As in table A.1 but with $k_d = 15$.

k_d	k_F	β	U_{rms}	k_{PE}	k_{Rh}	k_{Rh}/k_d	$\gamma_{Rh} :=$ k_{Rh}/k_{PE}	k'_{Rh}	k'_{Rh}/k_d	$\gamma'_{Rh} :=$ k'_{Rh}/k_{PE}
30	30	0	0.12	5.0	0.0	0.0	0.0	$30.0i$	$1.0i$	$6.0i$
30	30	0.1	0.12	5.0	0.6	0.0	0.1	$30.0i$	$1.0i$	$6.0i$
30	30	1	0.12	5.0	2.0	0.1	0.4	$29.9i$	$1.0i$	$6.0i$
30	30	10	0.12	4.9	6.6	0.2	1.4	$29.3i$	$1.0i$	$6.0i$
30	30	100	1.35	4.3	6.1	0.2	1.4	$29.4i$	$1.0i$	$6.9i$
30	30	1000	0.50	7.7	31.6	1.1	4.1	10.0	0.3	1.3
30	90	0	0.07	4.7	0.0	0.0	0.0	$30.0i$	$1.0i$	$6.4i$
30	90	0.1	0.07	5.3	0.8	0.0	0.2	$30.0i$	$1.0i$	$5.6i$
30	90	1	0.07	5.1	2.7	0.1	0.5	$29.9i$	$1.0i$	$5.9i$
30	90	10	0.07	5.2	8.4	0.3	1.6	$28.8i$	$1.0i$	$5.5i$
30	90	100	0.12	5.0	20.3	0.7	4.0	$22.1i$	$0.7i$	$4.4i$
30	90	1000	0.40	23.7	35.4	1.2	1.5	18.7	0.6	0.8

Table A.3: As in table A.1 but with $k_d = 30$.

BIBLIOGRAPHY

BIBLIOGRAPHY

Antipov, S. V., M. V. Nezlin, V. K. Rodionov, E. N. Snezhkin, and A. S. Trubnikov (1983), Rossby solitons - stability, collisions, asymmetry and generation by flows with a velocity shear, *Zhurnal Eksperimentalnoi I Teoreticheskoi Fiziki*, *84*(4), 1357–1372.

Arbic, B. K., and G. R. Flierl (2003), Coherent vortices and kinetic energy ribbons in asymptotic, quasi two-dimensional f-plane turbulence, *Physics of Fluids*, *15*(8), 2177–2189, doi:http://dx.doi.org/10.1063/1.1582183.

Arbic, B. K., R. B. Scott, G. R. Flierl, A. J. Morten, J. G. Richman, and J. F. Shriver (2012), Nonlinear cascades of surface oceanic geostrophic kinetic energy in the frequency domain, *J. of Phys. Oceanogr.*, *42*(9), 1577–1600, doi:10.1175/jpo-d-11-0151.1.

Arbic, B. K., M. Mueller, J. G. Richman, J. F. Shriver, A. J. Morten, R. B. Scott, G. Serazin, and T. Penduff (2014), Geostrophic Turbulence in the Frequency-Wavenumber Domain: Eddy-Driven Low-Frequency Variability, *J. Phys. Oceanogr.*, *44*(8), 2050–2069, doi:10.1175/JPO-D-13-054.1.

Babiano, A., and T. Dubos (2005), On the contribution of coherent vortices to the two-dimensional inverse energy cascade, *Journal of Fluid Mechanics*, *529*, 97–116, doi:10.1017/S0022112004003271.

Bahraminasab, A., M. D. Niry, J. Davoudi, M. Reza Rahimi Tabar, A. A. Masoudi, and K. R. Sreenivasan (2008), Taylor's frozen-flow hypothesis in burgers turbulence, *Phys. Rev. E*, *77*, 065,302, doi:10.1103/PhysRevE.77.065302.

Bakas, N. A., and P. J. Ioannou (2014), A theory for the emergence of coherent structures in beta-plane turbulence, *Journal of Fluid Mechanics*, *740*, 312–341, doi:10.1017/jfm.2013.663.

Batchelor, G. K. (1969), Computation of the energy spectrum in homogeneous two-dimensional turbulence, *Phys. Fluids*, *12*, 233–239, doi:10.1063/1.1692443.

Berloff, P., and I. Kamenkovich (2013a), On spectral analysis of mesoscale eddies. part i: linear analysis, *J. Phys. Oceanogr.*, *43*(12), 2505–2527, doi:10.1175/JPO-D-12-0232.1.

Berloff, P., and I. Kamenkovich (2013b), On spectral analysis of mesoscale eddies. part ii: nonlinear analysis, *J. Phys. Oceanogr.*, *43*(12), 2528–2544, doi:10.1175/JPO-D-12-0233.1.

Boffetta, G. (2007), Energy and enstrophy fluxes in the double cascade of two-dimensional turbulence, *J. Fluid Mech.*, *589*, 253–260, doi: 10.1017/S0022112007008014.

Boffetta, G., and R. E. Ecke (2012), Two-dimensional turbulence, in *Annu. Rev. Fluid Mech. Vol. 44*, *Annu. Rev. Fluid Mech.*, vol. 44, edited by Davis, S. H. and Moin, P., pp. 427–451, Annual Reviews, doi:10.1146/annurev-fluid-120710-101240.

Boffetta, G., and S. Musacchio (2010), Evidence for the double cascade scenario in two-dimensional turbulence, *Phys. Rev. E*, *82*(1, 2), doi: 10.1103/PhysRevE.82.016307.

Bos, W. J. T., and J.-P. Bertoglio (2009), Large-scale bottleneck effect in two-dimensional turbulence, *J. of Turbul.*, *10*(30), 1–8, doi: 10.1080/14685240903273873.

Buckwar, E., and R. Winkler (2006), Multistep methods for sdes and their application to problems with small noise, *SIAM Journal on Numerical Analysis*, *44*(2), 779–803.

Buckwar, E., and R. Winkler (2007), Improved linear multi-step methods for stochastic ordinary differential equations, *Journal of Computational and Applied Mathematics*, *205*(2), 912–922.

Burgess, B. H., and T. G. Shepherd (2013), Spectral non-locality, absolute equilibria and Kraichnan-Leith-Batchelor phenomenology in two-dimensional turbulent energy cascades, *Journal of Fluid Mechanics*, *725*, 332–371, doi:10.1017/jfm.2013.192.

Cadot, O., J. Hugues Titon, and D. Bonn (2003), Experimental observation of resonances in modulated turbulence, *J. Fluid Mech.*, *485*, 161–170, doi: 10.1017/S0022112003004592.

Canuto, C., M. Y. Hussaini, A. Quarteroni, and T. A. Zang (2007a), *Spectral Methods: Fundamentals in Single Domains*, Scientific Computation, Springer Berlin Heidelberg.

Canuto, C., M. Y. Hussaini, A. Quarteroni, and T. A. Zang (2007b), *Spectral Methods: Evolution to Complex Geometries and Applications to Fluid Dynamics*, Scientific Computation, Springer Berlin Heidelberg.

Chassignet, E. P., and B. Cushman-Roisin (1991), On the influence of a lower layer on the propagation of nonlinear oceanic eddies, *J. Phys. Oceanogr.*, *21*(7), 939–957, doi:10.1175/1520-0485(1991)021⟨0939:OTIOAL⟩2.0.CO;2.

Chelton, D. B., R. A. DeSzoeke, M. G. Schlax, K. El Naggar, and N. Siwertz (1998), Geographical variability of the first baroclinic Rossby radius of deformation, *J. Phys. Oceanogr.*, *28*(3), 433–460, doi:10.1175/1520-0485(1998)028⟨0433:GVOTFB⟩2.0.CO;2.

Chen, R. (2013), Energy pathways and structures of oceanic eddies from the ECCO2 state estimate and simplified models, Ph.D. thesis, Massachusetts Institute of Technology, (chapter 5).

Chen, R., G. R. Flierl, and C. Wunsch (2015), Quantifying and Interpreting Striations in a Subtropical Gyre: A Spectral Perspective, *J. Phys. Oceanogr.*, *45*(2), 387–406, doi:10.1175/JPO-D-14-0038.1.

Chen, S. Y., and R. H. Kraichnan (1989), Sweeping decorrelation in isotropic turbulence, *Phys. Fluids A-Fluid*, *1*(12), 2019–2024, doi:10.1063/1.857475.

Chen, S. Y., R. E. Ecke, G. L. Eyink, X. Wang, and Z. L. Xiao (2003), Physical mechanism of the two-dimensional enstrophy cascade, *Phys. Rev. Lett.*, *91*, doi:10.1103/physrevlett.91.214501.

Chen, S. Y., R. E. Ecke, G. L. Eyink, M. Rivera, M. P. Wan, and Z. L. Xiao (2006), Physical mechanism of the two-dimensional inverse energy cascade, *Phys. Rev. Lett.*, *96*(8), doi:10.1103/physrevlett.96.084502.

Chiu, W. (1970), On the spectral equations and the statistical energy spectrum of atmospheric motions in the frequency domain, *Tellus*, *22*(6), 608–619, doi:10.1111/j.2153-3490.1970.tb00529.x.

Cholemari, M. R., and J. H. Arakeri (2006), A model relating Eulerian spatial and temporal velocity correlations, *Journal of Fluid Mechanics*, *551*, 19–29, doi:10.1017/S0022112005008074.

Cohen, L. (1995), *Time-frequency analysis*, Prentice Hall Signal Processing Series, 1 ed., Prentice Hall PTR.

Connaughton, C. P., B. T. Nadiga, S. V. Nazarenko, and B. E. Quinn (2010), Modulational instability of Rossby and drift waves and generation of zonal jets, *Journal of Fluid Mechanics*, *654*, 207–231, doi:10.1017/S0022112010000510.

Constantinou, N. C., B. F. Farrell, and P. J. Ioannou (2014), Emergence and equilibration of jets in beta-plane turbulence: Applications of stochastic structural stability theory, *Journal of the Atmospheric Sciences*, *71*(5), 1818–1842, doi:10.1175/JAS-D-13-076.1.

Danilov, S., and V. M. Gryanik (2004), Barotropic beta-plane turbulence in a regime with strong zonal jets revisited, *Journal of the Atmospheric Sciences*, *61*(18), 2283–2295, doi:10.1175/1520-0469(2004)061⟨2283:BBTIAR⟩2.0.CO;2.

Danilov, S., and D. Gurarie (2001), Forced two-dimensional turbulence in spectral and physical space, *Physical Review E*, *63*(6, 1), doi:10.1103/PhysRevE.63.061208.

Danilov, S., and D. Gurarie (2004), Scaling, spectra and zonal jets in beta-plane turbulence, *Physics of Fluids*, *16*(7), 2592–2603, doi:10.1063/1.1752928.

Dekker, H. (2011), Turbulence: Large-scale sweeping and the emergence of small-scale Kolmogorov spectra, *Physical Review E*, *84*(2, 2), doi: 10.1103/PhysRevE.84.026302.

Del Alamo, J. C., and J. Jimenez (2009), Estimation of turbulent convection velocities and corrections to Taylor's approximation, *Journal of Fluid Mechanics*, *640*, 5–26, doi:10.1017/S0022112009991029.

Donner, L. J., et al. (2011), The Dynamical Core, Physical Parameterizations, and Basic Simulation Characteristics of the Atmospheric Component AM3 of the GFDL Global Coupled Model CM3, *Journal of Climate*, *24*(13), 3484–3519, doi: 10.1175/2011JCLI3955.1.

Dosio, A., J. V. G. De Arellano, A. A. M. Holtslag, and P. J. H. Builtjes (2005), Relating Eulerian and Lagrangian statistics for the turbulent dispersion in the atmospheric convective boundary layer, *Journal of the Atmospheric Sciences* , *62*(4), 1175–1191, doi:10.1175/JAS3393.1.

Dritschel, D. G., R. K. Scott, C. Macaskill, G. A. Gottwald, and C. V. Tran (2009), Late time evolution of unforced inviscid two-dimensional turbulence, *Journal of Fluid Mechanics*, *640*, 215–233, doi:10.1017/S0022112009991121.

Early, J. J., R. M. Samelson, and D. B. Chelton (2011), The evolution and propagation of quasigeostrophic ocean eddies, *J. Phys. Oceanogr.*, *41*(8), 1535–1555, doi:10.1175/2011JPO4601.1.

Eden, C. (2007), Eddy length scales in the North Atlantic Ocean, *Journal of Geophysical Research-Oceans*, *112*(C6), doi:10.1029/2006JC003901.

Effinger, H., and S. Grossmann (1987), Static structure-function of turbulent-flow from the Navier-Stokes equations, *Z. Phys. B Con. Mat.*, *66*(3), 289–304, doi: 10.1007/bf01305419.

Elipot, S., and S. T. Gille (2009), Estimates of wind energy input to the Ekman layer in the Southern Ocean from surface drifter data, *Journal of Geophysical Research-Oceans*, *114*, doi:10.1029/2008JC005170.

Eyink, G. L. (2006a), A turbulent constitutive law for the two-dimensional inverse energy cascade, *J. Fluid Mech.*, *549*, 191–214, doi:10.1017/S0022112005007883.

Eyink, G. L. (2006b), Multi-scale gradient expansion of the turbulent stress tensor, *J. Fluid Mech.*, *549*, 159–190, doi:10.1017/S0022112005007895.

Flierl, G. R. (1987), Isolated eddy models in geophysics, *Annual Review of Fluid Mechanics*, *19*, 493–530, doi:10.1146/annurev.fluid.19.1.493.

Flierl, G. R. (1988), On the instability of geostrophic vortices, *Journal of Fluid Mechanics*, *197*, 349–388, doi:10.1017/S0022112088003283.

Flierl, G. R., V. D. Larichev, J. C. McWilliams, and G. M. Reznik (1980), The dynamics of baroclinic and barotropic solitary eddies, *Dynamics of Atmospheres and Oceans*, *5*(1), 1–41, doi:10.1016/0377-0265(80)90009-3.

Frisch, U. (1995), *Turbulence: the legacy of A. N. Kolmogorov*, Cambridge University Press.

Frisch, U., S. Kurien, R. Pandit, W. Pauls, S. S. Ray, A. Wirth, and J.-Z. Zhu (2008), Hyperviscosity, Galerkin truncation, and bottlenecks in turbulence, *Phys. Rev. Lett.*, *101*(14), 144501, doi:10.1103/PhysRevLett.101.144501.

Galperin, B., S. Sukoriansky, and N. Dikovskaya (2010), Geophysical flows with anisotropic turbulence and dispersive waves: flows with a beta-effect, *Ocean Dynamics*, *60*(2, SI), 427–441, doi:10.1007/s10236-010-0278-2, 1st International Workshop on Modeling the Ocean, Natl Taiwan Normal Univ, Taipei, Taiwan, Feb 23-26, 2009.

He, G. W., and J. B. Zhang (2006), Elliptic model for space-time correlations in turbulent shear flows, *Physical Review E*, *73*(5, 2), doi:10.1103/PhysRevE.73.055303.

Heisenberg, W. (1948), Zur statistischen theorie der turbulenz, *Z. Phys.*, *124*(7-12), 628–657, doi:10.1007/BF01668899.

Hill, R. J. (1996), Corrections to Taylor's frozen turbulence approximation, *Atmospheric Research* , *40*(2-4), 153–175, doi:10.1016/0169-8095(95)00032-1.

Hlawatsch, F., and F. Auger (2008), *Time-frequency analysis: concepts and methods*, Digital signal and image processing series, ISTE.

Hodyss, D., and T. R. Nathan (2002), Solitary Rossby waves in zonally varying jet flows, *Geophysical and Astrophysical Fluid Dynamics*, *96*(3), 239–262, doi:10.1080/03091920290011012.

Hogg, A. M., W. K. Dewar, P. D. Killworth, and J. R. Blundell (2003), A quasi-geostrophic coupled model (Q-GCM), *Monthly Weather Review*, *131*(10), 2261–2278, doi:10.1175/1520-0493(2003)131⟨2261:AQCMQ⟩2.0.CO;2.

Hooghoudt, J. O., D. Lohse, and F. Toschi (2001), Decaying and kicked turbulence in a shell model, *Phys. Fluids*, *13*(7), 2013–2018, doi:10.1063/1.1375146.

Horton, W. (1989), Drift wave vortices and anomalous transport, *Pysics of Fluids B – Plasma Pysics*, *1*(3), 524–537, doi:10.1063/1.859168.

Iwayama, T., T. G. Shepherd, and T. Watanabe (2002), An 'ideal' form of decaying two-dimensional turbulence, *Journal of Fluid Mechanics*, *456*, 183–198, doi: 10.1017/S0022112001007509.

Kaneda, Y. (1993), Lagrangian and Eulerian time correlations in turbulence, *Physics of Fluids A-Fluid Dynamics*, *5*(11), 2835–2845, doi:10.1063/1.858747.

Kaneda, Y., T. Ishihara, and K. Gotoh (1999), Taylor expansions in powers of time of Lagrangian and Eulerian two-point two-time velocity correlations in turbulence, *Physics of Fluids*, *11*(8), 2154–2166, doi:10.1063/1.870077.

Kellay, H., and W. I. Goldburg (2002), Two-dimensional turbulence: a review of some recent experiments, *Rep. Prog. Phys.*, *65*(5), 845–894, doi:10.1088/0034-4885/65/5/204.

Kizner, Z., D. Berson, G. Reznik, and G. Sutyrin (2003), The theory of the beta-plane baroclinic topographic modons, *Geophysical and Astrophysical Fluid Dynamics*, *97*(3), 175–211, doi:10.1080/0309192031000108706.

Kolmogorov, A. N. (1941a), The local structure of turbulence in incompressible viscous fluid for very large Reynolds' numbers, *Dokl. Akad. Nauk SSSR*, *30*, 301–305.

Kolmogorov, A. N. (1941b), Dissipation of energy in locally isotropic turbulence, *Dokl. Akad. Nauk SSSR*, *32*, 16.

Kraichnan, R. H. (1967), Inertial ranges in two-dimensional turbulence, *Phys. Fluids*, *10*, 1417–1423, doi:10.1063/1.1762301.

Kraichnan, R. H. (1971), Inertial-range transfer in 2-dimensional and 3-dimensional turbulence, *J. Fluid Mech.*, *47*, 525–535, doi:10.1017/s0022112071001216.

Kraichnan, R. H., and D. Montgomery (1980), Two-dimensional turbulence, *Rep. Prog. Phys.*, *43*(5), 547–619, doi:10.1088/0034-4885/43/5/001.

Kuczaj, A. K., B. J. Geurts, and D. Lohse (2006), Response maxima in time-modulated turbulence: direct numerical simulations, *Europhys. Lett.*, *73*(6), 851.

Kuczaj, A. K., B. J. Geurts, D. Lohse, and W. van de Water (2008), Turbulence modification by periodically modulated scale-dependent forcing, *Comput. Fluids*, *37*(7), 816–824, doi:10.1016/j.compfluid.2007.01.012.

Kukharkin, N., and S. A. Orszag (1996), Generation and structure of Rossby vortices in rotating fluids, *Physical Review E*, *54*(5), R4524–R4527.

Kukharkin, N., S. A. Orszag, and V. Yakhot (1995), Auasicrystallization of vortices in drift-wave turbulence, *Physical Review Letters*, *75*(13), 2486–2489, doi: 10.1103/PhysRevLett.75.2486.

Lamorgese, A. G., D. A. Caughey, and S. B. Pope (2005), Direct numerical simulation of homogeneous turbulence with hyperviscosity, *Phys. Fluids*, *17*(1), 015,106, doi: 10.1063/1.1833415.

Larichev, V. D., and J. C. McWilliams (1991), Weakly decaying turbulence in an equivalent-barotropic fluid, *Physics of Fluids A-Fluid Dynamics*, *3*(5, 1), 938–950, doi:10.1063/1.857970.

Larichev, V. D., and G. M. Reznik (1976), 2-Dimensional solitary Rossby waves, *Doklady Akademii Nauk Sssr*, *231*(5), 1077–1079.

Leith, C. E. (1968), Diffusion approximation for 2-dimensional turbulence, *Phys. Fluids*, *11*(3), 671–672, doi:10.1063/1.1691968.

Lilly, D. K. (1969), Numerical simulation of two-dimensional turbulence, *Phys. Fluids Suppl.*, *12*, 240–249.

Lohse, D. (2000), Periodically kicked turbulence, *Phys. Rev. E*, *62*, 4946–4949, doi: 10.1103/physreve.62.4946.

Lumley, J. L. (1965), Interpretation of time spectra measured in high-intensity shear flows, *Physics Of Fluids*, *8*(6), 1056, doi:10.1063/1.1761355.

Maltrud, M. E., and G. K. Vallis (1991), Energy-spectra and coherent structures in forced 2-dimensional and beta-plane turbulence, *J. Fluid Mech.*, *228*, 321–342, doi:10.1017/s0022112091002720.

Mandec, G. (2008), Nemo ocean engine, *Note du Pole de modelisation*, *27*, doi: http://dx.doi.org/10.1063/1.1582183.

McIntyre, M. E. (2008), Potential-vorticity inversion and the wave-turbulence jigsaw: some recent clarifications, *Advances in Geosciences*, *15*, 47–56, doi:10.5194/adgeo-15-47-2008.

McWilliams, J. C., and G. R. Flierl (1979), On the evolution of isolated, nonlinear vortices, *J. Phys. Oceanogr.*, *9*, 1155–1182, doi:10.1175/1520-0485(1979)009⟨1155:OTEOIN⟩2.0.CO;2.

Moin, P. (2009), Revisiting Taylor's hypothesis, *Journal of Fluid Mechanics* , *640*, 1–4, doi:10.1017/S0022112009992126.

Müller, M., B. K. Arbic, J. G. Richman, J. F. Shriver, E. L. Kunze, R. B. Scott, A. J. Wallcraft, and L. Zamudio (2015), Toward an internal gravity wave spectrum in global ocean models, *Geophysical Research Letters*, *42*(9), 3474–3481, doi: 10.1002/2015GL063365.

Nelkin, M., and M. Tabor (1990), Time correlations and random sweeping in isotropic turbulence, *Phys. Fluids*, *2*(1), 81–83, doi:10.1063/1.857684.

Newton, I. (1687), *Philosophiæ Naturalis Principia Mathematica*, Jussu Societatis Regiæ ac Typis Joseph Streater.

Nycander, J., and G. G. Sutyrin (1992), Steadily translating anticyclones on the beta-plane, *Dynamics of Atmospheres and Oceans*, *16*(6), 473–498, doi:10.1016/0377-0265(92)90002-B.

Obukhov, A. M. (1941a), On the distribution of energy in the spectrum of turbulent flow, *Dokl. Akad. Nauk SSSR*, *32*, 22–24.

Obukhov, A. M. (1941b), Spectral energy distribution in a turbulent flow, *Izv. Akad. Nauk SSSR*, *5*, 453–466.

Okuno, A., and A. Masuda (2003), Effect of horizontal divergence on the geostrophic turbulence on a beta-plane: Suppression of the rhines effect, *Physics of Fluids*, *15*(1), 56–65, doi:http://dx.doi.org/10.1063/1.1524188.

Onsager, L. (1945), The distribution of energy in turbulence, *Phys. Rev.*, *68*(11-1), 286.

Penny, A. B., A. P. Showman, and D. S. Choi (2010), Suppression of the Rhines effect and the location of vortices on Saturn, *Journal of Geophysical Research-Planets*, *115*, doi:10.1029/2009JE003384.

Reznik, G. M. (2010), Dynamics of localized vortices on the beta plane, *Izvestiya Atmospheric and Oceanic Physics*, *46*(6), 784–797, doi:10.1134/S0001433810060095.

Rhines, P. B. (1975), Waves and turbulence on a beta-plane, *Journal of Fluid Mechanics*, *69*(June 10), 417–443, doi:10.1017/S0022112075001504.

Scott, R. K., and D. G. Dritschel (2013), Halting scale and energy equilibration in two-dimensional quasigeostrophic turbulence, *Journal of Fluid Mechanics*, *721*, doi:10.1017/jfm.2013.120.

Scott, R. K., and L. M. Polvani (2007), Forced-dissipative shallow-water turbulence on the sphere and the atmospheric circulation of the giant planets, *Journal of The Atmospheric Sciences*, *64*, doi:10.1175/JAS4003.1.

Sheng, J., and Y. Hayashi (1990a), Estimation of atmospheric energetics in the frequency domain during the FGGE year, *J Atmos Sci*, *47*(10), 1255–1268, doi:10.1175/1520-0469(1990)047⟨1255:EOAEIT⟩2.0.CO;2.

Sheng, J., and Y. Hayashi (1990b), Observed and simulated energy cycles in the frequency domain, *J Atmos Sci*, *47*(10), 1243–1254, doi:10.1175/1520-0469(1990)047⟨1243:OASECI⟩2.0.CO;2.

Smith, K. S. (2004), A local model for planetary atmospheres forced by small-scale convection, *Journal of the Atmospheric Sciences*, *61*(12), 1420–1433, doi:10.1175/1520-0469(2004)061⟨1420:ALMFPA⟩2.0.CO;2.

Smith, K. S., G. Boccaletti, C. C. Henning, I. Marinov, C. Y. Tam, I. M. Held, and G. K. Vallis (2002), Turbulent diffusion in the geostrophic inverse cascade, *Journal of Fluid Mechanics*, *469*, 13–48, doi:10.1017/S0022112002001763.

Smith, S. G. L. (1997), The motion of a non-isolated vortex on the beta-plane, *Journal of Fluid Mechanics*, *346*, 149–179.

Srinivasan, K., and W. R. Young (2012), Zonostrophic instability, *Journal of the Atmospheric Sciences*, *69*(5), 1633–1656, doi:10.1175/JAS-D-11-0200.1.

Stammer, D. (1997), Global characteristics of ocean variability estimated from regional TOPEX/POSEIDON altimeter measurements, *J. Phys. Oceanogr.*, *27*, 1743–1769, doi:10.1175/1520-0485(1997)027⟨1743:GCOOVE⟩2.0.CO;2.

Stern, M. E. (1975), Minimal properties of planetary eddies, *Journal of Marine Research*, *33*(1), 1–13.

Suhas, D. L., and J. Sukhatme (2015), Low frequency modulation of jets in quasi-geostrophic turbulence, *Physics of Fluids*, *27*(1), doi:10.1063/1.4905710.

Sukoriansky, S., N. Dikovskaya, and B. Galperin (2007), On the arrest of inverse energy cascade and the rhines scale, *Journal of the Atmospheric Sciences*, *64*(9), 3312–3327, doi:10.1175/JAS4013.1.

Sukoriansky, S., N. Dikovskaya, and B. Galperin (2008), Nonlinear waves in zonostrophic turbulence, *Physical Review Letters*, *101*(17), doi: 10.1103/PhysRevLett.101.178501.

Tabeling, P. (2002), Two-dimensional turbulence: a physicist approach, *Phys. Rep.*, *362*(1), 1–62, doi:10.1016/S0370-1573(01)00064-3.

Taylor, G. I. (1938), The spectrum of turbulence, *Proceedings of the Royal Society of London. Series A - Mathematical and Physical Sciences*, *164*(919), 476–490, doi:10.1098/rspa.1938.0032.

Tennekes, H. (1975), Eulerian and lagrangian time microscales in isotropic turbulence, *J. Fluid Mech.*, *67*, 561–567, doi:10.1017/s0022112075000468.

Theiss, J. (2006), A generalized Rhines effect and storms on Jupiter, *Geophysical Research Letters*, *33*(8), doi:10.1029/2005GL025379.

Tran, C. V., and J. C. Bowman (2003), Energy budgets in Charney-Hasegawa-Mima and surface quasigeostrophic turbulence, *Physical Review E*, *68*(3, 2), doi: 10.1103/PhysRevE.68.036304.

Tran, C. V., and D. G. Dritschel (2006), Impeded inverse energy transfer in the Charney-Hasegawa-Mima model of quasi-geostrophic flows, *Journal of Fluid Mechanics*, *551*, 435–443, doi:10.1017/S0022112005008384.

Vallis, G. K. (2006), *Atmospheric and oceanic fluid dynamics*, 745 pp., Cambridge University Press, Cambridge, U.K., doi:10.2277/0521849691.

Vallis, G. K., and M. E. Maltrud (1993), Generation of mean flows and jets on a beta-plane and over topography, *J. Phys. Oceanogr.*, *23*(7), 1346–1362, doi: 10.1175/1520-0485(1993)023⟨1346:GOMFAJ⟩2.0.CO;2.

van Leeuwen, P. J. (2007), The propagation mechanism of a vortex on the beta plane, *J. Phys. Oceanogr.*, *37*(9), 2316–2330, doi:10.1175/JPO3107.1.

von der Heydt, A., S. Grossmann, and D. Lohse (2003), Response maxima in modulated turbulence, *Phys. Rev. E*, *67*(4), 046,308, doi:10.1103/physreve.67.046308.

Wortham, C. (2013), A multi-dimensional spectral description of ocean variability with applications, Ph.D. thesis, Massachusetts Institute of Technology.

Wortham, C., and C. Wunsch (2014), A multidimensional spectral description of ocean variability, *J. Phys. Oceanogr.*, *44*(3), 944–966, doi:10.1175/JPO-D-13-0113.1.

Wunsch, C. (2009), The oceanic variability spectrum and transport trends, *Atmosphere-Ocean*, *47*(4), 281–291, doi:10.3137/OC310.2009.

Wunsch, C. (2010), Toward a midlatitude ocean frequency-wavenumber spectral density and trend determination, *J. Phys. Oceanogr.*, *40*(10), 2264–2281, doi: 10.1175/2010JPO4376.1.

Wyngaard, J. C., and S. F. Clifford (1977), Taylors hypothesis and high-frequency turbulence spectra , *Journal of the Atmospheric Sciences* , *34*(6), 922–929, doi: 10.1175/1520-0469(1977)034⟨0922:THAHTS⟩2.0.CO;2.

Xiao, Z., M. Wan, S. Chen, and G. L. Eyink (2009), Physical mechanism of the inverse energy cascade of two-dimensional turbulence: a numerical investigation, *J. Fluid Mech.*, *619*, 1–44, doi:10.1017/s0022112008004266.

Zhang, Y., and Y. D. Afanasyev (2014), Beta-plane turbulence: Experiments with altimetry, *Physics of Fluids*, *26*(2), doi:10.1063/1.4864339.